A molecular dynamics study of water and aqueous solutions in confinements of differing surface roughness and hydroaffinity

Molekulardynamische Untersuchungen von Wasser und wässrigen Lösungen in Confinements unterschiedlicher Oberflächenrauigkeit und Hydroaffinität

Zur Erlangung des Grades eines Doktors der Naturwissenschaften (Dr. rer. nat.)
genehmigte Dissertation von Michael F. Harrach, M.Sc., geboren in Frankfurt am Main.
Tag der Einreichung: 01.07.2015, Tag der Prüfung: 20.07.2015
2015 — Darmstadt — D 17

1. Gutachten: Prof. Dr. Barbara Drossel
2. Gutachten: Prof. Dr. Michael Vogel

TECHNISCHE
UNIVERSITÄT
DARMSTADT

Fachbereich Physik
Institut für Festkörperphysik
AG Drossel

A molecular dynamics study of water and aqueous solutions in confinements of differing surface roughness and hydroaffinity
Molekulardynamische Untersuchungen von Wasser und wässrigen Lösungen in Confinements unterschiedlicher Oberflächenrauigkeit und Hydroaffinität

Genehmigte Dissertation von Michael F. Harrach, M.Sc., geboren in Frankfurt am Main.

1. Gutachten: Prof. Dr. Barbara Drossel
2. Gutachten: Prof. Dr. Michael Vogel

Tag der Einreichung: 01.07.2015
Tag der Prüfung: 20.07.2015

2015 — Darmstadt — D 17

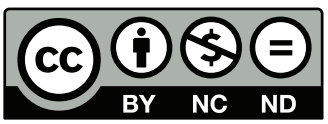

Erklärung zur Dissertation

Hiermit versichere ich, die vorliegende Dissertation ohne Hilfe Dritter nur mit den angegebenen Quellen und Hilfsmitteln angefertigt zu haben. Alle Stellen, die aus Quellen entnommen wurden, sind als solche kenntlich gemacht. Diese Arbeit hat in gleicher oder ähnlicher Form noch keiner Prüfungsbehörde vorgelegen.

Darmstadt, den 01.07.2015

(Michael F. Harrach)

”The best advice which comes from years of study of liquid mixtures is to use any model in so far as it helps, but not to believe that any moderately simple model corresponds very closely to any real mixture.”

(*George Scatchard*)

Abstract

Due to its abundance and its relevance for life, water is one of, if not the, most important liquid(s). It has various anomalies and an extremely rich phase diagram. Not only are water, and correspondingly aqueous solutions, everywhere, but often they are found in confined conditions. Examples range from the biological, e.g. the cells in our own bodies, to technical applications of microfluidics and, of course, geological concerns.

There are many areas concerning the behavior of water that are still not completely understood. In many such cases molecular dynamics simulations can play an important role, since they not only allow us to experience a resolution on the molecular scale, but also the possibility to actualize gedanken experiments which are not accessible to current experimental methods - or if accessible, at the very least, highly expensive. Of course, it is of utmost importance concerning the insights from such simulations to be aware of their limitations, and to keep the influence of the inevitable simplifications any molecular dynamics model will necessitate in mind. It is necessary to distinguish between effects from geometrical parameters, finite-size effects, the characteristics of different water models, and their interaction potentials.

The aim of this study is to investigate the behavior of pure water and aqueous solutions, namely isobutyric acid and water, in confinement, with special regard given to the roughness and structure of the confining interfaces. This is done by first considering hydrophobic and hydrophilic confining walls, with a planar geometry, and systematically varying wall roughness while keeping the same average potential, as well as observing the effects on different water models, namely TIP3P, TIP4P and TIP5P. We find that in the hydrophobic regime the smooth wall generally represents a usable abstraction of the atomically rough walls, while in the hydrophilic regime there are pronounced differences in structure and dynamics between all stages of wall roughness. For a small lattice constant, however, the smooth and the atomically rough wall still share a number of structural and dynamical similarities, although the degree of conformity depends on the water model. Out of the three water models, TIP5P water shows the largest degree of tetrahedral ordering and is often the one that is least perturbed by the presence of the wall.

Further, the behavior of SPC/E water in cylindrical confinement is investigated. In this case confinement refers to amorphous silica pores and amorphous ice pores as well as completely smooth pores, where the potential felt at a given distance from the pore wall is an averaged atomic potential. As compared to rough walls, smooth walls induce stronger distortions of water structure for both silica and ice confinements. On the other hand, unlike the smooth pores, the rough pores strongly slow down water dynamics at the pore wall. The slowdown vanishes when reducing the atomic charges in the wall, i.e. when varying the hydroaffinity, while keeping the surface topology intact, indicating that this is not a geometric effect, but rather due to the fact that the wall atoms provide a static energy landscape along the surface, e.g. fixed anchor-points for hydrogen bonds, to which the water molecules need to adapt, blocking channels for structural rearrangement. In the smooth pores, water dynamics can be faster than in the bulk liquid, not only at the pore wall, but also in the pore center. Changes in the tetrahedral order rather than in the local density are identified as the main cause for this change of the dynamical behavior in the center of smooth pores.

Lastly, molecular dynamics simulations of an isobutyric acid (iBA) and TIP3P water mixture in a cylindrical silica nanopore are performed for a number of different weight percentages. The general behavior is only weakly dependent on the mixture ratio and contrary to expectations the iBA features prominently at the pore wall, despite the hydrophilic nature of the pore. Increasing temperature triggers

more thorough mixing of the components which, coupled with other results, suggests an energetic cause for the accretion of iBA at the pore boundary.

Zusammenfassung

Aufgrund seiner Häufigkeit und der ausgeprägten Relevanz in Hinsicht auf das Leben an sich, ist Wasser eines der, wenn nicht das, wichtigste(n) Fluid(e) überhaupt. Wasser weist zahlreiche Anomalien auf und besitzt ein reichhaltiges Phasenverhalten. Wasser, und entsprechend wässrige Lösungen, sind nicht nur überall zu finden, sie tauchen auch häufig unter eingeschränkten geometrischen Verhältnissen auf. Beispiele dafür reichen von der Biologie - man denke an die Zellen aus denen unsere Körper aufgebaut sind - über technische Applikationen von Mikrofluidität zu geologischen Gegebenheiten.

Es gibt zahlreiche Bereiche in Bezug auf das Verhalten von Wasser, für welche noch Erklärungsbedarf vorliegt. In vielen dieser Fälle können Molekulardynamiksimulationen hilfreich sein. Molekulardynamiksimulationen erlauben nicht nur eine Auflösung auf der molekularen Ebene, sondern auch die Möglichkeit Gedankenexperimente zu verwirklichen, welche experimentell aufgrund der technischen Gegebenheiten nicht umsetzbar sind - oder falls umsetzbar, zumindest sehr teuer wären. Natürlich ist es von äußerster Wichtigkeit in Bezug auf die Einsichten, welche durch Simulationen gewonnen werden, die Grenzen dieser Vorgehensweise und die Einflüsse der unvermeidlichen Vereinfachungen welche Atom- und Molekülmodelle mit sich bringen im Hinterkopf zu behalten. Man muss zwischen den Effekten unterscheiden, welche durch geometrische Parameter gegeben sind, welche sich durch finite-size Effekte ergeben oder welche von gegebenen Charakteristika der Modelle und ihrer Interaktionspotentiale abhängen.

Das Ziel dieser Studie liegt darin, das Verhalten von Wasser und wässrigen Lösungen, genauer gesagt Isobuttersäure und Wasser, unter geometrischer Einschränkung zu untersuchen, und dabei den Fokus auf den Einfluss der Rauigkeit und Struktur gegebener Grenzflächen zu legen. Dazu werden zunächst ebene hydrophobe und hydrophile Grenzflächen mit systematisch variierter Rauigkeit in Betracht gezogen, wobei das mittlere Wandpotential beibehalten wird. Der Einfluss dieser Grenzflächen auf verschiedene Wassermodelle (TIP3P, TIP4P und TIP5P) wird untersucht. Es stellt sich heraus, dass im hydrophoben Regime die glatten Wände eine annehmbare Abstraktion darstellen, während im hydrophilen Regime die strukturellen und dynamischen Unterschiede zwischen verschiedenen Rauigkeitsstufen wesentlich ausgeprägter ausfallen.
Für kleine Gitterkonstanten teilen die glatten und rauen Wände noch einige strukturelle und dynamische Eigenschaften, wobei der Übereinstimmungsgrad noch zusätzlich vom Wassermodell abhängt. Von den drei genannten Modellen weist TIP5P die größte tetrahedale Ordnung auf und wird generell am wenigsten durch die Präsenz einer Grenzfläche gestört.

Des Weiteren wird das Verhalten von SPC/E Wasser in zylindrischem Confinement, bestehend aus amorphen Silikaporen, amorphen Eisporen und vollständig glatten Poren, welche auf radialsymmetrische Potentialen beruhen, untersucht. Die ”glatten” Poren basieren auf dem mittleren Potential, welches von den Silika- und Eisporen ausgeht. Im Vergleich zu den atomar ”rauen” Poren induzieren die glatten Poren stärkere Störungen in Bezug auf die native Wasserstruktur. Im Gegensatz zu den glatten Poren wird bei den rauen Poren die Wasserdynamik nahe an der Porenwand stark verlangsamt. Diese Verlangsamung verschwindet, wenn innerhalb der rauen Pore die Ladungen einzelner Atome reduziert werden, also bei Variation der Hydroaffinität unter Beibehaltung der Porenstruktur. Dies impliziert, dass es sich dabei nicht um einen geometrischen Effekt handelt, sondern um eine Folge davon, dass die Wandatome eine statische Energielandschaft erzeugen, z.B. durch das Auftreten starrer Anknüpfungspunkte für die Bildung von Wasserstoffbrücken, an welche sich die Wassermoleküle anpassen müssen. Dies blockiert dann strukturelle Umgestaltungen. In den glatten Poren tritt eine beschleunigte Wasserdynamik nicht nur an den Porenwänden auf, sondern auch im Poreninneren. Änderungen

im tetraedischen Ordnungsparameter werden als Hauptinitiator für das Verhalten im Poreninneren identifiziert, während lokale Dichteschwankungen nur eine untergeordnete Rolle spielen.

Schließlich werden Molekulardynamiksimulationen von Isobuttersäure-Wasser Mischungen in einer zylindrischen Silika-Nanopore mit einer Reihe an unterschiedlichen Gewichtsverhältnissen durchgeführt. Das Verhalten der Mischung hängt nur schwach vom Gewichtsverhältnis ab und im Gegensatz zu ersten Erwartungen tritt, trotz des hydrophilen Charakters der Porenwand, vor allem Isobuttersäure an der Porenwand auf. Höhere Temperaturen führen zu einer vollständigeren Durchmischung und damit einer Reduktion der Menge an Isobuttersäure an der Porenwand. Dies deutet auf einen energetischen statt entropischen Grund für die Anlagerung hin.

Contents

Acronyms

3LW	denotes the three-layered waterlike atomistic walls from 5.1
C0	denotes the atomistic walls from 5.1 (middling roughness)
C1	denotes the atomistic walls from 5.1 (pronounced roughness)
CRR	cooperatively rearranging regions
HB	hydrogen bond
HS	hard sphere
iBA	isobutyric acid
ISF	intermediate scattering function
LJ	Lennard Jones
MD	Molecular dynamics
OAC	orientational autocorrelation function
OCP	one component plasma (a system of charged classical particles moving in a uniform charge neutralizing background)
RCF	residence correlation function
SS	soft spheres, here denoting a system of interaction points with a repulsive r^{-l} potential, $l \in \mathbb{N}$
SW	denotes the smooth walled potential constraints from 5.1
VFT	Vogel-Fulcher-Tammann

1 Introduction

This thesis is about the behavior of water and mixtures involving water in confinement. Water is one of the most important liquids there are, due to its abundance and its relevance for life. Water plays an important role in our everyday life as well as in various scientific fields. It also displays many unusual properties, which are often attributed to the presence of hydrogen bonds. Among these properties are various anomalies and an extremely rich phase diagram. In many biological, geological, or technological systems water is spatially confined on the nano-scale, with various types of geometries and surface interactions, which modify the structure and dynamics of water. In fact, it has been proposed that most of Earth's water is confined by minerals in the lower Earth mantle [1].

Examples and applications for systems with confined water range from environmental studies [2] over microfluidics [3] to lab-on-a-chip [4], biological investigations [5, 6], and efforts to verify the existence of a liquid-liquid critical point [7, 8, 9].

Understanding the structure and dynamics of water in confinement is therefore of great importance. There exist various theoretical approaches to model and simulate water at interfaces, ranging from quantum mechanical [10, 11, 12], over classical molecular dynamics simulations [13, 14, 15, 16, 17], to more abstract models [18, 19, 20, 21, 22, 23, 24, 25]. These studies use different water models and model the interface and its interaction with water in different ways. How these differences affect the structure and dynamics of water is not yet fully understood. In particular, the basic structure of water on hydrophilic surfaces remains a major open issue [26], as does the influence of the amount of adsorbed water on a given surface [27, 28, 29], i.e. the influence of pressure.

Molecular dynamics (MD) simulations are often an insightfull tool when studying such phenomena, since they allow the user to observe the system and evaluate interactions on a molecular scale, as well as correlate different observables which the experimentalist has no direct access to. More on MD simulations can be found in section 2.

The choice of the water model already has an effect on the observed properties, even when only bulk behavior is investigated, without the presence of interfaces. There exist a large number of water models [30], and new models are still being invented with the aim to better reproduce the experimental properties of water. However, until today no water model is able to simultaneously reproduce the melting temperature and the temperature of maximum density.

In this study TIP3P [31], TIP4P [32], TIP5P [33] and SPC/E [34] water are used. A comparison of the three models TIP3P, TIP4P and TIP5P, was done by Vega et al. [35], where TIP5P and TIP4P water were judged to be of similar quality. TIP3P water performs poorer, but it has the advantage of simplicity and thus allows for larger simulations. Additionally, the TIP3P model is part of the CHARMM package and often used in simulations of biological systems. Another comparison of SPC, SPC/E, TIP4P and TIP5P water has led to the conclusion that TIP4P water and SPC water are best for reproducing experimental values [36]. Thus there is no agreement as to which water model is the best one.

The modeling of water-wall interactions is done in many different ways, attempting to correctly capture the different experimental situations with hydrophobic, hydrophilic, or functionalized walls, or with different types of confinement such as in naturally abundant nanoporous systems like zeolithes or in arrays of designed pores [37].
Modeling ranges from ab-initio models for atomic level interactions [10, 11, 12], to molecular interactions with e.g. crystalline hydrophobic and hydrophilic alkans or alcohols [38], carbon alkyl chains bound to a substrate, where the hydroaffinity is tuned by using different functional head groups [39, 40] and smooth walls given by an exterior potential [13], which can also include orientating contributions [41].

One great advantage of theoretical investigations of confined water is that the effects of the general geometry, the wall structure, and the interaction potentials can be studied separately. The mere confinement effect can be investigated by pinning part of the water molecules, thus ensuring that no foreign local structure is forced upon the free part of the liquid [15, 16, 14]. Klameth and Vogel [14] showed that while the structure of the confined water is not modified, the dynamics is spatially inhomogeneous and slow down when approaching the boundary of pinned water. Watanabe et al. [15] investigated geometrical confinement effects near the glass transition point and found that these lead to slower dynamics coming from a wall-induced enhancement of glassy structure. Kumar et al. [42] studied systems with purely repulsive potentials, resulting in qualitatively similar behavior to Lennard Jones systems, indicating that the effects of the confinement might be only weakly dependent on the exact form of the confining potential.

Besides pure confined water this study also contains a section on the confined water and isobutyric acid mixture. Isobutyric acid (iBA), or 2-methylpropanoic acid, has both hydrophilic and hydrophobic functional groups, leading to phase separation when mixed with water. It belongs to the group of carboxylic acids, which play an important role in a number of industrial relevant separation processes [43]. Furthermore they are used as basic building blocks of soaps and detergents [44, 45], used as raw materials for the production of nylon, biodegradable plastics, and certain pharmaceuticals, used as buffers and acidulants (food preservatives), flavoring agents, fungicides, and insecticides, biomass products, and catalysts [44, 46, 47]. Carboxylic acid derivatives find widespread application in various commercial sectors as well [45, 48], and are often present in aqueous waste streams and as byproducts of industrial operations [49].

In general the behavior of liquid-liquid mixtures and liquid-liquid transitions are very important as well, with a large impact on relevant topics such as oil recovery, lubrication, coating technology and pollution [50, 51, 52].

Confinement can severely change the phase diagram of mixtures, especially for very small pores [53] with a large amount of surface area. Therefore, understanding these effects is vital to developing new separation technologies and optimizing currently used techniques. A short introduction to the main theoretical approaches used for binary mixtures in confinement is given in section 4, subsection 4.3.

In a one dimensional system we cannot see a true phase transition between a one- and two-phase state [54], of course, but rather microphase separation with alternating domains of both phases [53]. While not strictly one dimensional systems, nanopores are small enough to be effected by this. When increasing the temperature the system does not pass a true critical point, but still shows phenomena reminiscent of a critical point, like e.g. a peak in the heat capacity [55, 56].

The phase behavior of simple fluids, mixtures and liquid crystals is dramatically altered when these fluids are contained in porous media having a pore size ranging from ten to a thousand ångströms [57]. In general the effects of confinement consist of a lowered critical temperature (in case of an upper critical solution temperature, in case of a lower critical solution temperature it is generally elevated), a shift in the phase envelope towards the preferentially adsorbed phase, if existent, and a slight reduction in the area of immiscibility as evidenced by both experimental [58, 55, 59, 60, 50, 51] and theoretical [53, 52, 61, 62, 50, 51] studies. Generally the effects are stronger for smaller pore widths, although this is not always the case [63].

The investigative part of this study, section 5, is divided into three main parts. All feature a comparison of the effects of rough and smooth confining walls of comparable average potential, although pertaining to different geometries and/or contents.

In the first part, 5.1, the results of a comprehensive study of the combined influence of water model, wall modeling, and hydroaffinity on the structure and dynamics of confined water are presented. Smooth

and atomistic flat walls are used. The smooth walls interact with the water via potentials that have either a hydrophobic or a hydrophilic effect. The atomistic walls have a hexagonal graphene-like lattice structure. Two different lattice constants, i.e., different wall "roughness", are used and the strength of the hydrophobic and hydrophilic interactions are chosen in such a way that the average potential at a given distance from the wall is identical to that of the smooth walls. This allows to distinguish the effect of interaction strength from the effect of wall roughness. Additionally, another type of hydrophilic wall is implemented, which consists of three atomic layers, mimicking hydrogen and oxygen atoms respectively. This water-like wall thus attracts the oxygen atoms of water as well as the hydrogen atoms. In this part the TIP3P [31], TIP4P [32] and TIP5P [33] water models at ambient temperature and pressure are used.

In the second part, 5.2, the structure and dynamics of SPC/E [34] water in cylindrical confinements are studied in a broad temperature range. The matrices consist of either amorphous silica or amorphous ice, specifically, a suitable set of pinned water molecules. All studied pores have radii between 11 Å and 15 Å, with some results pertaining to a 25 Å pore. To gain insights into the role of the topology of the wall, not only atomistic walls are considered, but also smooth walls corresponding to silica or ice environments. These are produced by potentials averaging the Lennard-Jones (LJ) interaction of the given pore with the water molecules. To determine the role of the hydroaffinity of the confinement, focus is put on the atomistic pores and the charges of the wall atoms are reduced, while leaving the wall topology unchanged. The relation between structure and dynamics is considered by correlating tetrahedral entropy [64] and correlation time for water in the various types of confinements. The atomistic simulations and evaluation of the resulting data was done by Felix Klameth.

In the third part, 5.3, a mixture of isobutyric acid (iBA) and TIP3P water is examined in a silica nanopore of roughly 4.2 nm diameter. The behavior of the mixture is contrasted with the behavior as shown when confined in a smooth pore based on the average potential of the silica nanopore. W.r.t. the rough pore, the model system results in wetting of the iBA, with a small amount of water at the pore wall, and a broad distribution of dynamic relaxation times. Interestingly the distribution of relaxation times of the iBA is not completely monotonic w.r.t. translational motion, but rather shows a slight speed up of dynamics directly at the pore boundary, a facet of behavior not seen for pure confined iBA. When observing the susceptibility w.r.t. translational and orientational movement different dynamic regimes are apparent for both dynamics. Comparison to the smooth pore makes it possible to gauge the influence of pore roughness and the availability of hydrogen bonding sites.

The make-up of these sections is always the same. In the beginning the simulation methods are presented. This is followed by the presentation of results and a discussion, after which the most important aspects of our findings are reiterated and put into context concerning their meaning for the scientific community.

The rest of this study is organized as follows. Section 2 gives an overview of how molecular dynamics simulations work, with a short listing of the advantages and disadvantages in 2.2. Section 3 introduces the main observables which are evaluated in the simulation. Section 4 touches on some of the theory and state of research relevant to this thesis. A more detailed listing is given at the beginning of the section. Details concerning simulation methods and results of this thesis are given in section 5. As described above it is split into three major subsections. Afterwards the most relevant parts are reiterated in the conclusion 6. In addition there follows a listing of all figures, tables and references, publications by the author, as well as a short curriculum vita and acknowledgment.

2 Molecular dynamics simulations

Classic molecular dynamics simulations, in the following referred to as MD simulations, allow us to observe position, orientation, and velocity of single atoms, or rather position and velocity of given interaction points, representing part of a molecule. As such, any observable rooted in these parameters can be calculated. This makes such simulations a valuable tool, enabling us to investigate on a molecular level.

However, MD simulations have their drawbacks as well. In the following a short overview will be given on how MD simulation work, followed by a list of advantages and drawbacks of this method. Mainly I will refer to the NAMD program [65]. While other molecular dynamics programs use the same basic functions and procedures, there are slight differences with respect to availability of certain algorithms, naming conventions and similar. In this work all MD simulations were done either using the NAMD or GROMACS [66] simulation package.

2.1 Molecular dynamics simulations - how do they work?

In molecular dynamics simulations atoms, or even parts of molecules, are represented by a given set of interaction points, each outfitted with parameters describing the potential it carries. For convenience we will generally refer to these interaction points as "atoms" in this section. Such a many-body problem cannot be solved analytically, but has to be calculated numerically. The dynamics of the atoms is assumed to be governed by the Newtonian equations of motion,

$$m_i \ddot{\vec{r}}_i = -\frac{\partial}{\partial \vec{r}_i} U_{\text{total}} \left(\vec{r}_1, \vec{r}_2, \ldots, \vec{r}_N\right), \tag{1}$$

where m_i is the mass of the i'th atom, $\vec{r}_i$ its position, and U_{total} the total potential energy, depending on all atomic positions. U_{total} consists of bonded and non-bonded interaction,

$$U_{\text{total}} = U_{\text{bond}} + U_{\text{angle}} + U_{\text{dihedral}} + U_{\text{vdw}} + U_{\text{Coulomb}} + U_{\text{ext}}, \tag{2}$$

where the bonded interactions U_{bond}, U_{angle} and U_{dihedral} govern things like bond-length and angles between atoms or groups of atoms, while U_{vdw} and U_{Coulomb} denote the van der Waals and Coulomb interaction respectively. Additionally, NAMD supplies the user with the ability to impose external potentials, U_{ext}, on the system.
Typically periodic boundary conditions are used in these kinds of simulations, thus eliminating surface effects at the system boundary. This also means that it is unfeasible to calculate the exact force owing to non-bonded interactions, since every atom interacts with every other non-bonded atom - and their counterparts in neighboring cells. Therefore the van der Waals interaction is cut off at a specified distance. Electrostatic interaction can either be handled the same way, or the periodicity can be exploited, computing the full electrostatic interaction with minimal additional cost, using the particle-mesh Ewald (PME) method, where the electrostatic interaction is divided into short-range and long-range parts. The short-range part is calculated directly, while for the long range part the charges are distributed on a grid based on the unit cell, allowing the interaction to be calculated via fast Fourier transform in reciprocal space.

NAMD uses the Verlet method [67] for NVE simulations, where velocities are evaluated in half-integer timesteps, with the values used to determine position in the full next timestep:

$$v_{n+\frac{1}{2}} = v_n + \frac{1}{m} F_n \frac{\Delta t}{2} \quad \text{("half-kick")} \tag{3}$$

$$r_{n+1} = r_n + v_{n+\frac{1}{2}} \Delta t \quad \text{("drift")} \tag{4}$$

$$F_{n+1} = F(r_{n+1}) \quad \text{("compute force")} \tag{5}$$

$$v_{n+1} = v_{n+\frac{1}{2}} + \frac{1}{m} F_{n+1} \frac{\Delta t}{2} \quad \text{("half-kick"),} \tag{6}$$

where v stands for velocity, r for position, F for force, m for mass and Δt are the timesteps. For a fixed time period, the method exhibits a global error proportional to Δt^2. Usually however, simulations are done in the NVT or NPT ensemble. There are several algorithms for maintaining temperature and pressure. The ones most commonly used in this thesis are the Langevin thermostat [65] and the Langevin-Piston barostat [68], respectively. The generic Langevin equation is given by

$$m\dot{v} = F(r) - \gamma v + \sqrt{\frac{2\gamma k_B T}{m}} R(t), \tag{7}$$

where γ is the friction coefficient, k_B is the Boltzmann constant, T is the temperature, and $R(t)$ is a univariate Gaussian random process. Coupling to the reservoir is modeled by adding the fluctuating and dissipative forces to the Newtonian equations of motion. The Langevin-Piston barostat is based on the extended system method by Anderson [69], where an additional degree of freedom is introduced to the system, corresponding to the volume of the simulation cell, which adjusts itself to equalize the internal and applied pressures. One can think of this additional degree of freedom as a "piston", hence the naming convention. This piston carries a "mass", with units of $\left(\text{mass} \cdot \text{length}^{-4}\right)$, which determines the decay time of the volume fluctuations. In the Langevin-Piston barostat the coupling of the piston degree of freedom to a heat bath is done by means of a Langevin equation.

Parameters for simulations can be established in a number of ways. Some, e.g. bond lengths and equilibrium angles, can be taken directly from experiment [70]. Others are parametrized via comparison to experimental findings like the temperature of maximum density [71]. And of course quantum chemical computations are used as well [70].

As such a MD simulation consists of the following steps:

1. set up the system parameters (potential interaction, volume/pressure, temperature, time step...)
2. set up initial atomic positions and velocities (e.g. taken from a Maxwell-Boltzmann distribution w.r.t. the correct temperature)
3. calculate the force on the atoms
4. determine velocity and position
5. repeat steps 3.) and 4.) while saving atomic positions and velocities with appropriate frequency

2.2 Advantages and disadvantages of molecular dynamics simulations

The advantages of MD simulations are rather clear. Positioning and dynamics of the molecules involved are completely open to the observer. System responses to arbitrary initial set-ups can be explored, including molecular configurations that are experimentally hard to reach or simply not achievable. This allows

the realization of gedanken experiments not accessible to current experimental methods and therefore the ability to distinguish between different influences, e.g purely geometric aspects of confinement as opposed to surface effects.

On the other hand the simulation can only be as good as the underlying potential. Different molecular models and interaction potentials might show different effects, neither of which necessarily have to conform to physical reality. Computational costs necessitate small system unit cells, with dimensions of a few nanometers and short time scales, usually in the nanosecond range. The use of periodic boundary conditions does not eliminate finite size effects and enforces long reaching unphysical correlations in bulk simulations, even in systems with only one component. The idea of periodic images is nonsensical as soon as critical length scales reach the size of the unit cell. This is especially important to keep in mind when investigating systems close to phase transitions, where correlation lengths can become infinite. And of course macroscopic phase separation or similar effects cannot be simulated in an infinite system built up from mirror images of a single small unit cell.

Since the interactions are built up using Newtonian equations of motions quantum mechanical effects are not taken into account and neither chemical reactions nor other processes based on electronic configurations are reproduced. While simulations on the level of electronic structure, so called ab-initio computations, can be done they are even further limited with regard to time scale and system size. Partially these problems can be mitigated, both on the level of MD simulations, by refinement of the molecular models, e.g. polarizable water models like the SWM4-NDP [72], and by hybridization of the simulation process. There exist both combinations of classical MD simulations and ab-initio computations [73], as well as combinations of classical MD and continuum mechanical simulations [74, 75].

Furthermore, MD simulations have come a long way since their beginning, an achievement which is strongly correlated with the advances in computing power. Since we can expect further progress on that front we can also expect the system size and time scale of MD simulations to grow accordingly.

3 Observables

3.1 Hydrogen bonds

Hydrogen bonding can be investigated experimentally with a number of different techniques. X-ray diffraction responds to the electron density, which for water is most pronounced around oxygen atoms [76, 77]. Neutron diffraction is sensitive to the positions of the nuclei. Studies with H_2O, D_2O, and mixtures of the two lead to $H-H$ and $H-O$ as well as $O-O$ radial distribution functions [78, 79]. Vibrational spectroscopy, both infrared and Raman, grants information about hydrogen bonding as well, since a local mode's vibrational frequency is highly sensitive to its hydrogen bonding environment [80, 81, 82, 83, 84]. X-ray absorption spectroscopy and x-ray emission spectroscopy have been shown to provide information about local structure in liquid water as well [85].

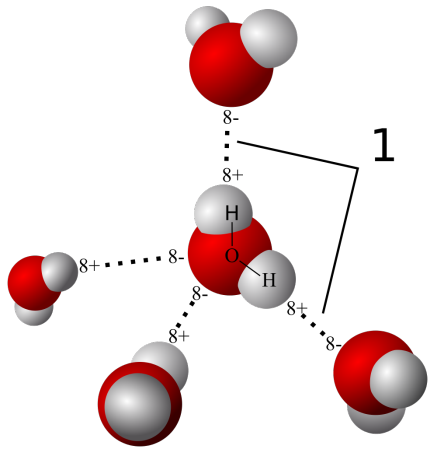

Figure 1: A water molecule with four hydrogen bonded neighbors. The tetrahedral structure is clearly recognizable. Graphic taken from [86], where it is displayed under under a Creative Commons license. First established by User Qwerter at Czech wikipedia, who is not affiliated with this work.

One controversy about hydrogen bonding is in how far it makes sense to assign the label of "hydrogen bond" to a given configuration, given that water consists of a three-dimensional network of hydrogen bonds with a broad distribution of O-H...O angles and distances, rendering the existence of a cut-off w.r.t. hydrogen bond definitions somewhat arbitrary. Some experimental data seems to indicate the existence of spectrally distinguishable hydrogen bond configurations. Such results have typically been interpreted as indicating that liquid water comprises two classes of HB domains: intact and broken [87]. Using temperature-dependent spontaneous Raman spectroscopy in conjunction with Monte Carlo simulations Smith et al. [87] were able to show that some of the supposed evidence for a multi-state system can originate from continuous distributions. As such one should keep in mind that the definitions for hydrogen bonds as used in molecular dynamics simulations are to a certain degree arbitrary.

A number of different hydrogen bonding definitions are used in molecular dynamics simulations, both energetic [88, 89, 90, 91] and geometrical, utilizing a number of different distances and angles [85].

In this study we use the same definition as Hartnig et al. [92], and consider two water molecules to be bonded when the angle between the intramolecular O-H vector and the intermolecular O...O vector is less than 30°, provided that the O...O separation is less than 3.35 Å. The same criteria is applied when assigning hydrogen bonds to other molecules, e.g. between isobutyric acid and silanol groups. In the latter case simple distance and energetic criteria were applied as well, however, the qualitative behavior did not change.

3.2 Tetrahedral order, tetrahedral order parameter, and tetrahedral entropy

Due to hydrogen bonding water has a tendency to settle in a tetrahedral structure, as fig. 1 illustrates. In reality of course, the structure is not quite as regular and a tetrahedral order parameter is one way to determine the quality of the tetrahedral distribution. We use the tetrahedral order parameter Q as

suggested by Errington and Debenedetti [93], which consists of a slightly rescaled version of the one originally developed by Chau and Hardwick [94], and is given by

$$Q = \langle q_i \rangle \equiv \left\langle 1 - \frac{3}{8} \sum_{j=1}^{3} \sum_{k=j+1}^{4} \left(\cos\left(\psi_{jk}\right) + \frac{1}{3} \right)^2 \right\rangle, \tag{8}$$

where the angular brackets denote the averages over all oxygen atoms and different points in time, and ψ_{jk} is the angle formed by the lines joining the oxygen atoms of two neighboring molecules $j, k \leq 4$ to the considered oxygen atom i. q_i varies between -3 and 1, with $Q = 0$ for an ideal gas and $Q = 1$ for a perfectly tetrahedral network.

Based on the distribution of tetrahedral order a tetrahedral entropy [64] can be defined by

$$S_Q(T) = S_0 + \frac{3}{2} k_B \int_{q_{\min}}^{q_{\max}} \ln(1 - q_i) P(q_i, T) \, \mathrm{d}q_i, \tag{9}$$

with $q_{\min} = -3$ and $q_{\max} = 1$. In this work the term "tetrahedral entropy" will generally be used for the difference $(S_Q(T) - S_0)/k_B$, where S_0 is a constant, the exact value of which depends on the discretization of possible states for q_i.

In contrast to other types of entropy, such as the excess entropy S^{ex} or the contribution of the two-point translational correlations to entropy S^2, the tetrahedral entropy can be easily evaluated in MD simulations, both for the bulk and for confined water.

3.3 Deviation from the uniform angular distribution

Let β denote the H–O–H angle of a given water molecule, e.g. 109.47° for SPC/E water. The uniform distribution $f_u(\cos(\psi_1), \cos(\psi_2))$ of $\cos(\psi_i)$, where ψ_i denotes the angle of the i'th O–H arm ($i \leq 2$) of a given molecule to an arbitrary vector $\vec{n}$, is given by

$$f_u(\cos(\psi_1), \cos(\psi_2)) = \frac{1}{2\pi} \frac{1}{\sqrt{2\cos(\psi_1)\cos(\psi_2)\cos(\beta) + \sin^2(\beta) - (\cos^2(\psi_1) + \cos^2(\psi_2))}} \tag{10}$$

We evaluate the deviation of the distribution of angles $g(\cos(\psi_1), \cos(\psi_2))$ from the uniform angular distribution as

$$\iint \left(\frac{f_u - g}{f_u} \right)^2 d\cos(\psi_1) \, d\cos(\psi_2). \tag{11}$$

This observable is a clear indicator of the existence of some kind of preferred orientational arrangement and also works well for one dimensional distributions, where the uniform distribution is given by

$$f_u(\cos(\psi_1)) = \frac{1}{2}. \tag{12}$$

3.4 Intermediate scattering function

The coherent $F_{s,q}$ and incoherent $F_{d,q}$ intermediate scattering function are defined as

$$F_{s,\vec{q}}(t) = \left\langle e^{-i\vec{q}\cdot\left(\vec{r}_i(t) - \vec{r}_i(0)\right)} \right\rangle \tag{13}$$

$$F_{d,\vec{q}}(t) = \left\langle e^{-i\vec{q}\cdot\left(\vec{r}_i(t) - \vec{r}_j(0)\right)} \right\rangle, \tag{14}$$

where $\vec{r}_i(t)$ gives the position of the atom or molecule under investigation at time t and $\vec{q}$ denotes the scattering vector. They are related to the van Hove correlation functions,

$$G_s(r,t) = \frac{1}{N}\left\langle \sum_{i=1}^{N} \delta\left(\vec{r} + \vec{r}_i(0) - \vec{r}_i(t)\right)\right\rangle \tag{15}$$

$$G_d(r,t) = \frac{1}{N}\left\langle \sum_{i\neq j}^{N} \delta\left(\vec{r} + \vec{r}_j(0) - \vec{r}_i(t)\right)\right\rangle, \tag{16}$$

via spatial Fouriertransform [95],

$$F_s(\vec{q},t) = \int d\vec{r} G_s(\vec{r},t)\, e^{-i\vec{q}\cdot\vec{r}} \tag{17}$$

$$F_d(\vec{q},t) = \int d\vec{r} G_d(\vec{r},t)\, e^{-i\vec{q}\cdot\vec{r}}. \tag{18}$$

Thus the coherent intermediate scattering function $F_{s,\vec{q}}$ characterizes how a density fluctuation of a tagged particle relaxes. Similarly one can study the relaxation of a density fluctuation relative to a given particle, i.e. a collective quantity via $F_{d,\vec{q}}$.
For the actual evaluation however, we mostly use a form of the intermediate scattering function, where we assume an isotropic system [96, 97] and can therefore ignore the vectorial nature of $\vec{q}$, retaining only the magnitude $q := \left|\vec{q}\right|$, with

$$F_{s,q}(t) = \left\langle \frac{1}{N}\sum_{i=1}^{N} \frac{\sin\left(q\left|\vec{r}_i(t) - \vec{r}_i(0)\right|\right)}{q\left|\vec{r}_i(t) - \vec{r}_i(0)\right|}\right\rangle \tag{19}$$

$$F_{d,q}(t) = \left\langle \frac{1}{N^2}\sum_{i=1}^{N}\sum_{j=1}^{N} \frac{\sin\left(q\left|\vec{r}_i(t) - \vec{r}_j(0)\right|\right)}{q\left|\vec{r}_i(t) - \vec{r}_j(0)\right|}\right\rangle. \tag{20}$$

The intermediate scattering function can be directly compared to experiments from inelastic neutron or X-ray scattering experiments. The magnitude of the scattering vector determines the length scale on which the dynamics of the system are probed. Therefore we generally chose a scattering vector of approximately $2\pi/\Delta_{nn}$, with Δ_{nn} giving the distance between nearest neighbors. In the case of water the intermediate scattering function was generally evaluated with respect to oxygen atom positions, with either $q = 2.27\ \text{Å}^{-1}$ (5.2, 5.3) or $q = 2.3\ \text{Å}^{-1}$ (5.1), while for isobutyric acid (5.3) we chose the center of mass of a given molecule, resulting in $q = 1.05\ \text{Å}^{-1}$. Slight deviations from the targeted magnitude of the scattering vector, imposed by the finite system size, arose when evaluating directionally (and therefore not using the simplified form of eq. (19)). These are recorded at the beginning of the corresponding sections. The correlation time τ_{isf} is defined as the time at which the function has decayed to a value of e^{-1}.

3.5 Residence correlation function

The residence correlation function $R(r,t)$ is given by [98]

$$R(r,t) = \frac{1}{N_r} \sum_{i=1}^{N} \theta_i(r,0)\,\theta_i(r,t) \tag{21}$$

$$\theta_i(r,t) = \begin{cases} 1 & \text{if molecule } i \text{ is in region } r \\ & \text{at time } t \\ 0 & \text{otherwise,} \end{cases} \tag{22}$$

where N_r is the average number of molecules in the region r, and gives the fraction of molecules that stay within the region r during a time t. We define the correlation time τ_{rcf} of the residence correlation function as the time at which the function has decayed to a value of e^{-1}.

3.6 Orientational autocorrelation function

The intermediate scattering function and residence correlation function both yield information about translational dynamics. While these are often coupled to rotational dynamics, decoupling, e.g. w.r.t. the melting temperature [99, 100] has been observed in experimental data as well. We calculate the orientational autocorrelation function $F_{rot}(t)$ as

$$F_{rot}(t) = \frac{1}{2}\left\langle 3\left(\vec{e}_i(0)\cdot\vec{e}_i(t)\right)^2 - 1\right\rangle, \tag{23}$$

where $\vec{e}_i(t)$ denotes the normalized unit vector describing the orientation of a predefined part of the i'th molecule at time t. As such the orientational autocorrelation function is given by the ensemble average of the second Legendre polynomial of $\vec{e}_i(0)\cdot\vec{e}_i(t)$. We define the correlation time τ_{rot} as the time at which the function reaches a value of e^{-1}.

3.7 Susceptibilities

From linear response theory it is known [95] that given a time correlation function $C_{AA}(t)$, w.r.t. the dynamical variable A the imaginary, or dissipative, part of the dynamic susceptibility χ, denoted as χ'' is proportional to the Fourier transform of $C_{AA}(t)$,

$$\chi'' \sim \omega \frac{1}{2\pi} \int_{-\infty}^{\infty} \mathrm{d}t\, C_{AA}(t)\, e^{-i\omega t}, \tag{24}$$

given that A is conjugate to the field causing the disturbance.

In this thesis calculation of the susceptibility is done in the real domain, evaluating only the cosine transformation via Filon's algorithm [101], as described in the dissertation by Thomas Blochowicz [102]. This is sufficient when the correlation function $C(t)$ is not only defined for positive times t, and therefore can be regarded as even, but also strictly real, since then the Fourier transform of $C(t)$ yields a real and even function as well [103].

4 Theoretical background

In this section of the thesis concepts and theoretical background which are relevant for the understanding and discussion of the results as given in section 5 will be introduced. A general understanding of the concept of molecular dynamics simulations has already been given in section 2, while the observables which are investigated are presented in section 3. A basic familiarity with both sections is therefore presumed.

4.1 Supercooled liquids, fragile and strong glass formers

In this section the concept of a glass will be discussed, along with an explanation as to the difference between fragile and strong glass formers. Afterwards the main ideas of the potential energy landscape description, which supports the slowdown of dynamics at rough, attractive interfaces, will be given, followed by a closer look at the Adam-Gibbs theory, a popular theory to explain the behavior of fragile glass formers.

The relevance of this topic becomes clear in 5.2, where we observe SPC/E water at temperatures below its melting point [104] and observe how the translational correlation time changes with temperature. The data is fitted to both the Arrhenius and the VFT (Vogel-Fulcher-Tammann) law [105, 106, 107], which will be further explained below.

So, what is a glass? A glass is in a non-equilibrium state of matter, with a liquid-like lack of long range order combined with solid-like elastic properties. Glasses are created when a fluid is cooled below the temperature of crystallization, but the actual process of crystallization is kinetically hemmed in and the fluid crosses over into the supercooled region. In this region the viscosity of the fluid can grow dramatically, by up to and over twelve orders of magnitude [108, 109].

With these high relaxation times the fluid can be kinetically unable to reach the state of thermal equilibrium, therefore becoming trapped in the glassy state. Experimentally this can be seen by a kink in the entropy or volume of the system. Since the glassy state is not a state of thermal equilibrium, but rather represents a kinetic transition, the glass transition temperature usually depends on external factors, like e.g. the cooling rate. Typically used definitions of the glass transition temperature T_g are accomplished by monitoring viscosity η or the structural relaxation time τ_α, with T_g being defined as the temperature where [110]

$$\eta\left(T_g\right) = 10^{12}\,\mathrm{Pa}\cdot\mathrm{s} \tag{25}$$

or [111]

$$\tau_\alpha\left(T_g\right) = 100\,\mathrm{s}. \tag{26}$$

This is where the Arrhenius,

$$\tau\left(T\right) = \tau_0\, e^{\frac{E_A}{k_\mathrm{B}T}}, \tag{27}$$

and VFT law,

$$\tau\left(T\right) = \tau_0\, e^{\frac{BT_0}{T-T_0}}, \tag{28}$$

come in. Both are equations which are often used to describe the viscosity or configurational relaxation time. Glass formers which follow the Arrhenius equation are known as strong glass formers, while fragile glass formers are often well described using the VFT equation. Both types are showcased in fig. 2. For experimental data on fragile and strong glass formers see e.g. [112].

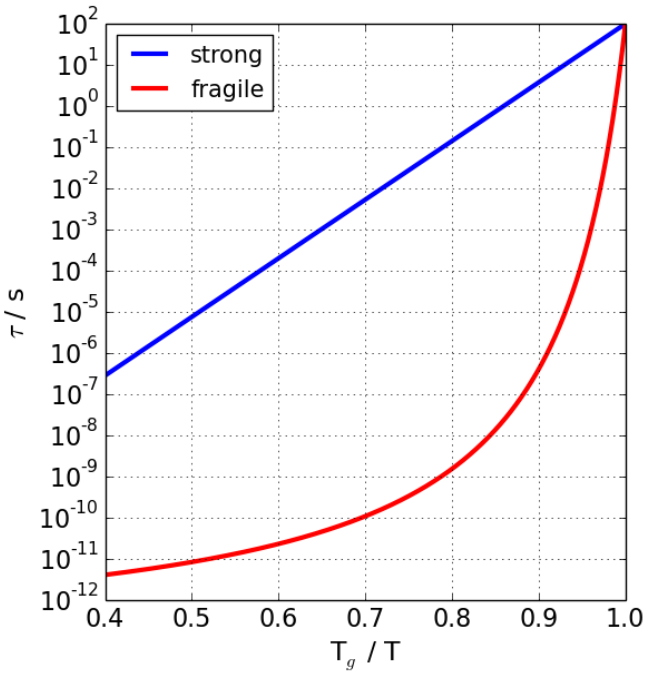

Figure 2: Depiction of fragile and strong glass formers with relaxation time τ as function of reduced temperature. Typical examples would be SiO_2 (fragile) and O-Terphenyl (strong). See e.g. fig. 3 from [112] for experimental data.

The Arrhenius law seems very intuitive. Structural relaxation can be seen as rearrangement of molecular order, transitioning between two local minima of the potential energy (this thought will be further expounded in the next part, where the main idea of the potential energy landscape description is given). To accomplish this transition an energy or free energy barrier ϵ has to be overcome, resulting in a relaxation time τ of

$$\tau = \tau_0 \, e^{\frac{\epsilon}{k_B T}} . \tag{29}$$

Therefore, relaxation times following the Arrhenius law, and consequently strong glass formers, are associated with constant energy barriers, whereas for fragile glass formers the energy barriers change with temperature. One explanation for such a change, which results in the originally phenomenological VFT equation, is given by the Adam-Gibbs theory [113], which is briefly explained further below.

4.1.1 Potential energy landscape description

The potential energy landscape description for glasses was originally conceived by Goldstein [114]. In this context the potential energy landscape is understood as the potential energy U plotted as a function of $3N$ atomic coordinates in a $3N+1$ dimensional space. In such a representation the state of a system is represented by a point moving on a surface with a $3N$ dimensional velocity, the average value of which is temperature dependent. Goldstein states a few main points in the justification of his description [114] for liquids in the glassy state and "not too far" from their glass transition, which can be summarized as follows.

- A glass at low temperatures, like a crystal, is at or near a potential energy minimum.
- The portion of the potential energy surface that represents the liquid or glassy region has a large number of minima of varying depths.
- At absolute zero, the state point of a glass will be trapped (ignoring quantum mechanical uncertainty considerations) in a minimum. As temperature is raised, sufficient thermal energy will become available to allow transitions to take place over potential barriers, even though they are large compared to the thermal energy.
- A transition over a potential barrier in U-space can be perceived as local in the sense that during the rearrangement from one local minimum to another most atomic coordinates change very little and only those in a small region of the substance change by appreciable amounts.

- At higher temperatures molecular rearrangement will take place in more than one region at a time. However, the system will always be close to a potential minimum in the sense that sudden cooling will force it into a potential minimum in such a way that most of the molecular coordinates experience little change.

- The potential barrier description of flow will have a range of validity at low temperatures, but gradually wash out as temperature is raised and the liquid becomes very fluid.

As pointed out, while the potential energy landscape is defined by the global state of the system, transitions can be seen as taking place on a local scale. The potential energy barrier separating two minima in the phase space is proportional to the number of particles, z, participating in the transition, which again is small compared to the overall number of particles. The temperature dependence of z is a natural candidate to explain fragile behavior [110], as seen in the following section on Adam-Gibbs theory.

Fig. 3 shows a schematic diagram of the potential energy hypersurface in the multidimensional configuration space for a many-particle system. The minima correspond to mechanically stable arrangements of the collective molecular coordinates of the system. The lowest lying minima are those whose neighborhoods would be selected for occupation by the system if it were cooled to absolute zero slowly enough to maintain thermal equilibrium. Higher lying minima correspond to amorphous particle packings [115].

Goldstein [114] assumes Arrhenius like (cf. eq. (29)) relaxation times for energy barriers of specific transitions. Given the different nature of predominantly local energy barriers this leads to a heterogeneous scenario, as seen in both experiments and computer simulations [116, 117, 118, 119].

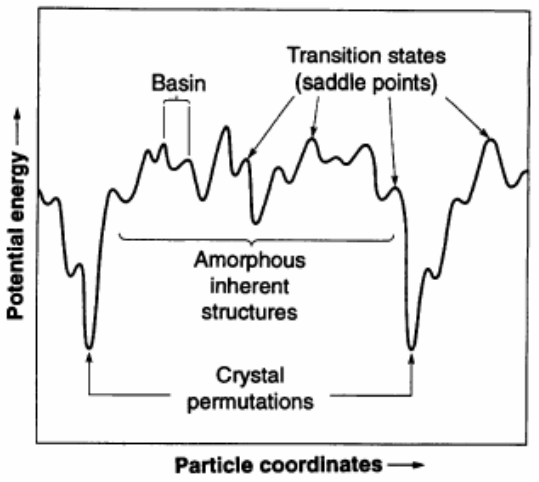

Figure 3: Schematic diagram of the potential energy hypersurface in the multidimensional configuration space for a many-particle system. The minima correspond to mechanically stable arrangements of the collective molecular coordinates of the system. From ref. [115], *A Topographic View of Supercooled Liquids and Glass Formation* by F. H. Stillinger (*Science* **267**, 1935 (1995)), reprinted with permission from AAAS.

4.1.2 Adam-Gibbs theory

Adam-Gibbs theory is based on the existence of so-called cooperatively rearranging regions (CRR). These CRRs are defined as subsystems of the sample which, upon a sufficient fluctuation of enthalpy, can, independently of its environment, rearrange into another configuration.

A graphical depiction of the notion of cooperativity is given in fig. 4. Let the number of molecules in such a CRR be denoted by z, with the system consisting of N CRRs, with n subsystems allowing cooperative rearrangement and $N - n$ subsystems in a state where a transition is not possible.
The cooperative transition probability $W(T)$ is then proportional to n/N, which is proportional to the ratio of the "partition function" Δ' when only summing up over energy and volume states allowing a

transition and the general partition function Δ, with the corresponding Gibbs energies of $G' = z\mu' = -k_B T \ln(\Delta')$ and $G = z\mu = -k_B T \ln(\Delta)$. This leads to a transition probability of

$$W(T) \sim \frac{\Delta'}{\Delta} = e^{\frac{-z\Delta\mu}{k_B T}}, \tag{30}$$

where $z\Delta\mu = z(\mu' - \mu)$ is the difference in the Gibbs free energy and therefore the free energy barrier which must be overcome. The dependence of the energy barrier per particle $\Delta\mu$ on temperature T and the number of constituents z of the CRR can be considered to be negligible. Compared to the exponential function the same is true for the proportionality factor, denoted by A. To obtain the average transition probability $\bar{W}(T)$ one has to sum over all possible transition probabilities $W(T)$, corresponding to all possible z. These are restricted by a minimal $z^\star$, the smallest number of constituents which allows a transition. As Adam and Gibbs [113] show, this number can be expressed by the Avogadro number N_A, the critical configurational entropy of the subsystem $s_c^\star$ and the molar configurational entropy of the macroscopic sample S_c via

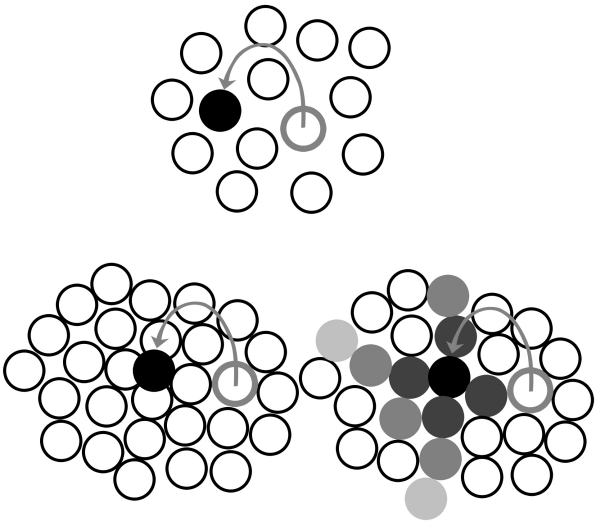

Figure 4: Graphical depiction of the concept of cooperativity. At high temperatures and low densities (top) a molecule is able to jump to a new position without rearrangement of neighboring molecules. At lower temperatures and higher densities some of its neighbors (shown shaded) must move cooperatively to make room. Graphic sketched according to visual representation from ref. [120], "SOFT CONDENSED MATTER" by R. A. L. Jones (2002): Fig 2.13 (p. 22), by permission of Oxford University Press (www.oup.com).

$$z^\star = \frac{N_A s_c^\star}{S_c}. \tag{31}$$

The sum of possible transition probabilities $W(T)$ can be expressed as a truncated geometrical progression, leading to

$$\bar{W}(T) = \frac{A}{1 - e^{-\frac{\Delta\mu}{k_B T}}} e^{-\frac{z^\star \Delta\mu}{k_B T}}, \tag{32}$$

where the denominator is nearly equal to unity for $\Delta\mu \gg k_B T$, such that its temperature dependence is negligible compared to the nominator and can simply be absorbed into a new proportionality factor $\bar{A}$. Plugging in the expression for $z^\star$ leads to

$$\bar{W}(T) = \bar{A} e^{-\frac{\Delta\mu s_c^\star}{k_B T S_c}} = \bar{A} e^{-\frac{C}{k_B T S_c}}, \tag{33}$$

where most of the constants have been subsumed in C and $\Delta\mu$ now describes the molar enthalpy.
Since the relaxation time is reciprocally related to the transition probability, this expression is easily rewritten to describe relaxation times. To obtain the VFT equation, however, one has to further approximate the configurational entropy. The configurational entropy is given by

$$S_c = \int_{T_0}^{T} \mathrm{d}T' \frac{\Delta c_p}{T'}, \tag{34}$$

where $\Delta c_p = c_p^{fluid} - c_p^{glas}$ is the specific heat of the glass forming liquid. Using an empirical approximation by Angell and Sichina [121], consisting of

$$\Delta c_p = \frac{K}{T}, \tag{35}$$

the configurational entropy can be written as

$$S_c = \frac{K\,(T - T_0)}{T T_0}. \tag{36}$$

It follows that the relaxation time τ is given by

$$\tau \sim \frac{1}{\bar{W}} \sim e^{\frac{CT_0}{k_B K (T - T_0)}}. \tag{37}$$

Thus we have finally obtained the VFT formula.

Therefore, according to this theory, the divergence of the the relaxation times can be traced back to the increasing size of the CRRs.

One problem with this approach, is that it lacks a fleshed out explanation to the morphology and composition of these CRRs. An idea to reconcile this problem has been given by Stanley et al. [122], who have used MD simulations to provide a connection between the configurational entropy and the average mass of mobile particle clusters, which occur in spatially heterogeneous dynamics, as seen in SPC/E water.

4.2 Entropy scaling

In section 5.2 we evaluate the relationship between the tetrahedral entropy and the correlation time of the incoherent intermediate scattering function for SPC/E water in confinement and in the bulk. The idea of finding a relationship between entropy and mobility of particles of a fluid is hardly new and has in many cases been shown to be quite successful.

The excess entropy S_{ex}, is the difference between the systems thermodynamic entropy and that of the equivalent ideal gas. The magnitude of excess entropy characterizes the extent to which static interparticle correlations, present due to interparticle interactions, reduce the number of microstates accessible to the fluid.

The excess-entropy scaling relation is a semiquantitative model (like the van der Waals equation of state), rather than a theory. However, it is useful for estimation of unknown transport coefficient and for providing guidelines for theoretical analysis [123].

An intuitive argument for a linear relationship between S_{ex} and a reduced diffusion coefficient $D_Z^\star$ has been given by Dzugutov [124].

Consider a simple liquid. The transfer of momentum and energy at high densities is facilitated by the short-range repulsive interatomic interactions, which can be described as binary collisions of hard spheres. The rate of this process is thus defined by the collision frequency which, according to Enskog theory [125], can be calculated for the temperature T and the number density ρ as

$$\Gamma_E = 4\sigma^2 g\,(\sigma)\,\rho \sqrt{\frac{\pi k_B T}{m}} \tag{38}$$

where m and σ are the atomic mass and the hard sphere diameter respectively. $g(\sigma)$, the value of the radial distribution function at the contact distance, represents the density of the immediate neighbors. In a real system, σ can be interpreted as the position of the first maximum of $g(r)$. Using σ and Γ_E^{-1} as natural units of length and time respectively, the diffusion coefficient D can be expressed in a dimensionless form as

$$D_Z^\star = D\Gamma_E^{-1}\sigma^{-2}. \tag{39}$$

In a system at equilibrium, the constraints imposed by the structural correlations reduce the number of accessible configurations per atom by a factor of $e^{S_{\text{ex}}}$. Furthermore, the rate of cage diffusion is defined by the frequency of local structural relaxations, which is proportional to the number of accessible configurations. Hence the $D_Z^\star$ and $e^{S_{\text{ex}}}$ must be connected by a universal linear relationship.

In 1977, Rosenfeld [126] originally noticed that casting the transport coefficients, D (self diffusion) and η (shear viscosity), of simple monatomic equilibrium fluids in a specific dimensionless form,

$$D_R^\star = D\rho^{\frac{1}{3}}\sqrt{\frac{m}{k_{\text{B}}T}} \tag{40}$$

$$\eta_R^\star = \frac{\eta}{\rho^{\frac{2}{3}}\sqrt{mk_{\text{B}}T}}, \tag{41}$$

makes them approximately single-valued functions of excess entropy. In his original publication he examines data for self-diffusion and shear viscosity using data from the hard-sphere (HS) model, a one component plasma (OCP), soft spheres (SS, in this case referencing an inverse 12th power potential), and a LJ-fluid, thus also showing the effect of adding an attractive part to the purely repulsive SS potential. To a good accuracy, $\log\left(D_R^\star\right)$ and $\log\left(y_R^\star\right)$ are nearly linear in the excess entropy for the three repulsive systems. Adding an attractive force at a given density ρ, and temperature T, to the inverse 12th power potential increases the diffusion coefficient. Basically the attractive term reduces the repulsion and decreases the size of the effective hard spheres, thereby increasing their diffusivity. At the same time the entropy is increased, with both effects quantitatively balancing each other (cf. fig. 1 from ref. [126]). A similar analysis holds also for the shear viscosity, except that there is also a long-range contribution to momentum transport from the potential in addition to the kinetic part. These data were corroborated by the plots of hundreds of simulation results for the reduced transport coefficients, of systems with quite disparate pair interactions [123], as functions of (minus) the reduced excess entropy, $s = -S_{\text{ex}}/(N_A k_{\text{B}}) > 0$. The quasi-universal behavior can be approximated by

$$D_R^\star \approx 0.6e^{-0.8s} \tag{42}$$

$$\eta_R^\star \approx 0.2e^{0.8s} \tag{43}$$

for all strongly coupled simple fluids, i.e. $s \gtrsim 1$.

This observation has predictive value because, while the transport coefficients of dense fluids can be difficult to estimate from first principles, the excess entropy can often be accurately predicted from liquid-state theory.

Similar observations to Rosenfeld's have been made by others as well. Dzugutov [124] looked at three model liquids of strongly differing local order, namely a LJ liquid (at different densities and at constant pressure), related to face-centered cubic pattern, a liquid characterized by predominantly icosahedral local order [127] and a liquid with local order topologically related to the primitive hexagonal lattice [128]. Included were also two liquid metals, Cu [129] and Pb [130], as well as hard sphere fluid.

He assumed the two-particle approximation to be sufficient to describe the entropy

$$S_2 = -2\pi\rho \int_0^\infty \mathrm{d}r \left(g\left(r\right) \ln\left(g\left(r\right)\right) - \left(g\left(r\right) - 1\right)\right) r^2, \tag{44}$$

and was able to show a linear relationship between $\ln\left(D^\star\right)$ and S_2. More precisely, the data closely clusters around

$$D_Z^\star = 0.049 e^{S_2}. \tag{45}$$

Interestingly this observation, i.e. scaling property, is not confined to the domain of conventional liquid dynamics. For the liquid with the predominantly icosahedral local order data was also taken from near its melting point, where a high rate of vacancy-driven activated hopping was observed [131]. And this is not the only non-conventional transport phenomenon Dzugutov investigated. Atomic diffusion in an equilibrium quasicrystal [132, 133], shows good agreement with the scaling law (45) as well. This process is driven by a generic form of structural relaxation, associated with incommensurate degrees of freedom.

The observation of general compliance with (45) implies that atomic diffusion is an entirely geometrical phenomenon which can be uniquely and universally accounted for by the frequency of binary collisions and the excess entropy, representing the measure of structural uncertainty. A more general conclusion is that the rate of exploration of the configurational space, which, in condensed systems, defines the diffusion rate, is controlled by the entropy [124].

While Dzugutov used microscopic parameters to scale the diffusion coefficient $D_Z^\star$ (cf. eq. 39) and arrived at a slightly different scaling law (cf. eq. (42) and eq. (45)), Rosenfeld used only macroscopic parameters for $D_R^\star$ (cf. eq. (40)) and was later able to show [123] that their results are in good agreement.

Rosenfeld [123] further states that the exponential forms only provide a good numerical representation to results which are fundamentally of a rational form which stems from series in powers of the density. The idea behind this is the following:

In the Green-Kubo formalism [134] the transport coefficients are given in terms of the time integral of an autocorrelation function for the appropriate current. E.g. the self-diffusion coefficient is given by

$$D = \int_0^\infty \mathrm{d}t \left\langle v_x\left(t\right) v_x\left(0\right)\right\rangle. \tag{46}$$

Expansion of the autocorrelation functions can be done in a Taylor series in powers of the time, with coefficients that are given in terms of space integrals, involving the equilibrium correlation functions of the system, and the pair interactions and their derivatives. For physical interaction potentials of the form $\phi(r) = r^{-l}$, with $l \leq 12$, the pair-correlation functions $g_\phi(r;\rho,T)$ can be represented by a single function $g\left(r\rho^{1/3}, S_{\text{ex}}/N_A k_{\text{B}}\right)$ with the excess entropy S_{ex} as parameter, with minimal errors [135]. The inverse power potentials in general rigorously obey density scaling, i.e.

$$g_l(r,\rho;S_{\text{ex}}/N_A k_{\text{B}}) = g_l\left(r\rho^{1/3};S_{\text{ex}}/N_A k_{\text{B}}\right). \tag{47}$$

The approximation of universality therefore comes from approximation of a given dense fluid by using a pair-correlation function from a soft r^{-l} potential. Rosenfeld states that he expects similar entropy scaling of integrals of higher-order correlation functions to be valid as well. To the extent that this kind of information is dominant in determining the Green-Kubo integral, one can expect entropy scaling for the transport coefficient.

However, the complexity of the expressions involved and the slow convergence of the time series essentially prohibit a direct test of this conjecture.

However, even lacking a rigorous theoretical underpinning this form of entropy scaling has enjoyed large successes and consequently attracted attention w.r.t. to not-so-simple liquids or under non-bulk conditions.

Mittal, Errington and Truskett [136] investigated the relationship between diffusivity and excess entropy in the hard sphere fluid under two- and one-dimensional confinement, with smooth interacting walls. They report that, although confinement strongly affects local structuring, the relationships between self-diffusivity, excess entropy, and average fluid density are, to an excellent approximation, independent of channel width or particle-wall interactions.

Similarly they studied the effect of confinement on excess entropy scaling for LJ fluids [137], concluding that the scaling laws of Rosenfeld and Dzugutov can collapse appropriately reduced self-diffusivities of the bulk and confined LJ fluids as a function of excess entropy over a wide range of thermodynamic conditions.

They further investigated entropy scaling with respect to a core-softened fluid [138], which is based on a pair interaction of the 12-6-LJ potential plus a Gaussian well, and shows similar anomalies as the SPC/E water model [139]. They found that when plotted along curves of constant density the self-diffusion coefficient showed entropy scaling of the form $D \sim e^{A(\rho)S_{\text{ex}}}$, where $A(\rho)$ is a T-independent parameter. They further investigated a binary LJ alloy [138] and noted that, at constant ρ, S_{ex} and $-(TS_c)^{-1}$, where S_c denotes the configurational entropy, are linearly related and therefore contain the same thermodynamic information about the supercooled fluid (at least over all conditions for which data was available [140, 141]).

Fomin and Ryzhov [142] note that in the case of core-softened potentials [139, 143] the validity of Rosenfeld scaling depends of the thermodynamic path, as it is successful along isochors, but breaks down along isotherms.

Sharma, Chakraborty and Chakravarty [144] studied entropy, diffusivity, and structural order in liquids with waterlike anomalies. In their work they approximate the excess entropy by the pair correlation entropy S_2 and, generalizing the dimensionless diffusivity $D_Z^\star$ to a binary liquid, show a strong linear dependence of $\ln\left(D_Z^\star\right)$ on S_2 for liquid silica.

Krekelberg et al. [145] have generalized the dimensionless form of the self-diffusion coefficient and were able to show via MD simulations that this quantity is approximately a single-valued function of

excess entropy for a range of model one- and two-component fluid mixtures, demonstrating that the "generalized Rosenfeld" scaling applies more broadly than other simple approaches such as Enskog theory or empirical scalings based on the pair-correlation contribution to the excess entropy. The approach however breaks down for highly asymmetric hard-sphere mixtures for packing fractions near the freezing transition, as well as for Gaussian-core mixtures, where the softness of the interactions combined with the size asymmetry gives rise to significant decoupling of the single-particle dynamics of the species.

Entropy scaling in the form of Rosenfeld has been tested with regard to different water models [146, 147, 148, 149, 150] as well, and not only with respect to the diffusivity, but also concerning observables such as the correlation time of the coherent intermediate scattering function [146]. The main points regarding these studies are mentioned in the discussion of the chapter concerning the simulation and evaluation of SPC/E water in cylindrical pores (cf. section 5.2.3).

4.3 Binary mixtures in confinement

The main theoretical approaches to binary mixtures in confinement are given by the random field Ising model (RFIM), first proposed by Brochard and De Gennes [151, 152], suggesting that the effect of a containing gel on a liquid mixture should be much like a random field, the single pore model (SPM) by Liu et al. [153], which focuses on the wetting properties of a liquid mixture in a pore geometry, and finite size scaling.

In a bulk system near to a critical point, the correlation length, ξ, of order parameter fluctuations, in the system is well described by a function of the form

$$\xi\left(t, H; L=\infty\right) \sim |t|^{-\nu} \, \Xi_{\pm}\left(H\,|t|^{-\Delta}\right), \tag{48}$$

where $t = (T - T_c)/T_c$, T_c is the critical temperature, $\Xi_{\pm}$ a scaling function where $\pm$ refers to $t > 0$ and $t < 0$ respectively, H is the applied field, L denotes the system size, and $\Delta = \beta + \gamma$ is a sum of critical exponents. The behavior of other quantities such as the specific heat, magnetic susceptibility, and isothermal compressibility are also dominated by a divergent function when near the critical temperature, with e.g. the specific heat C, or rather the singular part of the specific heat C_s, given by

$$C_s\left(t, H; L=\infty\right) \sim |t|^{-\alpha} \, C_{\pm}\left(H\,|t|^{-\Delta}\right), \tag{49}$$

with scaling function $C_{\pm}$. When the system size L is large compared to the correlation length, $L \gg \xi$, no significant finite-size effects should be observed. On the other hand, for $L \leq \xi$ the system size will cut off long-distance correlations, so that an appreciable finite-size rounding of critical-point singularities is to be expected. Since the bulk correlation length scales with (48), the finite-size scaling combination is naturally $L/|t|^{-\nu}$. Thus, one assumes

$$\xi\left(t, H; L\right) \sim |t|^{-\nu} \, \hat{\Xi}_{\pm}\left(H\,|t|^{-\Delta}\,; L\,|t|^{\nu}\right), \tag{50}$$

$$C_s\left(t, H; L\right) \sim |t|^{-\alpha} \, \hat{C}_{\pm}\left(H\,|t|^{-\Delta}\,; L\,|t|^{\nu}\right), \tag{51}$$

with scaling functions $\hat{\Xi}_{\pm}$ and $\hat{C}_{\pm}$, and similar expressions for the other quantities.

In confinement the pore structure limits the growth of the correlation length, and a crossover to $d_{\text{conf.}}$-dimensional behavior occurs near the shifted critical point. For a planar pore system e.g., a shift of

$$L^{-1/\nu} \sim \left|T_c - T_m\left(L\right)\right| / T_c \tag{52}$$

occurs [154], where $T_m(L)$ is the position of the shifted maximum and L is the pore width of the system. An extensive review of finite size scaling theory can be found in [155].

However, in general real materials will possess complex geometries, which may be locally cylindrical or planar, but have connections and correlations between pore sections - therefore the use of the RFIM. The idea behind the connection to the RFIM is that when the correlation length of the gel matrix is short compared to the correlation length of the mixture, the presence of the gel can be interpreted as a short-ranged random field acting on the fluid mixture. There are experimental observations supporting both the RFIM [156], and the SPM [157, 158], and indicating that neither theory is actually sufficient [57]. The fact that RFIM theory should only be relevant if the correlation length of the field is very short, i.e., much shorter than the thermal correlation length of the fluid itself is one weakness of this approach. Further it is also implicit in the RFIM that the field itself does not occupy space, excluding the presence of the spins, and thereby interfering with their exchange interaction. In many real systems this is not a sensible assumption w.r.t. the pore matrix.

However, clearly the wetting behavior of binary fluids is crucial for the evolution of systems in confinement. In 1977, Cahn [159] predicted that sufficiently close to the critical point in a binary system in the unstable two-phase region in contact with a third phase, e.g. a glass wall, one of the components would preferentially wet the third phase with a macroscopic layer, and the importance of wetting has since been validated in a number of experimental studies [158, 160, 161, 162, 163, 164].

In the following section the main conditions and results of the SPM by Liu et al. [153] are introduced.

4.3.1 Single pore model

Liu et al. [153] decided to model the behavior of a binary liquid in the idealized case of a cylindrical pore by focusing on the wetting behavior. They assume a constant overall composition, as can be found in experiments on binary liquid mixtures confined in sealed Vycor samples, and a symmetric coexistence curve, so that the volume fraction occupied by each phase is $1/2$.

Let the constituents of the mixture be denoted as α and β. Pore length and radius are given by L and r_0. Liu et al. [153] argue that in equilibrium there are two possibilities. Either the nonwetting phase is suspended in the pore middle, while surrounded by the wetting phase (corresponds to complete wetting, denoted by *cw*), or the pore is filled up to $L/2$ with α and from $L/2$ to L with β (corresponds to partial wetting, denoted by *pw*). Accordingly they established the free energies per length of the configurations by

$$F_{cw}/2\pi = \varphi_\beta r_0^2 \frac{\sigma_{\alpha\beta} + \bar{A}V(r_c)}{r_c} \tag{53}$$

$$F_{pw}/2\pi = \frac{1}{2}\varphi_\beta \bar{A}_2 r_0, \tag{54}$$

where $\varphi_\beta = 1/2$ is the volume fraction occupied by the β-phase, $\sigma_{\alpha\beta}$ is the α-β interfacial tension, $\bar{A}V(r)$ is the free energy per unit area, as a function of the inner radius r, and $\bar{A}$ and $\bar{A}_2$ are temperature-dependent Hamaker constants, corresponding to the interface potential and the free energy difference of filling the pore with β instead of α, respectively. End-cap contributions to the free energy are neglected, since they vanish with r_0/L. The bubble radius r_c is determined by choosing the effective interface potential for two concentric cylinders of radius r and r_0, $V(r)$, based on van der Waals forces and minimizing F_{cw}. To prevent unphysical divergences the authors have introduced a molecular cut-off a.

At the critical point the Hamaker constants and interfacial tension vanish. They vary with temperature according to

$$\bar{A} \sim A t^{\beta} \tag{55}$$

$$\bar{A}_2 \sim A_2 t^{\beta} \tag{56}$$

$$\sigma_{\alpha\beta} \sim \sigma_0 t^{\mu} = \sigma_0 t^{2\nu} \tag{57}$$

where A, A_2 and σ_0 depend on the material and

$$t = \frac{T_c - T}{T_c} \tag{58}$$

which is positive in the two-phase region.

The calculation of r_c allows for radial values not consistent with a tube configuration (two concentric cylinders stretching along the complete pore), but rather a series of bubbles of the β phase, while still remaining in the completely wetted regime. This configuration is referred to as "capsules". Further, when transitioning from a completely wetted to a partially wetted regime, one will usually encounter alternating bubbles of both species instead of a complete phase separation. This configuration will be referred to as the "plug" configuration.

Fig. 5 shows a sketch of these phases and the resulting phase diagram - based on the phase diagram as calculated by Liu et al. (cf. fig. 1 from ref [153]). The values used for the original calculation are roughly based on the case of nitromethane and carbon disulfide against glass, with exponents $\mu = 2\nu \approx 1.264$ and $\beta \approx 0.328$ based on the three-dimensional Ising model (cf. eq. (55) and (57)). The solid curve denotes the wetting transition, i.e. the crossover from complete to partial wetting behavior. The short-dashed curve shows the boundary between "tube" and "capsule" configurations. The long-dashed line can be viewed as a "spinodal line". Contrary to the case of an isolated cylinder, wetting forces from the pore walls can counter the destabilizing effect of surface tension, such that there is no Rayleigh instability, i.e. a cylinder of the β phase enclosed in the pore is stable against small sinusoidal perturbations. This area of stability is demarcated by the spinodal line, so that the tube configuration is actually metastable between the short-dashed and long-dashed line. Monette, Liu and Grest [165] have remarked that the condition for the "spinodal line" as originally proposed by Liu et al. [153] is not quite correct. Recalculations, however, show the exact same qualitative behavior. There is no fundamental change to the phase diagram.

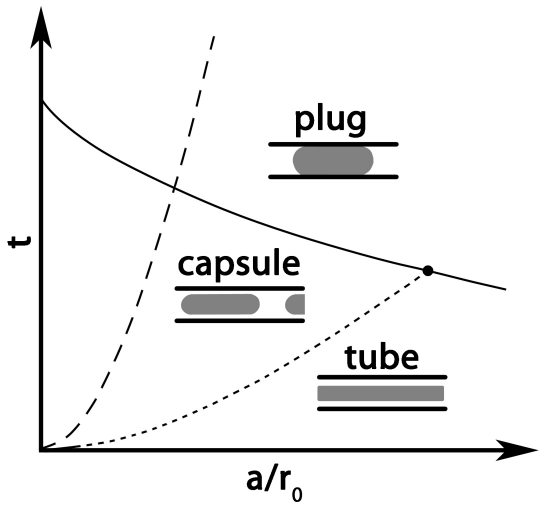

Figure 5: Wetting phase diagram for a binary liquid mixture confined in a cylindrical pore with radius r_0 and length $l \gg r_0$ as a function of reduced temperature t and inverse pore radius a/r_0. Adapted with permission from ref. [153]. Copyrighted by the American Physical Society.

The transitions as drawn in the phase diagram were evaluated numerically, but the qualitative behavior is easily explained. There exists a competition between surface tension and wetting forces. At the critical temperature there is no surface tension and wetting forces

prevail. As reduced temperature t increases, so does the difference in composition between the phases, leading to a growing interfacial tension and wetting potential. The interfacial tension, however, increases more rapidly (since $2\nu > \beta$, cf. eq. (55) and (57)), leading to a decrease of the wetting layer thickness. Since the composition is kept constant this either directly causes a transition to a "plug" configuration, or first to a "capsule" configuration and, if the temperature increases further, then to a "plug" configuration, where the interfacial area is minimized to the pore cross section.

5 Simulation results and discussion

This section of the thesis presents the results of the simulations and subsequent investigations. It is divided into three main parts, each of which discusses a particular aspect of water or aqueous solutions in confinement. However, all of them contain comparisons concerning the behavior of the fluid when confined by smooth, featureless interfaces as realized by external forces and atomically rough interfaces.

In the first part, 5.1, the different contributions of wall roughness, water model and interaction strength on water confined by planar interfaces is investigated. In the second part, 5.2, the structure and dynamics of SPC/E water in cylindrical confinements are studied in a broad temperature range. In this part of the thesis, simulations concerning confinement by atomistic pores were done by Felix Klameth, who coauthored the resulting publication [166]. In the third part the results of cylindrical confinement on a mixture of isobutyric acid and water is researched. This project was inspired by NMR measurements done on a iBA/water mixture confined to a silica nanopore [99] conducted by the AK Buntkowsky of the TU Darmstadt. The unexpected simulation result of the iBA clustering at the pore wall in turn prompted further experimental investigations (as of yet unpublished), which supported the simulation results.

As explained in the introduction, the make-up of these sections is always the same. In the beginning the simulation methods are presented. This is followed by the presentation of results and a discussion, after which the most important aspects of our findings are reiterated and set into context concerning their meaning for the scientific community.

5.1 TIP3P, TIP4P and TIP5P water at planar walls of differing roughness

This section of the thesis concerns itself with the structure and dynamics of water using different water models (TIP3P [31], TIP4P [32], TIP5P [33]) at ambient conditions, constrained by planar walls, which are either modeled by smooth potentials or regular atomic lattices, imitating the honeycomb-structure of graphene. The constraining walls exhibit differing hydroaffinity and lattice constants. Two different lattice constants are used, with the interaction strength chosen in such a way that the average potential as a function of distance from the wall is identical to that of the smooth walls for each category, i.e. hydrophobic or hydrophilic respectively. This allows us to distinguish the effect of interaction strength from the effect of wall roughness. Interaction with these walls takes place via the LJ potential.

Additionally, another type of wall is implemented, consisting of three atomic layers, which mimic hydrogen and oxygen atoms respectively. These waterlike walls thus attract the oxygen atoms of water as well as the hydrogen atoms.

The main results are that in the hydrophobic regime the smooth wall generally represents a usable abstraction of the atomically rough walls, especially for TIP3P, while in the hydrophilic regime there are strongly pronounced differences in structure and dynamics between all stages of wall roughness, especially w.r.t. motion perpendicular to the wall. For a small lattice constant however the smooth and the atomically rough wall still share a number of structural and dynamical similarities. Out of the three water models, TIP5P water shows the largest degree of tetrahedral ordering and is often the one that is the least perturbed by the presence of the wall.

In this section results pertaining to a directional evaluation of the incoherent intermediate scattering function (3.4) are shown. Deviations from the the targeted absolute value of the scattering vector $q = 2.3\,\text{Å}^{-1}$ are generally less than 1.42%.

5.1.1 Simulation methods

Water models

All MD simulations were performed using NAMD 2.8 [65], with the water models TIP3P [31], TIP4P [32] and TIP5P-Ewald [33]. Table 1 shows the corresponding parameters. The models TIP3P and TIP4P are an integral part of the NAMD-package, while we used a modified version of NAMD 2.8, created by David J. Huggins [167] to simulate the TIP5P water.

Wall types and simulation unit cell dimensions

All simulations were performed using the NVT ensemble with periodic boundary conditions. The cross section in the x-y-plane (parallel to the walls) is given by $51.577\times51.048\,\text{Å}^2$, while the z-dimension is in the range 33 to 39 Å, depending on the system (see below).

We used smooth walls (SW) and atomistic walls with a hexagonal atomic structure with the nearest-neighbor distance being either ≈ 1.418Å (C0 wall) or ≈ 2.127Å (C1 wall), such that there were 1008 or 448 atoms per unit cell. For each of these three wall types, we constructed a hydrophobic and a hydrophilic version, which interacts with water only via the LJ potential, with the parameters given in table 2. The interaction parameters of the atoms constituting the atomistic walls were chosen such that they lead to the same average energy well depth per area as given by the potential wall, while the $R'_{\text{min}}s$, R_{min} denoting the distance of the minimal potential energy c.f. table 1, were chosen such that at a distance of R^{SW}_{min} to the smooth wall the average distance of a given atom to the nearest atom of the atomistic wall equals $R^{C0/C1}_{\text{min}}$.

parameters	TIP3P	TIP4P	TIP5P
r_{OH}	0.9572	0.9572	0.9572
r_{OM}		0.15	
r_{OLP}			0.7
$\angle H-O-H$	104.52	104.52	104.52
$\angle LP-O-LP$			109.47
$q\,(O)$	-0.834		
$q\,(H)$	0.417	0.52	0.241
$q\,(M)$		-1.04	
$q\,(LP)$			-0.241
ε_O	0.152100	0.155000	0.178000
ε_H	0.046000		
$R_{\mathrm{min},2,O}$	1.768200	1.770100	1.737914
$R_{\mathrm{min},2,H}$	0.224500		

Table 1: Parameters used for the water models. Distances are given in Å, angles in degrees, charges in units of the elementary charge, and energies in kcal/mol. ε_i and $R_{\mathrm{min},2,i}$ characterize the Lennard-Jones (LJ) interactions, with the potential energy $V_{i,j}^{LJ}(r)$ given by $V_{i,j}^{LJ}(r) = \sqrt{\varepsilon_i \varepsilon_j}\left(\frac{R_{\mathrm{min},2,i}+R_{\mathrm{min},2,j}}{r}\right)^6\left(\left(\frac{R_{\mathrm{min},2,i}+R_{\mathrm{min},2,j}}{r}\right)^6 - 2\right)$.

LJ-parameters	hydrophobic	hydrophilic
ε_O	0.05331	0.45000
ε_H	0.02932	0.24747
$R_{\mathrm{min},O}$	4.08206	2.88486
$R_{\mathrm{min},H}$	2.49245	1.24450

Table 2: Parameters of the LJ interaction between the water molecules and the smooth walls. In the case of TIP4P and TIP5P water there is no interaction between the hydrophilic walls and the H-atoms. Distances are given in Å and the energy density in $\mathrm{kcal/mol} \times \mathrm{Å}^2$

For the smooth walls, the LJ interaction is implemented such that every infinitesimal wall area dA interacts with a given atom via the LJ-12-6 potential. The associated energy well depths (for the interaction with the oxygen atoms) are given by $\approx -1.38\,\mathrm{kcal/mol}$ and $\approx -8.22\,\mathrm{kcal/mol}$ respectively.

In the case of the hydrophobic wall we chose the parameters to be roughly consistent with the interaction of water and graphene [168]. The hydrophilic wall has an energy well depth deep in the hydrophilic region [169, 41], while $R_{\mathrm{min},O}$ was chosen to be roughly in the vicinity of the typical $O\ldots O$ separation distance in the $O-H\ldots O$ hydrogen bond [41]. An energy density of $\varepsilon_O = 0.45\,\mathrm{kcal/mol}\times\mathrm{\AA}^2$ for the oxygen-wall interaction was near to the highest possible value we could use in the NPT ensemble without the computer simulation giving way to unrealistic dynamical behavior.

The z dimension of the unit cell was determined by NPT-simulations at a pressure of 1 bar using the TIP3P water model and the smooth wall, with a given number of 2836 water molecules. The appropriate number of TIP4P and TIP5P water molecules was taken from the density-ratio of TIP3P to TIP4P and TIP5P water determined in NPT-bulk-simulations, and the same number of molecules was used for the atomistic walls. For TIP4P water, this led to 2772 molecules, and for TIP5P water to 2811 molecules. The resulting z dimensions were 36.48 Å for hydrophobic walls and 33.67 Å for hydrophilic walls. This difference is not important for the obtained structural and dynamical properties, since the influence of the wall is felt only to a distance of up to 15 Å, as shown by simulations with different water models and wall types [170, 171, 38, 172, 173, 12] as well as experiments [174].

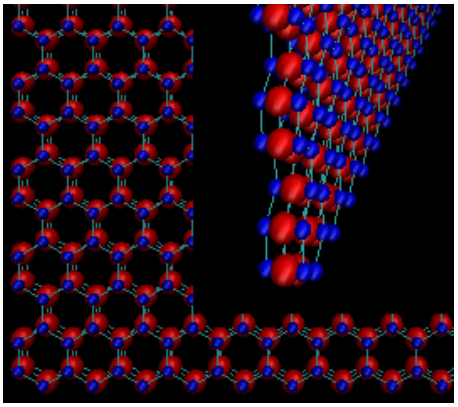

Figure 6: Illustrates the 3LW wall type. The basic design is shown both flat and at an angle.

In addition to the one-layer walls three-layer walls (3LW) were constructed as well, with parameters inspired from those of the H and O atoms of water molecules. These water-like walls consist of three atomistic sheets arranged directly over each other in a distance of 0.957 Å, where the atoms of the inner sheet emulate oxygen atoms (or lone pairs) w.r.t. charge and LJ-parameters, while the outer walls emulate hydrogen atoms. Fig. 6 illustrates the 3LW walls, which are specific to each water model. To increase the water-wall attraction the energy well depth of the LJ interaction of the "hydrogen" atoms was increased by 5%. The same parameters were used for both mesh sizes. The number of water molecules for each cell was determined in such a way that the z dimension of the unit cell became identical to that of the hydrophobic C0 and C1 walls, plus 2×0.957 to take into account the thickness of the three-layer wall. In order to achieve this, NPT simulations were performed for three different molecule numbers roughly in the target area. The three z extensions obtained from these simulations were used to deduce the required number of molecules by linear interpolation.

Molecular dynamics

All simulations were performed using rigid bonds for the water molecules and at a temperature of 296 K, using Langevin dynamics, with a coupling coefficient of $1.0\,\mathrm{ps}^{-1}$ and the hydrogen atoms included in the Langevin dynamics. Both LJ- and electrostatic interactions were cut off at a distance of 18.0 Å, with a switching distance of 15.0 Å, using the standard NAMD switching functions. The simulation time step was usually set at 1.0 fs, although in some of the simulations involving TIP5P water and the waterlike 3LW walls a time step of 2.0 fs was used.

5.1.2 Results

Hydrophobic walls

STATIC PROPERTIES

Density profile

Fig. 7 shows the density distributions perpendicular to the wall for the three hydrophobic walls (left hand side). These distributions show the familiar behavior, with pronounced peaks close to the wall and an amplitude that decays rapidly with increasing distance from the wall, so that the peaks cannot be discerned beyond 12 Å to 14 Å. Similar profiles were reported for a number of water models and hydrophobic walls [170, 38, 39, 40, 17].

These peaks indicate a layering of the water molecules close to the wall. By comparing the different density profiles, one can see that the layering is less pronounced for TIP5P water, with a broader hydrogen distribution at the first oxygen peak, owing to the higher degree of angular order for TIP5P water at the wall (see below). The wall type has little influence on the density profiles. The first oxygen peak broadens somewhat and the first hydrogen shoulder becomes less pronounced for TIP4P and TIP5P water when going from the smooth to the structured walls, but not for TIP3P water.

In the following, several quantities are presented, which have been evaluated by averaging over all molecules within the same peak. The peak boundaries used for these evaluations are indicated by a color change in fig. 7 (left hand side).

The upper right hand side of fig. 7 shows the density profile within one hexagon for the first two density peaks of TIP4P water at C0 and C1 wall types. TIP3P and TIP5P water behave similarly. For the C0 wall there is only a slight hint of the hexagonal structure, while for C1 the middle of the hexagon is favored by the oxygen atoms.

Angular distribution

Next, we evaluated the angular distribution of the water molecules. The results are shown in fig. 7 on the lower right hand side. To ease coordination with the density peaks the density distribution is shown in the uppermost panel. The deviation from the uniform distribution is shown in the middle panel. The deviation grows when approaching the wall, and several peaks are superimposed to this increase. The water model has a stronger influence on the shape of the curves than the wall type. Interestingly, the curves for TIP5P water show an additional local minimum close to the wall, which does not occur for the other two models. This indicates again that the structure of TIP5P water is less perturbed by the wall.

The bottom panel shows the ratio between the number of OH bonds oriented away from and towards the wall, with an angular deviation from the perpendicular direction of at most 30 degrees. The curves are similar for all water models and wall types, with the TIP5P water curves having slightly lower values. The molecules nearest to the wall have more OH bonds oriented towards the wall than away from it, indicating dangling bonds pointing to the wall. This is typical for hydrophobic walls [171, 175, 38, 40].

Tetrahedral order parameter

The tetrahedral order parameter is almost identical for all wall types and shows the same trend for all water models, with about 80 percent of the bulk value in the first peak and almost the bulk value in the second peak. Table 3 shows the values for the first three peaks.

DYNAMIC PROPERTIES

Fig. 8 shows the correlation times of the orientational autocorrelation function and the intermediate scattering function perpendicular and parallel to the wall.

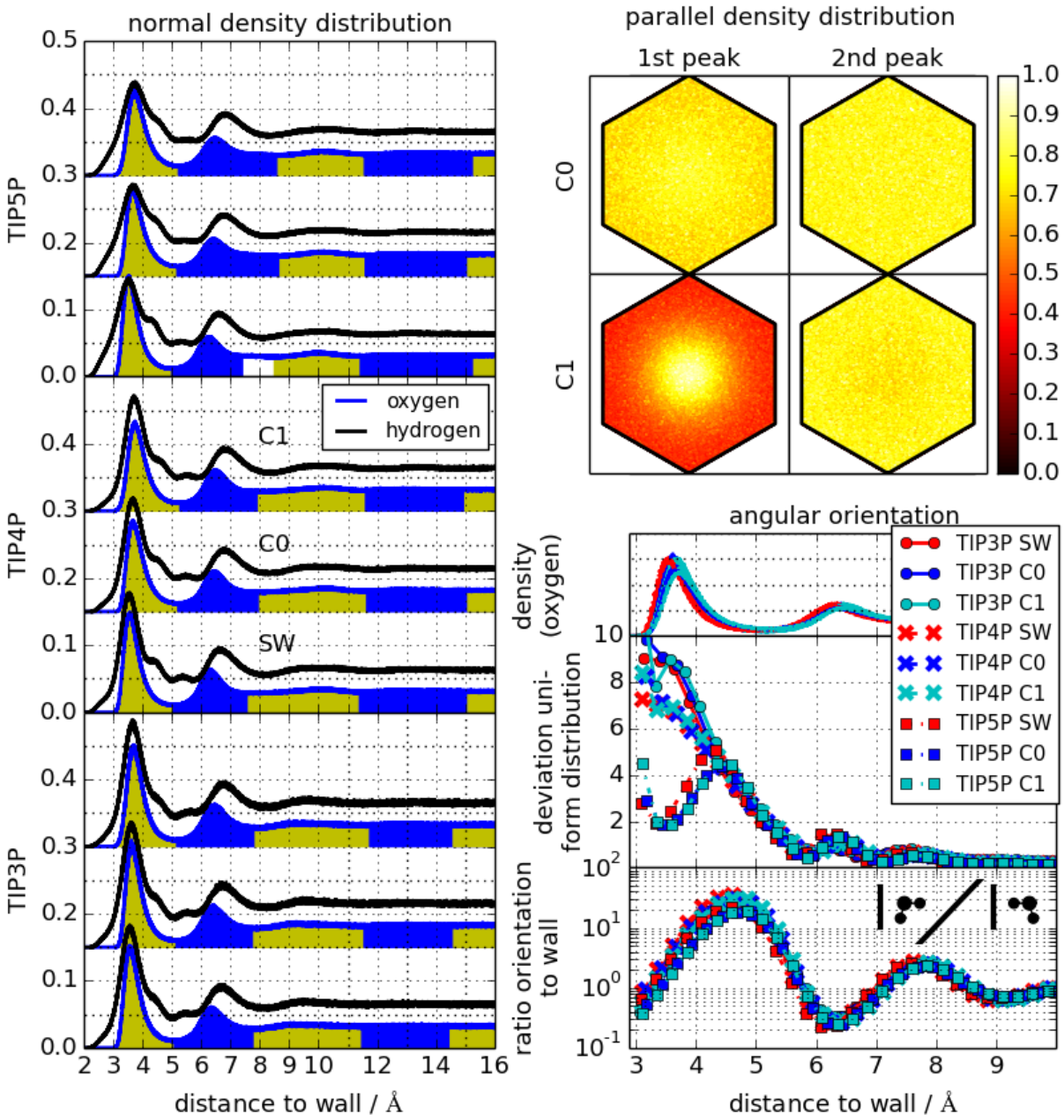

Figure 7: Density and orientation at the hydrophobic walls. Left hand side: Density distribution perpendicular to the walls (units: atoms per $Å^3$). The color changes indicate the peak boundaries used for the evaluation of various quantities. The density profiles are stacked, with the SW wall at the bottom and the C1 wall at the top. Right hand side, upper panels: Density distribution of water oxygen atoms, parallel to the wall and within the first and second density peak close to hydrophobic C0 and C1 walls (distribution shown w.r.t. wall hexagons). Data for the TIP4P water is shown. TIP3P and TIP5P water behave similarly. Right Hand side, lower panels (top to bottom): Density distribution of oxygen atoms (for easier comparison with density peaks); deviation from the uniform distribution; ratio of OH bonds oriented away and toward the wall with an angular deviation from the perpendicular direction of at most 30 degrees (cf. pictogram in upper right corner).

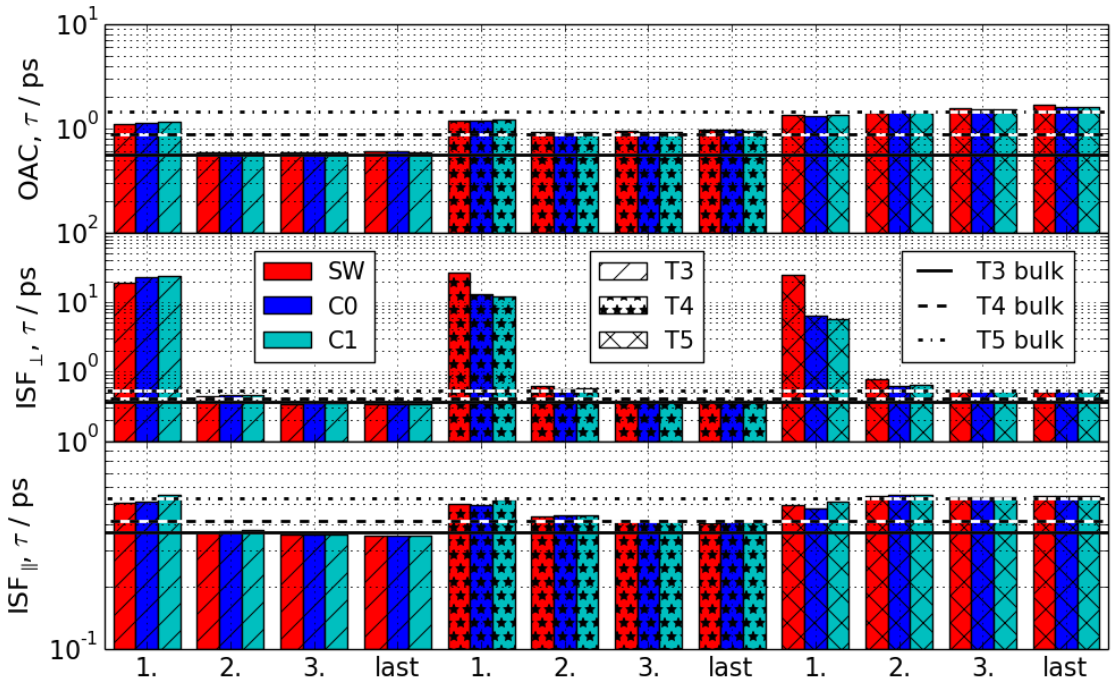

Figure 8: Correlation times of the orientational autocorrelation function and the intermediate scattering function perpendicular and parallel to the wall, for hydrophobic walls. The horizontal lines indicate the bulk values.

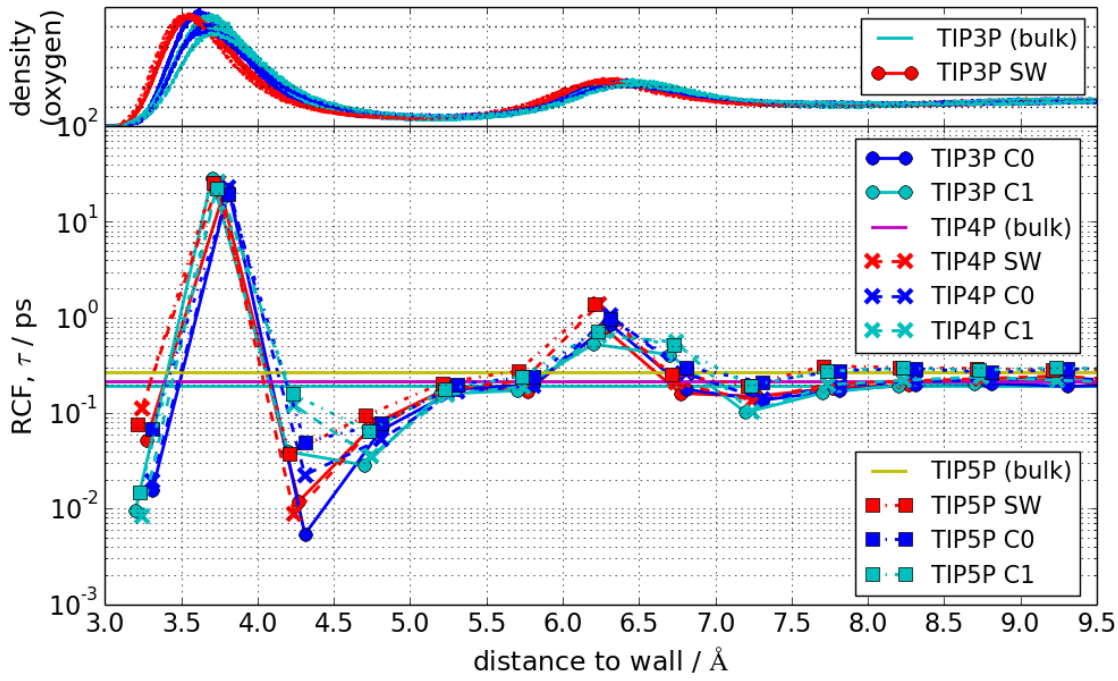

Figure 9: Correlation times of the residence correlation function for the hydrophobic walls.

water/wall	1st peak	2nd peak	3rd peak	bulk
TIP3PSW	0.48	0.54	0.55	
TIP3PC0	0.47	0.55	0.56	0.56
TIP3PC1	0.47	0.55	0.57	
TIP4PSW	0.51	0.62	0.64	
TIP4PC0	0.53	0.62	0.64	0.64
TIP4PC1	0.52	0.65	0.63	
TIP5PSW	0.51	0.64	0.64	
TIP5PC0	0.51	0.65	0.65	0.65
TIP5PC1	0.52	0.65	0.66	

Table 3: Tetrahedral order parameter within the first three peaks for the hydrophobic walls.

The correlation time of the orientational autocorrelation function shows little dependence on the wall type. It deviates from the bulk value mainly in the first peak, and this deviation is strongest for TIP3P water and positive for TIP3P and TIP4P water. For TIP5P water, which has the largest bulk value of the correlation time, the correlation time in the first peak is somewhat smaller than the bulk value. All these trends can also be seen in the intermediate scattering function parallel to the wall.

The correlation time of the intermediate scattering function perpendicular to the wall decreases with increasing distance from the wall for all three water models. Compared to the first density peak the second one already shows only little deviation from the bulk value. The correlation times differ only little for the different wall types in the case of TIP3P. For TIP4P and TIP5P, however, dynamics speed up somewhat when transitioning from the smooth to the rough walls, indicating that of the three water models TIP3P water is most effected by the rough walls, and TIP5P the least. The correlation times at the smooth wall are similar for all water models within the first peak.

Fig. 9 shows the correlation time of the residence correlation function, evaluated as the characteristic time water molecules stay within the considered slab of thickness 0.5 Å. The correlation time is increased close to the density maxima, being approximately two orders of magnitude larger in the first peak than in the bulk. The qualitative features of the curves are the same for all water models and wall types. Near the second peak all water models show slightly slower dynamics for the SW and C0 walls than the C1 wall. These data agree well with those of the intermediate scattering function perpendicular to the wall, but show more details since the graph has a finer spatial resolution. In particular, one can see that the correlation time is smaller than in the bulk when the local density is low or has a large gradient.

Hydrophilic walls

STATIC PROPERTIES

Density profile

Fig. 10 (left hand side) shows the density profile for the hydrophilic walls. Again, the peak boundaries used for the evaluation of mean correlation times and of the tetrahedral order parameter are also indicated. Just as for the hydrophobic walls, there is little difference between the density profiles for the SW and C0 walls, and a rapid decay of peak height with distance from the wall. The TIP5P water profiles differ again from those of the other water models by lower hydrogen peaks. For the C1 walls, the first oxygen peak splits into two smaller peaks, which relative to the density distribution contain similar amounts of oxygen. The relative height of the two peaks differs between the three water mod-

water/wall	1. peak	2. peak	3. peak	bulk
TIP3PSW	0.42	0.53	0.56	
TIP3PC0	0.43	0.53	0.55	0.56
TIP3PC1	0.38 | 0.49	0.53	0.56	
TIP4PSW	0.47	0.61	0.64	
TIP4PC0	0.48	0.61	0.65	0.64
TIP4PC1	0.40 | 0.58	0.61	0.63	
TIP5PSW	0.44	0.61	0.68	
TIP5PC0	0.46	0.60	0.65	0.65
TIP5PC1	0.39 | 0.60	0.58	0.64	

Table 4: Tetrahedral order parameter within the first three peaks for the hydrophilic walls.

els. All peaks are considerably higher than for the hydrophobic walls, and they are closer to the wall. While there were shoulders and small peaks of the hydrogen density between the first two oxygen peaks for hydrophobic walls, there are now clearly pronounced hydrogen peaks. Two or three distinct hydrogen peaks near the wall and a tapering off of the density oscillation beyond 12 Å was also reported by other authors who performed MD simulations for hydrophilic walls [176, 170, 172, 40, 39], and for experiments [177].

A look at the positions of the oxygen atoms relative to the hexagonal lattice of the wall shows that the oxygen atoms of the first peak for the C0 wall and the first part of the double peak for the C1 wall are concentrated at the center of the hexagon, and those of the second part of the double peak for the C1 wall are situated at the corners of the hexagon, see fig. 10 (upper panels, right hand side). The oxygen atoms in the next peak show also a slight preference for the corners of the hexagon.

Angular distribution

The deviation from the uniform distribution is shown in fig. 10 (lower panels, right hand side). As for the hydrophobic walls, this deviation increases when approaching the wall and shows several peaks. In particular the first peak is higher than for hydrophobic walls. In contrast to the hydrophobic walls, the wall type has a larger influence on the curves than the water model, with the C1 curves having considerably smaller peaks than those for the other wall types. The C1 curves as well as all TIP5P water curves show an initial increase with increasing distance from the wall. After the first density peak the TIP3P water curves are on average slightly below those for the other water models.

The ratio of OH bonds pointing away from and towards the wall is shown in the bottom panel of fig. 10 (right hand side). It shows a strong alignment away from the wall in the first peak, as expected for a hydrophilic boundary (not containing proton acceptors) [38, 178]. The alignment reverses, though less strongly, in the second peak. Again the curves for the C1 walls differ from the SW/C0 walls, even showing some dangling bonds close to the wall, as observed for hydrophobic walls.

Tetrahedral order parameter

Table 4 shows the tetrahedral order parameter within the first three peaks. It behaves very similar to the hydrophobic case, with deviations from the bulk value occurring mainly in the first peak. This deviation is stronger than for hydrophobic walls. For the C1 wall, the values for the two sub-peaks are given separately, showing a considerably smaller order parameter in the first sub-peak.

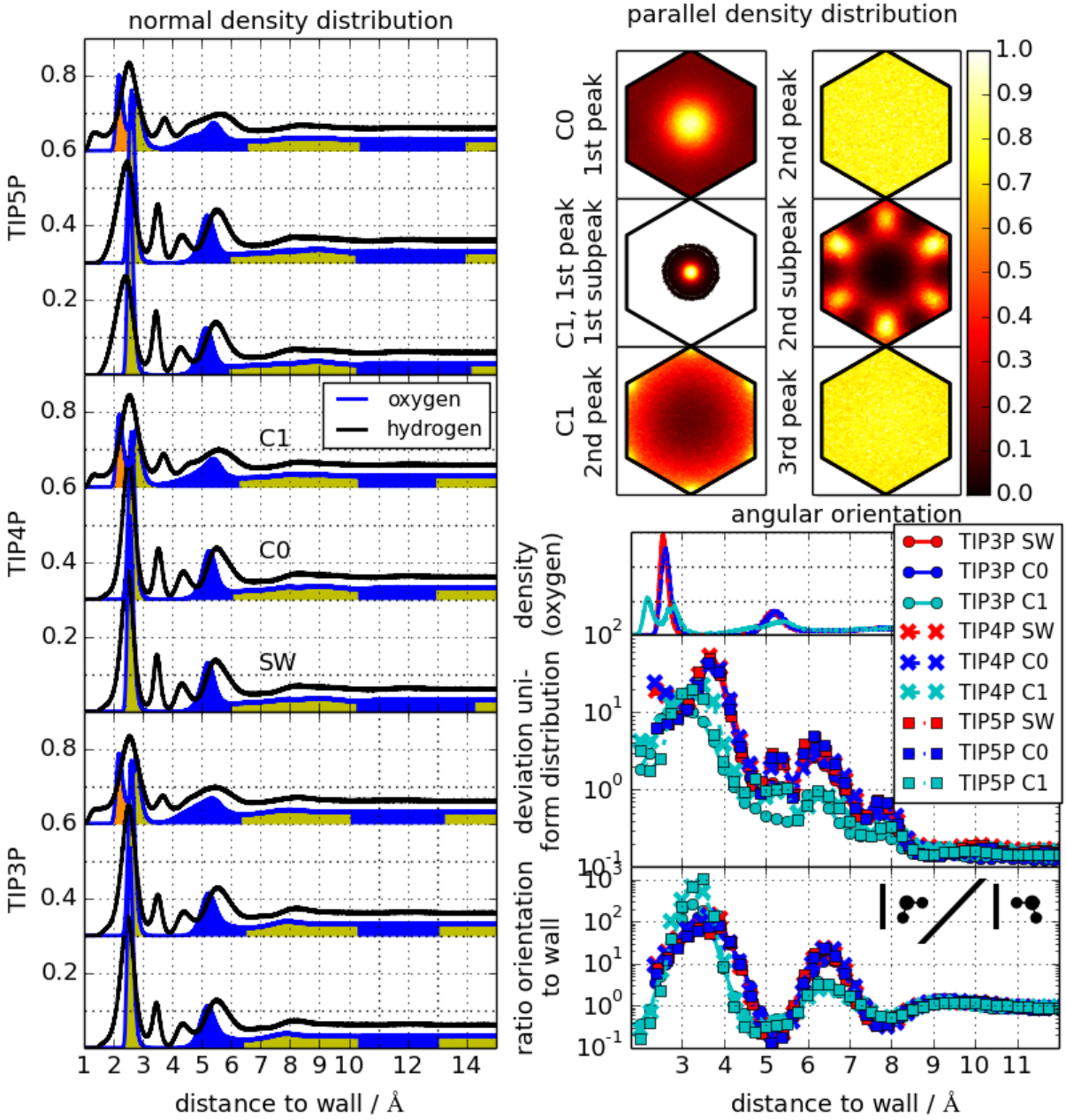

Figure 10: Density and orientation at the hydrophilic walls. Left hand side: Density distribution perpendicular to the walls (units: atoms per $Å^3$). The color changes indicate the peak boundaries used for the evaluation of various quantities. The density profiles are stacked, with the SW wall at the bottom and the C1 wall at the top. Right hand side, upper panels: Density distribution of the water oxygen atoms parallel to the wall. Data is shown for TIP4P water and the first and second density peak (C0) as well as the third density peak for C1. The hexagonal shape represents the wall hexagonal lattice of the wall. TIP3P and TIP5P water behave similarly. Right Hand side, lower panels (top to bottom): Density distribution of oxygen atoms (for easier comparison with density peaks); deviation from the uniform distribution (plotted semi logarithmically for better resolution of the peaks); ratio of OH bonds oriented away and toward the wall with an angular deviation from the perpendicular direction of at most 30 degrees (cf. pictogram in upper right corner).

DYNAMIC PROPERTIES

Fig. 11 shows the correlation times of the orientational autocorrelation function and the intermediate scattering function perpendicular and parallel to the wall. For the C1 walls, the correlation times for the two sub-peaks of the first peak are shown.

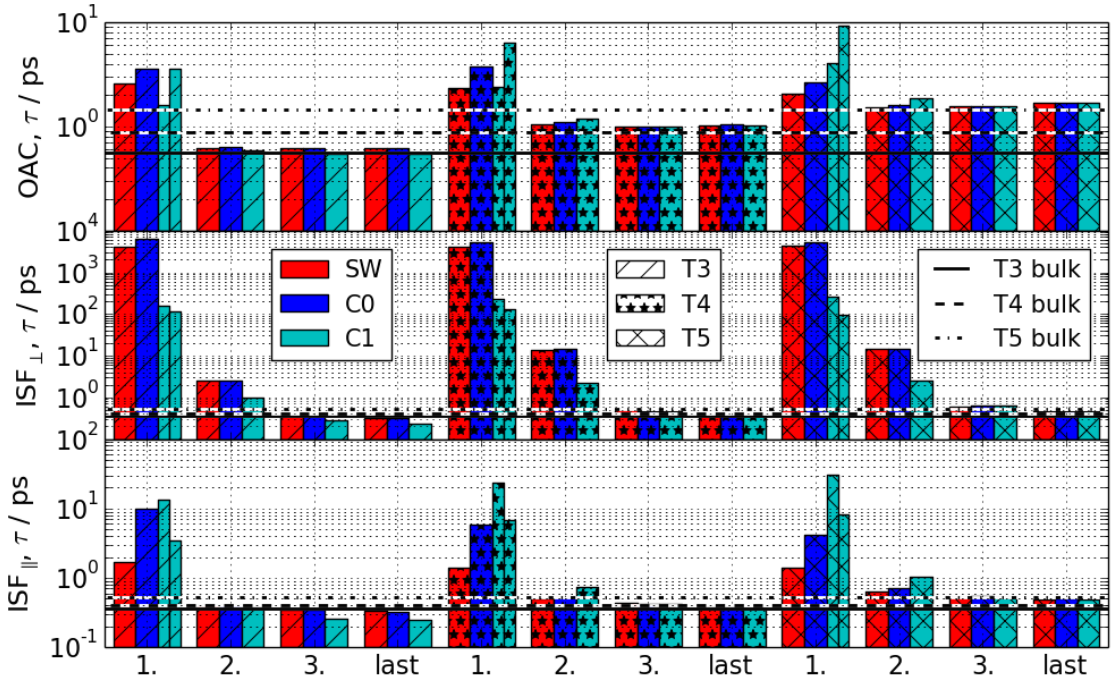

Figure 11: Correlation times of the orientational autocorrelation function and the intermediate scattering function perpendicular and parallel to the wall, for hydrophilic walls. The horizontal lines indicate the bulk values.

Similarly to the hydrophobic walls, the orientational autocorrelation function deviates from the bulk value mainly in the first peak, with this deviation being larger than for hydrophobic walls. In contrast to the hydrophobic walls, the correlation time for the first peak is also increased for TIP5P water. The correlation time in the first peak is shortest for TIP5P water, at least with regard to SW/C0 walls, therefore also showing the smallest deviation from the bulk value. For C1 walls the correlation time is longer in the second sub-peak than in the first and smallest for TIP3P water.

The correlation times of the intermediate scattering function evaluated perpendicularly to the wall are shown in the middle panel of fig. 11. These times decrease with increasing distance from the wall. In the first peak, the correlation times for the different water models agree very well in perpendicular direction, with the C1 wall showing by far the fastest dynamics, and the other two wall types leading to correlation times four orders of magnitude larger than in the bulk. In the parallel direction, the system with the SW wall shows the fastest dynamics, and the correlation times for the other two wall types differ between the different water models.

Fig. 12 shows the correlation times of the residence correlation function, evaluated as the characteristic time water molecules stay within the considered slab of thickness 0.5 Å. All water models and wall types show the same qualitative features. The C1 walls differ from the other two wall types by having lower maxima in the first two peaks and a higher minimum between these two peaks. This correlates with oxygen density being lower in the first two peaks than for the other two wall types, and higher between the first two peaks.

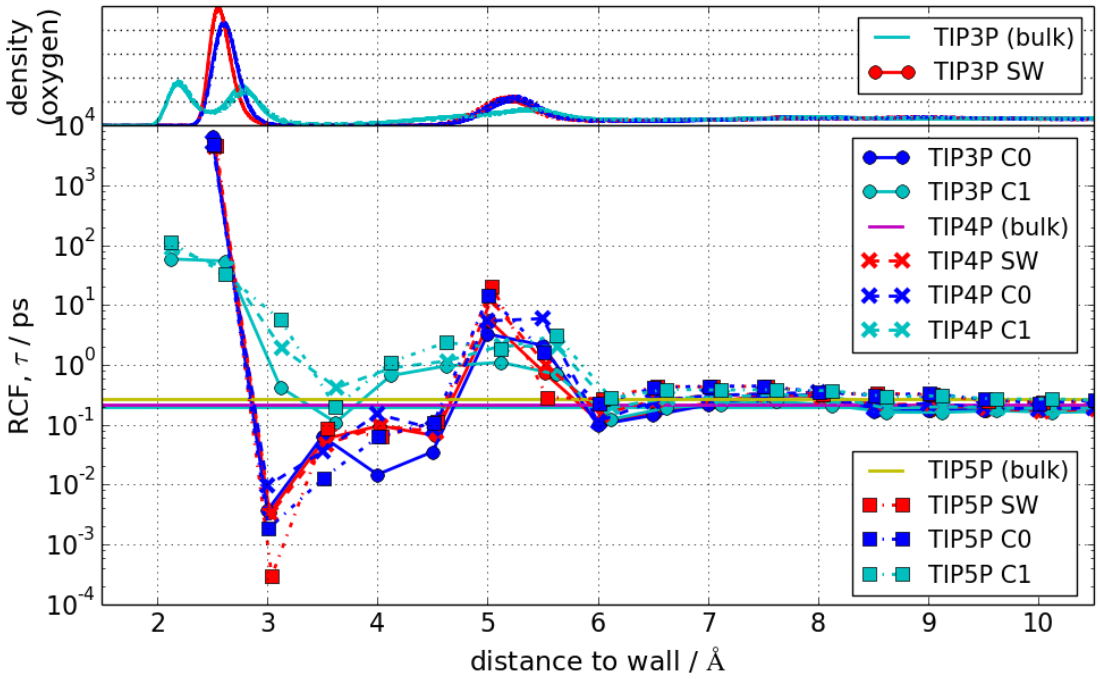

Figure 12: Correlation times of the residence correlation function for the hydrophilic walls.

Waterlike walls

STATIC PROPERTIES

Density profile

Fig. 13 (left hand side) shows the density profile for the waterlike walls. The first oxygen peak is sharper than for the other wall types. Again, TIP5P water has lower peaks than TIP3P and TIP4P water, indicating that the water structure is less modified by the wall. When going from C0 to C1 walls, the first peak broadens somewhat, and additional peaks occur.

Fig. 13 (upper panels, right hand side) shows the distribution of oxygen atoms parallel to the wall in the first four peaks. Regardless of wall type or water model the oxygen atoms strongly favor the center of the hexagons within the first peak. TIP5P water at the C0 wall shows less structure in the density, indicating again that the water structure is little modified by the wall.

Angular distribution

The deviation from the uniform distribution is shown in the fig. 13 (lower panels, right hand side). As for the hydrophilic walls, the wall type has a stronger influence on the curves than the water model. The C0 walls induce larger deviations from the uniform distribution than the C1 walls, near the wall TIP5P water deviates the least from the uniform distribution and TIP4P water the most.

The lowest panel of fig. 13 (right hand side) shows the ratio of OH links pointing away from and towards the wall with an angular deviation from the perpendicular direction of at most 30 degrees. This ratio is several orders of magnitudes larger (or smaller) than for the other wall types. In particular, in the first peak the OH-bonds are oriented very strongly towards the wall.

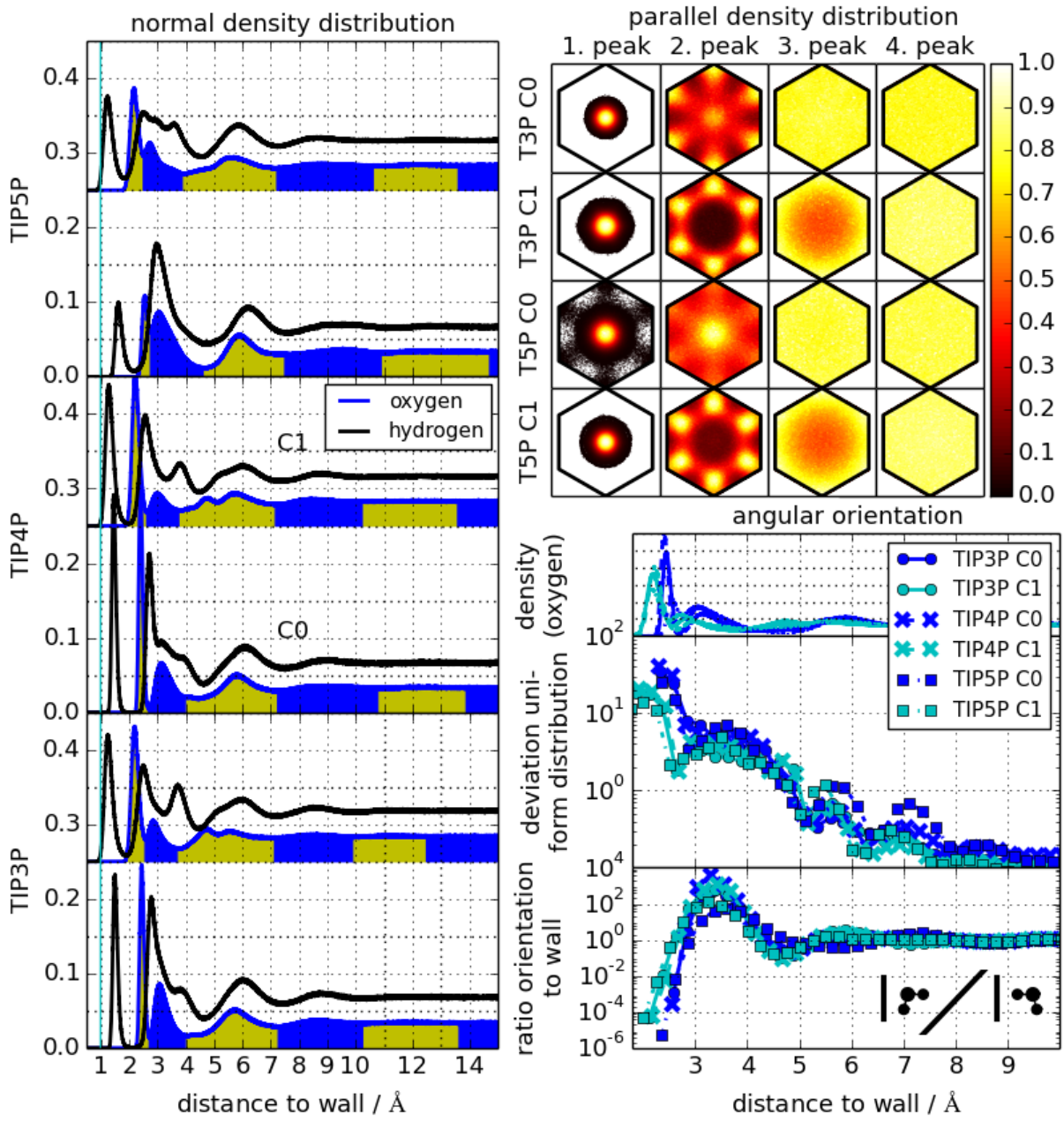

Figure 13: Density and orientation at the waterlike walls. Left hand side: Density distribution perpendicular to the wall (units: atoms per $Å^3$). The color changes indicate the peak boundaries used for the evaluation of various quantities. The density profiles are stacked, with the C0 wall at the bottom and the C1 wall at the top. The cyan line on the left hand side denotes the presence of the outer wall layer. Right hand side, upper panels: Density distribution of the water oxygen atoms parallel to the wall. Data is shown for TIP3P and TIP5P water and the first through fourth density peak. The hexagonal shape represents the wall hexagonal lattice of the wall. TIP4P water (not shown) behaves similarly to TIP3P water. Right Hand side, lower panels (top to bottom): Density distribution of oxygen atoms (for easier comparison with density peaks); deviation from the uniform distribution (plotted semi logarithmically for better resolution of the peaks); ratio of OH bonds oriented away and toward the wall with an angular deviation from the perpendicular direction of at most 30 degrees (cf. pictogram in lower right corner).

water/wall	1. peak	2. peak	3. peak	bulk
TIP3PC0	0.33	0.51	0.55	0.56
TIP3PC1	0.29	0.55	0.56	
TIP4PC0	0.29	0.61	0.61	0.64
TIP4PC1	0.30	0.61	0.63	
TIP5PC0	0.37	0.58	0.56	0.65
TIP5PC1	0.30	0.64	0.65	

Table 5: Tetrahedral order parameter within the first three peaks for the waterlike walls.

Tetrahedral order parameter

Table 5 shows the average value of the tetrahedral order parameter in each of the first three peaks. It shows the same qualitative behavior for all three water models. In the first peak, the order parameter is around half the bulk value, while the deviation from the bulk value is small in the other peaks. The order parameter value in the first peak is considerably smaller than for the other wall types.

DYNAMIC PROPERTIES

Fig. 14 shows the correlation times of the orientational autocorrelation function and the intermediate scattering function parallel and perpendicular to the wall.

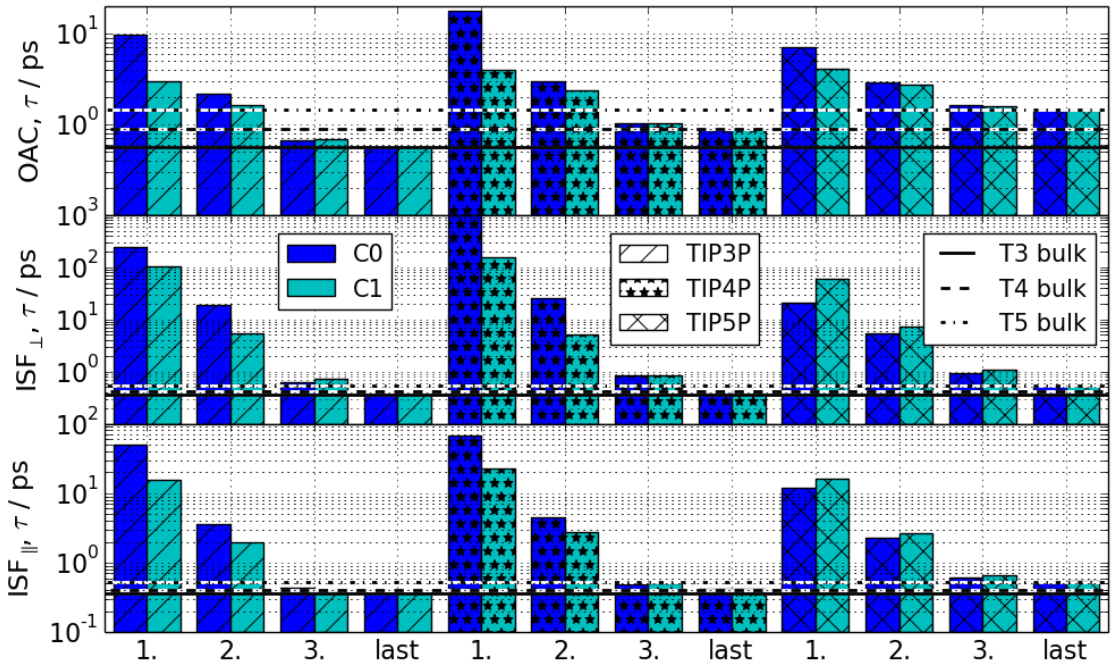

Figure 14: Correlation times of the orientational autocorrelation function and intermediate scattering function parallel and perpendicular to the wall, for waterlike walls. The horizontal lines indicate the bulk values.

As for the hydrophilic walls, all correlation times decrease with increasing distance from the wall. W.r.t. the C0 walls perpendicular movement is faster for the 3LW walls, while parallel movement is slower. In general the correlation times of TIP5P water in the first peak are shorter than for the other two

water models, and those of TIP4P water are largest. The exception is the correlation time of the C1 wall, where the TIP5P water correlation time is roughly 3% larger than that of TIP3P water, which is small compared to the 46% difference between the bulk values.

Except for the TIP5P water, the C0 walls lead to larger correlation times than the C1 walls. Compared to the hydrophobic and hydrophilic walls the correlation times in the directions parallel and perpendicular to the wall are very similar.

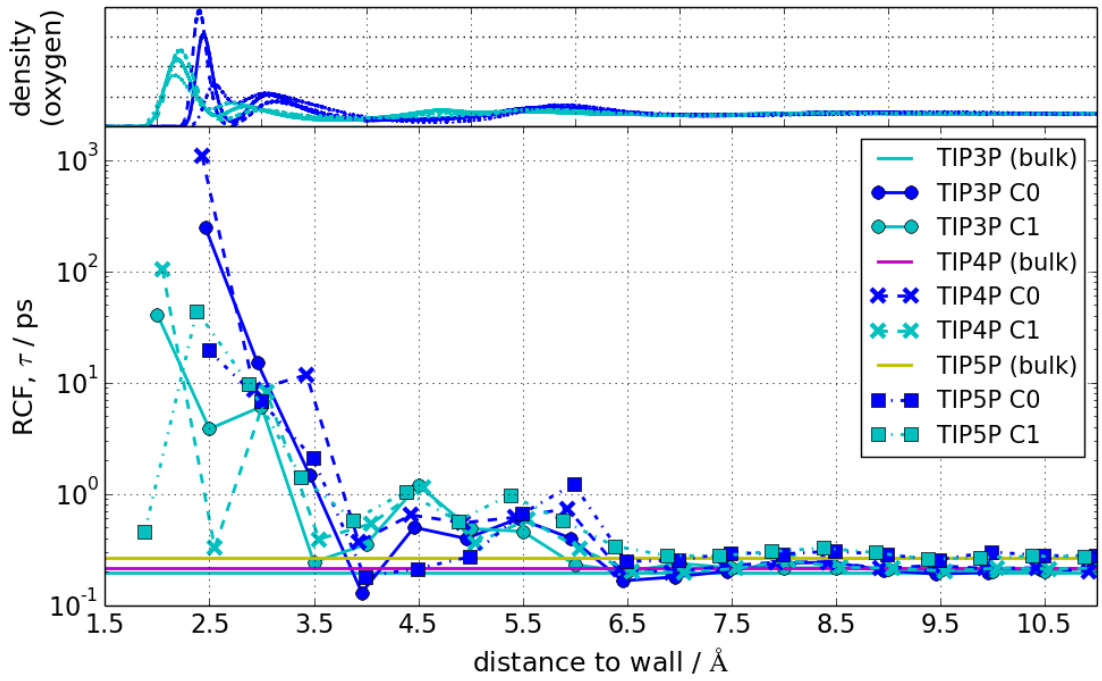

Figure 15: The correlation times of the residence correlation function for the waterlike walls.

Fig. 15 shows the correlation times of the residence correlation function, evaluated as the characteristic time water molecules stay within the considered slab of thickness 0.5 Å. The curves for all water models and wall types exhibit similar features. The dynamics is slowed down at the wall and sped up between peaks, converging towards the bulk values with increasing distance to the wall. For TIP3P and TIP4P water, correlation is slower close to C0 walls than close to C1 walls, while for TIP5P water the situation is reversed.

5.1.3 Discussion

In the following paragraphs, the results obtained for the different wall types and water models are compared, and related to other studies reported in the literature. The discussion of the static and dynamic properties are kept separate.

STATIC PROPERTIES

In general, hydrophilic and waterlike walls have a stronger influence on the structure of water than hydrophobic walls. The peaks of the density distribution of the oxygen atoms are more sharply pronounced at hydrophilic and waterlike walls compared to the hydrophobic walls, which has also been reported by other authors [98, 172]. However, for more elaborate potentials the opposite case of sharper peaks near hydrophobic walls has been reported as well [38].

For the hydrophilic and waterlike walls, the density profiles are strongly affected by the mesh size of the wall hexagons. The double peak for the hydrophilic C1 wall is reminiscent of the density profile of SPC/E water at a SiO_2 wall with a high density, $13.63\,OH/nm^2$ of hydroxyl groups [170]. The density of interaction points for the C0 and C1 walls are given by $38.28\,nm^{-2}$ and $17.02\,nm^{-2}$ respectively, thus being comparable in magnitude for the C1 wall, suggesting that for the hydrophilic wall the density profile is strongly influenced by the density of hydrophilic interaction points.

The density distribution within layers parallel to the wall reflects the honeycomb pattern of the wall atoms, and this effect is stronger for larger mesh sizes. This seems obvious for the hydrophobic and hydrophilic walls, where the potential energy depth of the wall-water interaction sites is inversely proportional to the density of these sites, but it is also observed for the waterlike walls, where the potential is independent of mesh size.

The angular orientation of water molecules is less affected by the wall for TIP5P water than for the other two water models, similar to the dynamical effects discussed further below. Of the three wall types, the waterlike walls have the strongest influence on the orientation of the molecules. We ascribe this to the influence of the electrostatic forces for waterlike walls, which affect the hydrogen atoms as strongly as the oxygen atoms. It is known from the literature that water molecules neighboring hydrophobic walls have dangling bonds pointing towards the wall [98, 175, 171, 178, 40, 38], while the OH-bonds point in the opposite direction close to hydrophilic walls [38, 98, 178]. We observe the same effect, with the exception of the hydrophilic C1 walls.

DYNAMIC PROPERTIES

For the hydrophobic walls the correlation times depend somewhat on wall type, but also differ noticeably between water models. For the hydrophilic and waterlike walls, which create sites of low energy for water molecules, the wall type has a considerable influence.

Water near hydrophobic walls shows faster dynamics than near hydrophilic or waterlike walls, consistent with what has been observed at crystalline hydrophobic and hydrophilic alkans or alcohols [38], or at graphite walls vs. hydrophilic SiO_2 walls with a high hydroxyl density ($13.63\,OH/nm^2$) [170], but not when comparing graphite walls and hydrophilic SiO_2 walls with a low hydroxyl density ($4.54\,OH/nm^2$). Considering that even our C1 walls have a higher density of water-wall interaction points than the high hydroxyl density SiO_2 walls, it is satisfying that our findings agree qualitatively with the high hydroxyl density case. Quantitatively, we observe in the first peak at hydrophilic smooth (SW) and C0 walls correlation times of the residence correlation function and the perpendicular intermediate scattering function which are around two orders of magnitude higher than for the corresponding hydrophobic walls, while the correlation times at the waterlike walls are in-between, spanning a large range. The correlation times of the orientational autocorrelation function are up to one order of magnitude higher for hydrophilic and waterlike walls than for hydrophobic walls. The correlation times of the parallel intermediate scattering function differ relatively little for smooth hydrophobic and hydrophilic walls and between one and one and a half order of magnitude for atomistic hydrophobic and hydrophilic walls. In general, dynamics parallel to the wall is faster than dynamics perpendicular to the wall (in the first peak). This has been observed for water at hydrophobic and hydrophilic walls [172] as well as for hard spheres at a hard wall [179].

In the following, we will try to understand the factors responsible for the mentioned differences in correlation times, and for some of the more subtle differences shown in 5.1.2. The strength and type of the water-wall interaction, the structure of the wall, and the properties of the water model all have an influence. Due to the setup of our study, where each of these factors is varied separately, we can disentangle these different contributions to some extent.

First, it seems obvious that, all other factors staying the same, an increase in attractive interaction with the wall will slow down translational motion of water molecules. This is confirmed when going from hydrophobic to hydrophilic smooth walls, or from hydrophobic to hydrophilic atomistic walls with the same atomic structure and mesh size. Partially this slowing down can be attributed to the attraction between wall atom and water molecule and partially to the increase in density in the first peak, such that neighboring water molecules hamper translational movement.

When increasing the mesh size of the hydrophobic and hydrophilic walls, the water-wall attraction per lattice atom is increased as well, while the average potential energy per wall area remains the same. Given the increased energy per contact, an increase in mesh size should lead to a slowing down of translational motion. Since an increase in mesh size makes the wall more rough, the trajectories of water molecules are probably less straight and have more collisions than for smoother walls, and this should also slow down motion. On the other hand, rougher walls provide more space and less contact points for water molecules, which could increase mobility. In fact, we found such an increased mobility, at least w.r.t. to perpendicular motion, when going from hydrophilic C0 to C1 walls. For TIP4P and TIP5P water the same is found for the transition from hydrophobic smooth to rough walls. But otherwise, our computer simulations and the simulations of other authors show that water moves slower near rougher walls when the average potential energy of both wall types with water is the same: Lee and Rosky [98] examined TIP4P water at smooth and atomically rough, i.e. 24 interaction points/nm^2, hydrophobic walls with the same average potential, finding that water molecules at the rough wall are slightly slower than those at the smooth wall. Scheidler, Kob and Binder [16] found that simple liquids move faster at non-attractive smooth walls than at non-attractive rough walls. Interestingly, both groups of authors found that water near hydrophobic walls can be faster than in the bulk. We observe this only for TIP5P water at hydrophobic SW and C0 walls, but not for the other water models, which we explain by our hydrophobic wall having a larger interaction energy with water than Lee and Rosky's. TIP5P water differs from the other water models by having larger bulk correlation times, indicating a stronger hydrogen bond network in the bulk, and apparently the mobility-increasing effect of disrupted hydrogen bonds is slightly stronger than effects that hamper water motion close to walls.

For the waterlike walls, we did not change the potential when changing the mesh size. Thus increasing the mesh size lowers the average potential per area, and consequently we observe for TIP3P and TIP4P water an increase in both parallel and perpendicular translational movement when going from C0 to C1 walls. Similarly, Argyris, Tummala and Striolo [170], using the SPC/E water model, report a decrease in translational motion when increasing the number of hydroxyl groups on a silica matrix. However, for TIP5P water we observe the opposite effect, with translational motion becoming slower for larger mesh size. Papavassiliou et al. [180], who used MD simulations to investigate slip vs. no-slip conditions at hydrophilic interfaces made a similar observation with regard to SPC/E water [34] on a MgO surface, when changing the lattice constants. They concluded that when preferential adsorption sites exist, which are sufficiently close to each other that water migration from one to the next can occur without requiring hopping events, hydrodynamic liquid slip occurs. In our case we correlate this effect with the in-plane density distribution, cf. fig. 13 (upper panels, right hand side), which shows that TIP5P water is much less trapped by C0 wall hexagons than TIP3P and TIP4P water, making TIP5P dynamics much faster than TIP3P and TIP4P dynamics near C0 walls. Near C1 walls, the in-plane density distribution and displacement parallel to the wall are comparable for all three water models. We attribute these phenomena to the fact that for the C0 wall the mesh size (around 1.4 Å) is far from the bulk nearest neighbor distance of the water molecules (around 2.7 Å), in combination with TIP5P water showing a stronger tendency to form networks, thus being less perturbed by a wall with a mesh size further from its internal structure.

Finally, let us discuss to some detail movement perpendicular to the walls, which is captured in the perpendicular component of the intermediate scattering function and in the residence correlation function. In the literature there are different reports about the effect of hydroaffinity on residence times. Lee and Rossky [98] report residence times of the same order of magnitude for their hydrophobic and hydrophilic systems, around 100 ps using TIP4P water, stating that the strength of pair interactions and local dynamics is not reflected in the residence times. Their hydrophilic system consists of a silica interface with a hydroxyl density of $4.62\,\mathrm{nm}^{-2}$, which is low when compared to our density of wall water interaction points. Argyris, Tummala and Striolo [170] investigated SPC/E water at 300 K at graphite, as well as SiO_2, where the crystal was cut along the (1 1 1) crystallographic face at different depths, therefore obtaining surfaces with a high and low density of hydroxyl groups. They report an increase of residence times at the graphite wall by one order of magnitude compared to the bulk, no increase at the wall with low density hydroxyl groups, and an increase by two orders of magnitude at the wall with a high density of hydroxyl groups. Their residence times at the graphite wall are comparable to ours at the hydrophobic surface. Li, Du and Yuan [39] calculated residence times for a 4 Å wide slab of SPC water on a pure water system and a hydrophilic and hydrophobic self assembled monolayer, with 34.71 ps, 9.64 ps and 10.68 ps, for the hydrophilic, hydrophobic and pure water systems respectively.

We observe an increase in the correlation times of the perpendicular intermediate scattering function of about one to one and a half orders of magnitude at the hydrophobic walls, between two and four orders of magnitude at the hydrophilic walls, and between one and a half and three orders of magnitude at the waterlike walls.

Although the residence times near hydrophobic walls are comparable in order of magnitude for all our systems and those reported in the literature, we see small systematic influences of wall type and water model. While the perpendicular motion of TIP3P water slows down slightly, when going from SW to C0 walls, TIP4P and TIP5P water speed up. Perpendicular dynamic properties change little when wall roughness is further accentuated, while motion parallel to the wall shows a minimal slowdown, indicating a larger preference of the water molecules to remain at the center of the wall hexagons, in agreement with the (parallel) density profiles of fig. 7 (upper panels, right hand side).

For the hydrophilic walls, the perpendicular correlation times near the atomistic C0 walls are larger than at smooth walls, while the correlation times at the C1 walls are noticeably shorter. This can be explained by the parallel density distribution as well. At the hydrophilic walls the preference w.r.t. positioning in relation to the hexagonal lattice structure of the wall is more pronounced than at the hydrophobic walls, influencing perpendicular dynamics as well. At the C0 walls the water molecules are less likely to find their way away from the wall unobstructed. This is not the case for the C1 walls, which is probably due to the difference in preferred water molecule position in the first and second part of the first density peak, c.f. fig. 10 (upper panels, right hand side), thus providing gaps where molecules can slip through. This underlines again that for hydrophilic walls details of the wall-water interaction have a considerable effect on correlation times.

5.1.4 Conclusion

In this section the influence of wall roughness, or mesh size of atomistic walls at a honeycomb structure as opposed to smooth potential walls, on the static and dynamic properties of different water models at ambient conditions has been investigated.

Dynamic and static properties vary in dependence on the density of wall-water interaction sites, the strength of these interactions, the details of the potential and the properties of the water model. TIP5P has a stronger inherent structure than TIP3P and therefore often responds differently. TIP4P is somewhere in between and shares different characteristics with both water models. All three water models show

pronounced density peaks close to the wall and a slowing-down of translational motion perpendicular to the wall. Translational motion parallel to the wall is slowed down much less, and is even minimally accelerated near hydrophobic walls for TIP5P water. Other authors [98, 16] found accelerated motion parallel to hydrophobic walls also with other water models, but in their simulations the water-wall interaction was weaker. Taking their results and our results together we can conclude that when walls are sufficiently smooth and water-wall interaction is sufficiently weak motion parallel to the wall will become faster than in the bulk for all water models, but for TIP5P water this happens most easily.

For hydrophobic walls and TIP3P water, we find that structural and dynamical properties of water agree for smooth walls and atomistic walls with a lattice constant significantly smaller than the distance between water molecules, when the interaction strengths are matched such that the average potential energy at a given distance from the wall is the same. For TIP4P and TIP5P, with a more pronounced inherent structure (cf. table 3 for the tetrahedral order parameter) there is a noticeable change in perpendicular dynamics when switching from a smooth to a rough wall, though a very small one when compared to the case of the hydrophilic walls. This change is again more pronounced for TIP5P water, compared to TIP4P. We thus extend earlier findings by Kumar et al. [42] who compared systems with purely repulsive smooth walls and smooth walls with a Lennard Jones potential, concluding that the properties of the confined liquid are only weakly dependent on the details of the confining potential.

For hydrophilic walls, which attract water molecules much stronger, the wall structure has a considerable influence on structural and dynamical properties of water, even when the walls are constructed such that the average potential energy at a given distance from the wall is the same. The approximation of an atomistic wall by a smooth potential works only when the lattice constant is significantly smaller than the distance between water molecules and when motion perpendicularly to the wall is considered. For larger lattice constants, the number of water-wall interaction points of our systems becomes comparable to the density of hydroxyl groups on hydrophilic silica surface modeled by other authors, and we find that motion parallel to the wall is strongly affected by wall structure since the wall structure creates preferred sites for water molecules. For the same reason, residence times of water molecules within a given layer close to the wall depend strongly on details of the wall structure.

For our ”waterlike” walls, which attract oxygen and hydrogen molecules with the same interaction strength as that between water molecules, a change of the lattice constant also changes the structural and dynamical properties of water. Interestingly, an increase in the lattice constant, which in this case implies a decrease of the average water-wall potential energy, does not necessarily lead to faster translational dynamics, as demonstrated in the case of TIP5P water. All these findings indicate that the dynamics of water near hydrophilic (or waterlike) walls is affected by several details of the wall, part of which accelerate and part of which slow down motion. In particular, when there are less interaction sites with a stronger energy, this on the one hand prevents the water molecules from moving away from these sites, but on the other hand the lower density of such sites leaves more space for motion. Which of these two effects dominates depends also on the extent to which the structure of water is modified at the wall. For these reasons, there are widely different findings in the literature (and also in our simulations) concerning the time scales for motion of water molecules near hydrophilic walls.

To conclude, the extent of abstraction used when modeling water near surfaces, as for instance in biological systems, must be chosen carefully and with regard to the water model used. While hydrophobic interactions may be averaged to a certain degree without compromising the characteristic response of the system, hydrophilic interactions must be implemented more carefully, testing the robustness of the findings with respect to different versions of the model that appear equally realistic.

5.2 SPC/E water confined in cylindrical pores

In this part of the thesis molecular dynamics simulations of SPC/E [34] water in amorphous silica pores and amorphous ice pores with radii slightly larger than 10 Å are evaluated with regard to structure and dynamics of the water. In addition the behavior of the water is observed in completely smooth pores such that the potential felt at a given distance from the pore wall is an averaged atomic potential. As compared to rough walls, smooth walls induce stronger distortions of water structure for both silica and ice confinements. On the other hand, unlike the smooth pores, the rough pores strongly slow down water dynamics at the pore wall. The slowdown vanishes when reducing the atomic charges in the wall, i.e., when varying the hydroaffinity, while keeping the surface topology, indicating that it is not a geometric effect. Rather, it is due to the fact that the wall atoms provide a static energy landscape along the surface, e.g. fixed anchor-points for hydrogen bonds, to which the water molecules need to adapt, blocking channels for structural rearrangement. In the smooth pores, water dynamics can be faster than in the bulk liquid not only at the pore wall, but also in the pore center. Changes in the tetrahedral order rather than in the local density are identified as the main cause for this change of the dynamical behavior in the center of smooth pores.

5.2.1 Simulation methods

MD simulations for the completely smooth and the atomically rough pores were carried out using the NAMD and the GROMACS simulation package, respectively.

In both cases the SPC/E water model with rigid bonds was used, with a cutoff at 12 Å and a switching distance of 0.0 Å (GROMACS) or 10^{-10} Å (NAMD). A time step of 2 fs was utilized. The Coulomb interactions were calculated using the Particle-Mesh Ewald sum. Periodic boundary conditions were applied. For the silica pore the LJ interaction parameters between silica and water were established employing the LJ parameters given by Bródka and Zerda [181] together with the Lorentz-Berthelot mixing rules.

Smooth pores

MD simulations for the smooth pores were done using NAMD 2.8 [65], with $N = 2161$ water molecules in a "silica-like" pore and $2856 \leq N \leq 3016$ water molecules in an "ice-like" pore. In contrast to GROMACS, NAMD enables an implementation of smooth walls. An ice-like pore was implemented by a radially symmetric force using a tclBC-script. The force was calculated numerically at radial intervals of 0.05 Å by on average assigning the same LJ interaction potential to a given volume element as in the corresponding atomistic pore. In the case of the silica-like pore we proceeded analogously, assuming a surface density of 4 nm^{-2} silanol groups. Both types of smooth pores have a radius of 12.5 Å.

Simulations at constant temperature were done with the Langevin thermostat [65]. Constant pressure simulations were carried out using the Langevin-Piston [68] method. All temperatures had a minimal equilibration time of 20 ns in the NPT ensemble before the appropriate density was determined and NVT simulations were performed. For the water-like pore NPT simulations were conducted in the bulk, after which the appropriate number of water molecules were excised for the pore. NVT simulations were done using the Langevin thermostat, with a coupling coefficient of 1.0 ps^{-1} and with the hydrogen atoms included in the Langevin dynamics.

Atomically rough pores

MD simulations of the rough pores were done using the GROMACS [66] simulation software package. The temperature was set using the Nosé-Hoover thermostat [182, 183].

Since constant pressure simulations cannot be performed when a fraction of the atoms have fixed positions, three overall densities were used in the NVT simulations for the amorphous silica pore, two of which resulted in core densities similar to those obtained in the NPT simulation for the smooth pore. Only results for the best density match with the smooth pore are shown. The atomistic silica pore has a radius of 11 Å. More details about this matrix can be found in [184].

In the case of the amorphous ice pore, SPC/E bulk water was simulated in cubic systems comprising $N = 11890$ water molecules. The pressure P of 1 bar was maintained at a given temperature using the Parrinello-Rahman barostat [185]. After NPT equilibration, the position-restraint feature of GROMACS was used to pin the water molecules outside a cylindrical volume, thus creating the amorphous ice pore. Pinning was done via an harmonic potential with a force constant of $10^6\,\mathrm{kJ}/\left(\mathrm{nm}^2\mathrm{mol}\right)$, which was applied to oxygen atoms at a distance larger than the desired confinement size from the symmetry axis of the simulation box. More details can be found in recent publications by Klameth and Vogel [14, 186]. Here, the focus lies on data for pores with a radius of 15 Å radius, complemented by some data for a radius of 25 Å. To systematically investigate the dependence of the properties of confined water on the hydroaffinity of the confining matrix, the charges of the oxygen and hydrogen atoms of the pinned water molecules were varied in some of our studies, ensuring that charge neutrality of these molecules is maintained.

5.2.2 Results

Comparison of Bulk Behavior for the Used Simulation Packages

In order to assess the effect of using two different simulation packages, we first compare static and dynamic properties of SPC/E bulk water in the temperature range from 200 K to 270 K, as obtained from NAMD and GROMACS runs, respectively.

The density shows very good agreement between both simulation packages, with the density maximum around 250 K and deviations less than 0.75%. The tetrahedral entropy shows very good agreement as well, with a difference below 2.0%.

Dynamic properties, such as the correlation time obtained from the incoherent intermediate scattering function, show a difference of up to 14% at the lower temperature values. Since correlation times are very long and plotted logarithmically, this is still a small effect in the plots, and it is due to slightly different densities used in the two bulk simulations.

Structural Properties of Confined Water

Density profile and molecular orientation

Fig. 16 shows the oxygen density profile as a function of the distance from the pore axis. In order to obtain actual densities, each oxygen atom is assigned the mass of a water molecule. Note that the center of the pore is at the center of the figure.

Due to the rotational symmetry of the potential, the smooth pores cause pronounced density oscillations, which extend up to the pore center. The density in the pore center is approximately the same in the atomistic and smooth silica pores. Due to the roughness of the walls, the density cutoff is smeared out for the atomistic walls, and some water molecules even enter the silica matrix. The precise peak positions and heights for a given pore type depend on water density and pore radius, and, thus, have no deeper

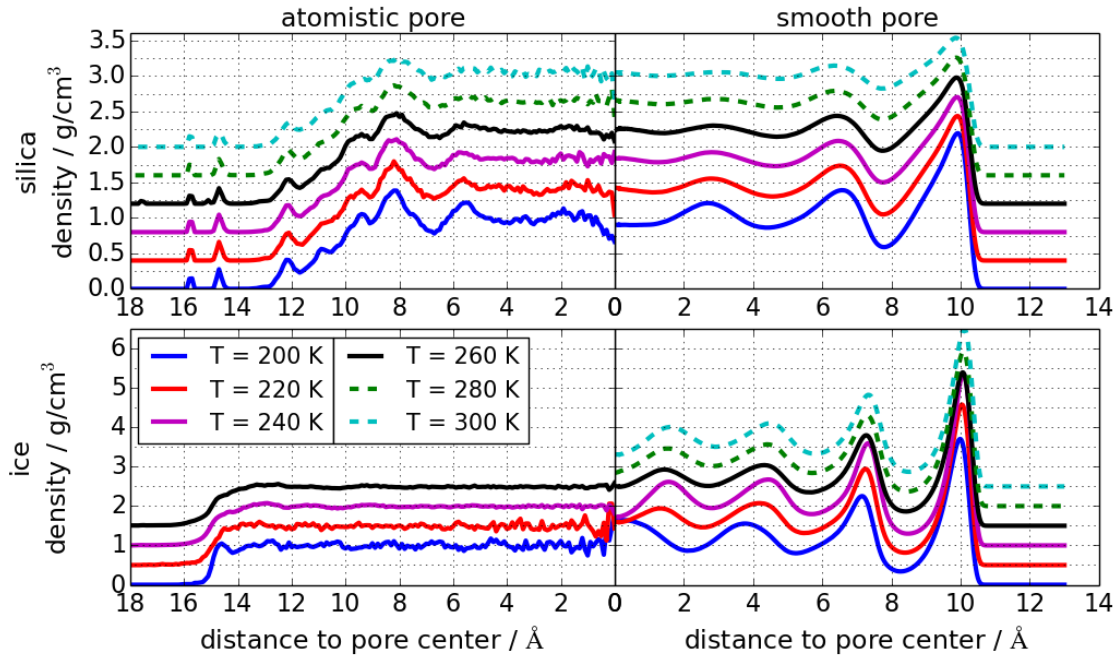

Figure 16: Density profiles based on the positions of the oxygen atoms. For clarity, curves for different temperatures are vertically shifted. In contrast to the other figures, the distance to the pore center is plotted on the horizontal axis.

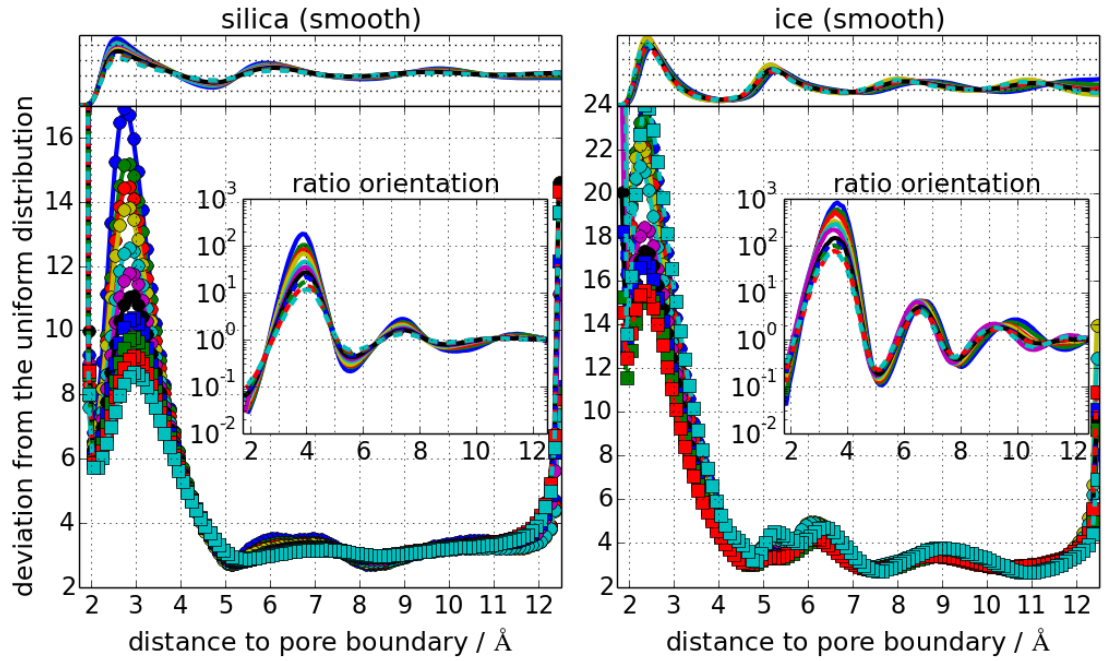

Figure 17: Water structure in smooth pores: (top panels) density profile, (main panels) deviation from the uniform angular distribution, and (insets) number of molecules pointing towards pore center divided by number of molecules pointing towards pore boundary, each within $30°$ of the radial vector. The distance to the pore boundary, rather than to the pore center is plotted on the horizontal axes. Results for silica-like and ice-like pores are shown on the left hand and right hand sides, respectively.

meaning. In contrast to the other pores, hardly any density oscillations are observed in the amorphous ice pores, indicating an unperturbed water structure [14].

For both smooth pores, the strong density oscillation is accompanied by an oscillation in the orientation of the water molecules with respect to the pore surface, see fig. 17.

The hydrogen atoms of the water molecules closest to the smooth walls tend to point towards the pore surface. Since the smooth wall potentials do not interact with hydrogen atoms, these "dangling bonds" are due to entropic effects, and they are typical of hydrophobic walls [171, 38, 175, 40]. Indeed, the well depths of the LJ potentials fall into the hydrophobic regime.

The water molecules within the first water layer tend to lie parallel to the pore surface, i.e., both O–H vectors are perpendicular to the radial direction, with a preference to orient themselves parallel to the symmetry axis. This produces the pronounced deviation from the uniform angular distribution at such distances to the pore boundary. At the inner flank of the first density peak, hydrogen atoms tend to point towards the pore center. This pattern of hydrogen atoms pointing in the direction of decreasing density is repeated in the other density peaks, albeit to a smaller degree.

The number of hydrogen bonds per water molecule turns out to be larger near the density minima than near the density maxima, where the number of hydrogen bonds is, however, still larger than in bulk water at the corresponding density. Similar conclusions were drawn based on NMR shifts calculated in ab-initio simulations of water in silica pores [10].

We considered two water molecules as hydrogen bonded when the angle between the intramolecular O–H vector and the intermolecular O...O vector was less than 30°, provided that the O...O separation was less than 3.35 Å [92].

The formation of density oscillations is also well known from systems with flat confining surfaces. For interfacial water at flat homogeneously hydroxylated silica surfaces [170, 187] the formation of the first water layer is accompanied by a clear molecular orientation. Similarly, Bonnaud et al. [188], studying SPC water confined in amorphous silica slit pores, found a large peak in the angular distribution in the first adsorbed water layer. The cylindrical shape of our pores leads to a less pronounced molecular orientation, similarly to the case of a partially hydroxylated silica surface with a heterogeneous distribution of hydroxyl groups [187].

Tetrahedral Entropy

Fig. 18 shows the tetrahedral entropy $S_Q(T) - S_0(T)$ in units of k_B as a function of the distance to the pore boundary. A value for S_0 can be determined when extending the Adam-Gibbs relation between translational relaxation time and configurational entropy to the tetrahedral relaxation time and tetrahedral entropy at high temperatures [64]. We found a value of $S_0 \approx 3.97 k_B$, which is not far from the value $S_0 \approx 4.21 k_B$ found by Kumar et al. [64] for the TIP5P water model. While the tetrahedral ordering of the bulk is preserved in the amorphous ice pore, it is strongly distorted in the other pores. In the former pore, the small peak at the boundary is the mere consequence of the fixed positions of the wall atoms. In the other pores, in particular, in the smooth pores, we find a strong increase of the tetrahedral entropy when approaching the pore boundary, which reflects the strong deviation from the bulk structure observed in the above analysis of water orientations. Even in the center of these pores, water shows a larger tetrahedral entropy than in the bulk. Not surprisingly, this effect is stronger at lower temperatures. The full probability distribution $P(q_i)$ of the tetrahedral order parameter (not shown) in the center of the smooth ice-like pore shows features which indicate reduced order and resembles that of bulk water at considerably higher temperatures or densities. The strong density oscillations in the inner region of the smooth ice-like pore have only a minor effect on $P(q_i)$.

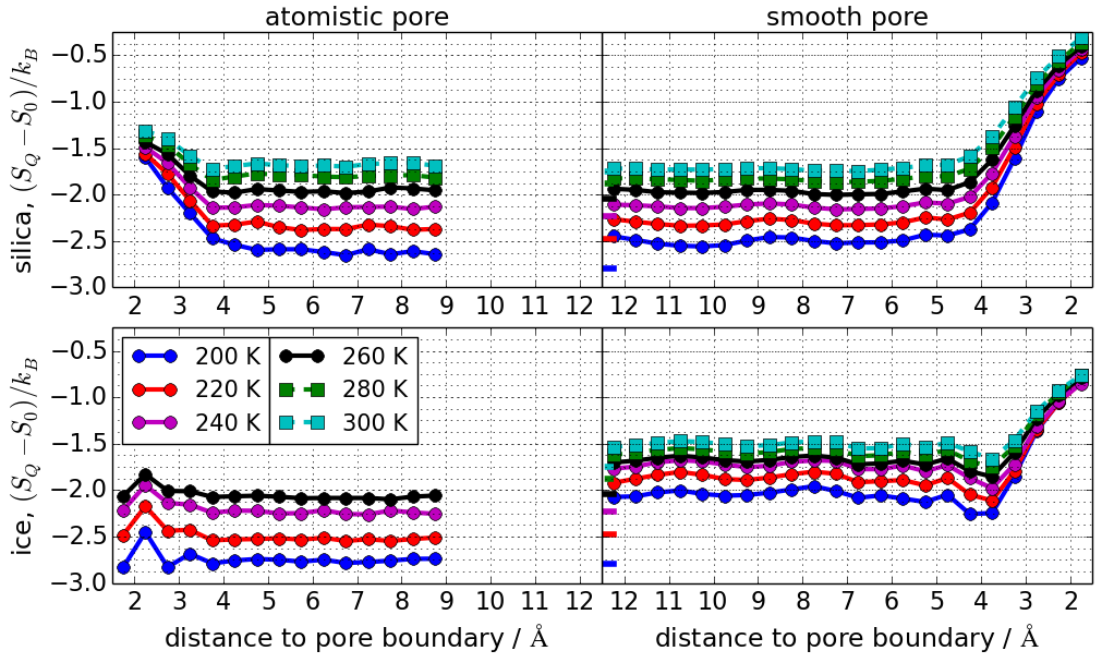

Figure 18: Tetrahedral entropy $(S_Q(T) - S_0(T))/k_B$ vs. distance to the pore boundary. The short thick lines denote the bulk values at 1 bar.

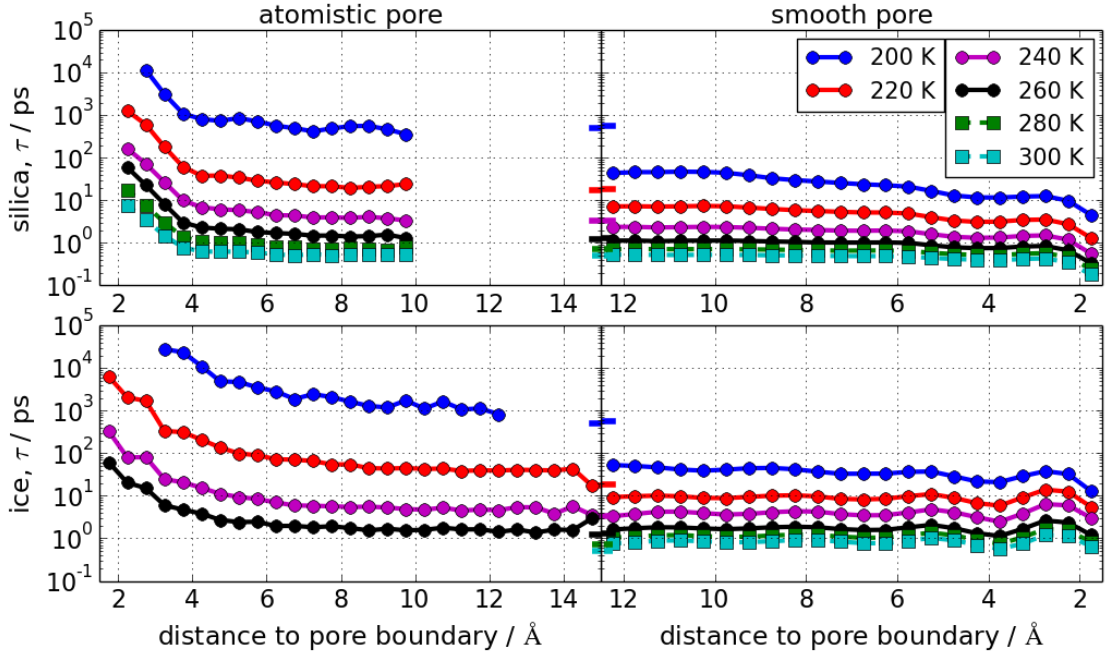

Figure 19: Correlation times of the incoherent intermediate scattering function $F_q(t)$ as a function of the distance to the pore boundary.

Intermediate Scattering Function

Fig. 19 shows the correlation times τ of the incoherent intermediate scattering function evaluated as a function of the distance to the pore boundary.

The most striking feature of these plots is that dynamics slow down drastically towards the pore boundary in the atomistic pores, but accelerate in the smooth pores. At low temperatures, dynamics is considerably faster than in the bulk for the smooth pores even in the pore center. We made sure that this acceleration of the dynamics is not an artifact of the numerical implementation by varying the size of the simulation box and the algorithm for the electrostatics, which gave similar results.

In order to understand better why the correlation time strongly increases near the atomistic walls, while it slightly decreases near the smooth walls, we studied a situation that is intermediate between the two pore types. Apart from the wall roughness, the two pore types differ also by the electric dipole moments present in the atomistic walls, but not in the smooth walls, which are defined only by a LJ potential. By reducing the charges of the oxygen and hydrogen atoms in the wall of an amorphous ice pore, one can interpolate between the two situations. Since this charge reduction reduces the strength of the interaction between the pore and the water molecules, the pore becomes more hydrophobic.

Fig. 20 shows the position-resolved correlation times τ for a pore of 25 Å radius, formed by pinned water molecules with variable charges of the oxygen and hydrogen atoms at a temperature of 240 K. The charge on the oxygen atoms was varied between $-0.3e$ and $-1.0e$, with a charge of $-0.8476e$ for SPC/E water. The charge of the hydrogen atoms was altered accordingly so as to preserve the charge neutrality of the water molecules. For comparison, we also show the position-resolved correlation times for the amorphous ice pore with a radius of 15 Å at 240 K.

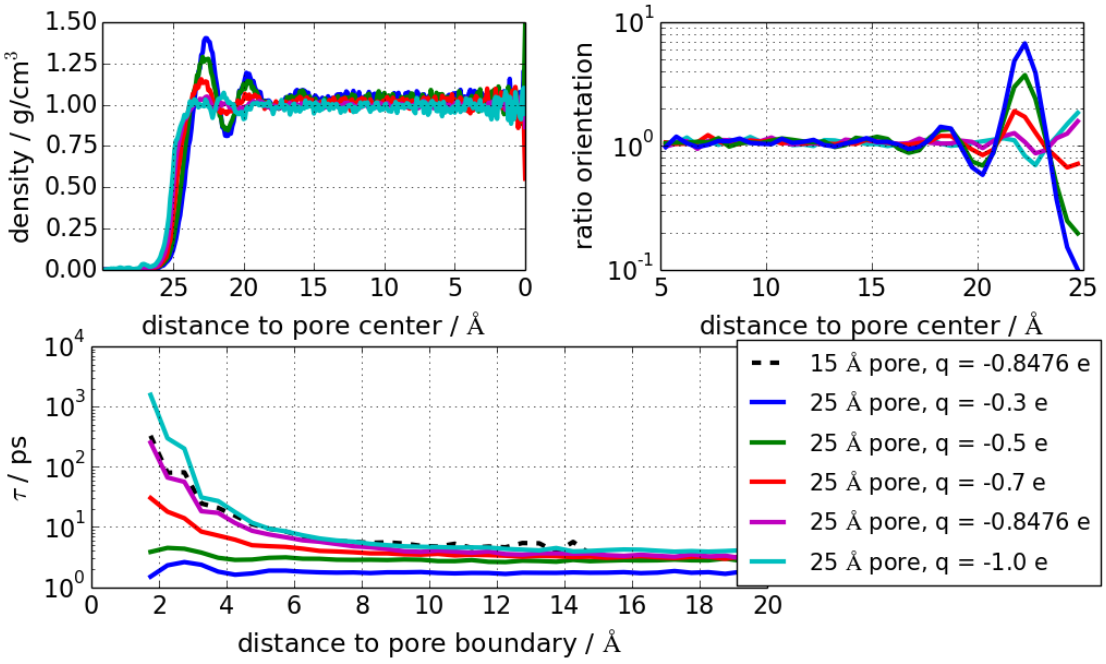

Figure 20: Density, molecular orientation, and correlation time obtained from the intermediate scattering function $F_q(t)$ at 240 K, in dependence on the distance to the pore boundary for an amorphous ice pore with 25 Å radius, where the charges of the pore atoms were modified to the given values q for oxygen and $-q/2$ for hydrogen.

As can be seen, the correlation time at the wall decreases by three orders of magnitude when the absolute value of the charges of the wall atoms is decreased. Even at the pore center the correlation time is reduced, despite the larger diameter of the pore. At the same time, oscillations in density and molecular orientation become significant when reducing the absolute value of the charges, i.e., with increasing hydrophobicity of the wall. The reduced correlation time in the pore center is accompanied by a higher disorder in the water structure. To investigate the relation between dynamics and structure in more detail, fig. 21 shows the inverse of the (dimensionless, reduced) correlation time

$$\frac{1}{\tau^*} = \frac{1}{\tau} \frac{1}{\sqrt{k_B T/M}\,\sqrt[3]{\rho/M}} \tag{59}$$

plotted against the tetrahedral entropy. Here, ρ is taken as the average value in the pore center, and M denotes the molar mass. In addition to the data for the different pores, we show also the values for the two bulk isochors at 0.9 g/cm^3 and 1.1 g/cm^3, and for the 1 bar isobar.

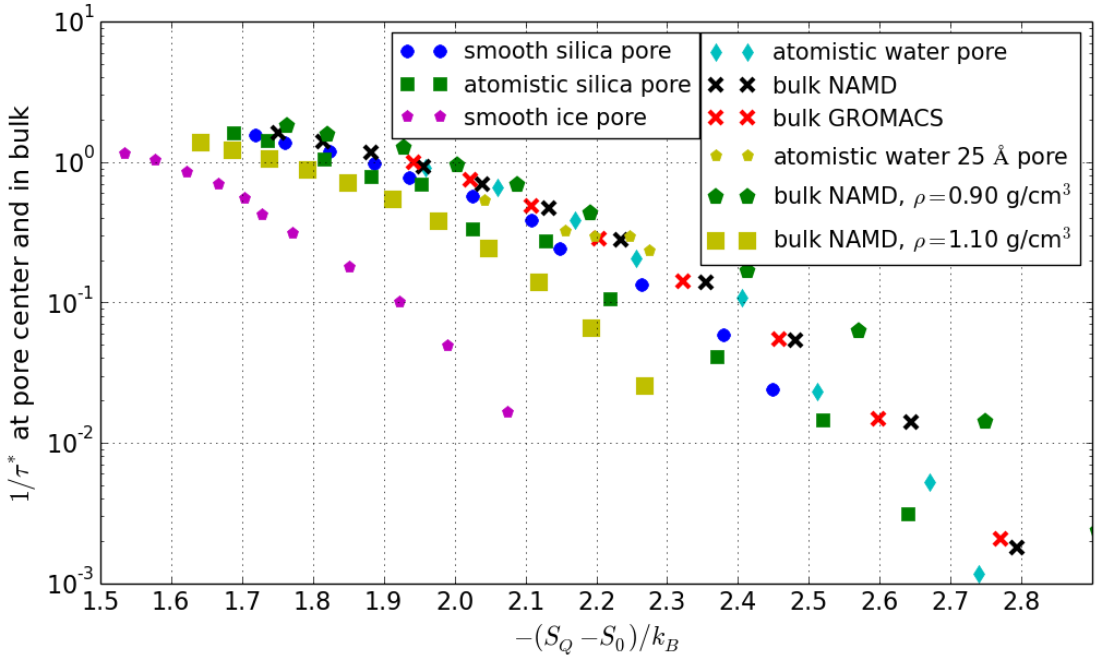

Figure 21: $1/\tau^*$ (inverse reduced correlation times) vs. $-(S_Q - S_0)/k_B$ in the bulk and in the center of the studied pores.

Apart from the smooth ice-like pore, the data for all pores lie between that for the two isochors and follow the same trend, indicating that the degree of disorder is a determining factor for the correlation time. This result is in agreement with a study by Nayar et al. [189], who found a correlation between tetrahedral order and local bonding energy for water molecules. With decreasing temperature, i.e., with increasing $-(S_Q - S_0)$, the difference between the different pores increases.

Fig. 22 shows an Arrhenius plot of the correlation time τ of the intermediate scattering function at the pore center and the pore boundary for water in all studied pores and in the bulk liquid, along with fits to the VFT-relation (cf. eq. (28) in 4.1) and simply (exponential) Arrhenius-like behavior.
It is evident that the temperature dependence of the correlation times is smaller for water in the center of the smooth pores than in the center of the atomistic pores, at least in the studied temperature range. Furthermore we observe a change from VFT-like behavior to Arrhenius-like behavior when going from the pore center to the pore boundary for both atomistic and smooth pores.

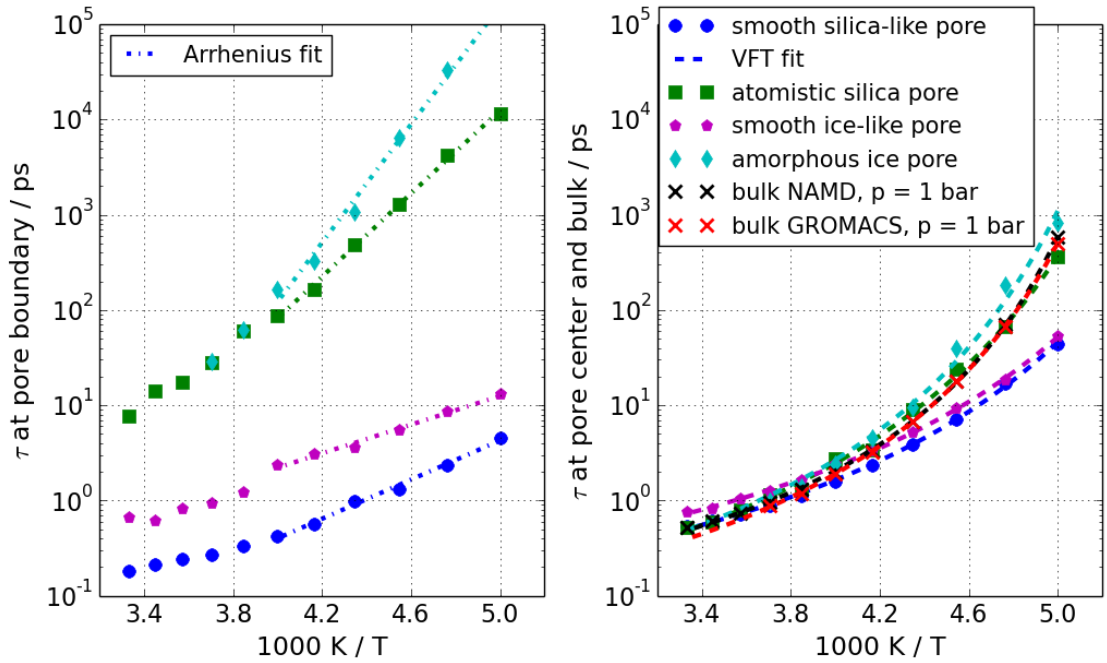

Figure 22: Arrhenius plot of the correlation times of water in the studied pores and in the bulk liquid. The left hand figure shows the correlation time at the pore wall with an Arrhenius fit for temperatures below and including 250 K, the left hand figure shows the correlation time at the pore center (and bulk) with fits according to the VFT-relation, cf. eq. (28).

Fig. 23 shows the tetrahedral entropy as well as the second, third and fourth moment vs. the first moment of the tetrahedral order distribution (the tetrahedral order parameter) for a number of different densities (0.9 g/cm^3 - 1.15 g/cm^3) and temperatures (200 K - 300 K). While not topical w.r.t. confined fluids, it is interesting to note not only the strong correlation between the tetrahedral entropy and the tetrahedral order parameter, but also the strong correlation with the following moments of the tetrahedral distribution.

This indicates that the better part of the information w.r.t. to tetrahedral order is already contained in the tetrahedral order parameter, and that changes in the water network caused by variation of parameters like density or temperature are only weakly dependent on the specific parameter or combination thereof.

5.2.3 Discussion

In this subsection, we will discuss and interpret our results for the correlation times and their relation to density and entropy in the light of what is known about water dynamics.

The relation between dynamics and entropy was evaluated for bulk water by several groups.

Scala et al. [190] reported for SPC/E water that the diffusive dynamics is governed by the configurational entropy. Mittal et al. [150] showed that the anomalous density-dependent trends in diffusivity for SPC/E water are directly reflected in the two-body, translational correlation contribution to the excess entropy, similar to their earlier work involving a core-softened fluid showing similar anomalies as the SPC/E water model [138]. Errington et al. [146] and Agarwal et al. [147] investigated the dependence of the dynamical properties of SPC/E water on entropy. They observed that the reduced diffusivity shows a strong correlation with the excess entropy for higher temperatures, but for lower temperatures the curves belonging to different densities do not collapse. This is even more so when the excess entropy S_{ex} is re-

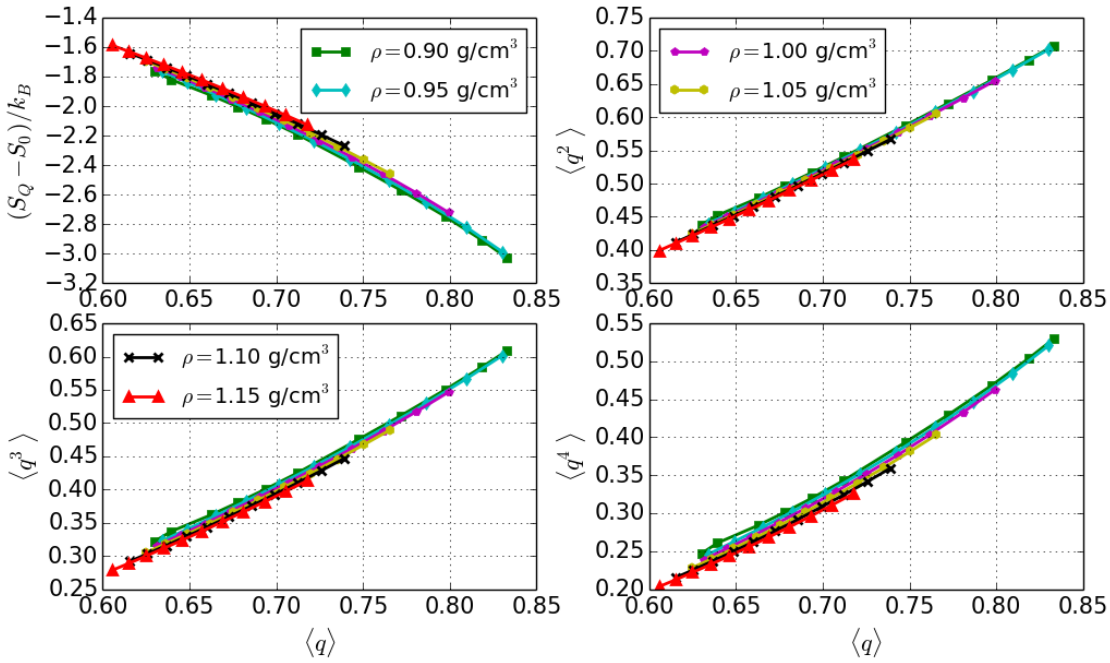

Figure 23: Tetrahedral entropy, second, third and fourth moment of the tetrahedral order vs. the tetrahedral order parameter for different density (cf. legend) and temperature values (200 K - 300 K) in the bulk. The strong correlation between first and consecutive moments of the order distribution is apparent.

placed with the pair correlation entropy S_2. Similar results hold for the reduced correlation times [146]. To the best of our knowledge, there are no publications comparing the tetrahedral entropy with the excess entropy for water models. However, Kumar, Buldyrev, and Stanley [64] showed that the tetrahedral entropy for the TIP5P water depends linearly on S_2 for lower temperatures, with an increasing slope for higher temperatures.

Agarwal et al. [148] and Prasad et al. [149] explored scaling relationships between transport properties in water and excess entropy. Prasad et al. [149] modified the relative strength of the Lennard-Jones and electrostatic interaction and found that Rosenfeld-scaling need not break down progressively as the degree of energy-virial correlations decreases. Agarwal et al. [148] show that Rosenfeld-scaling is approximately valid for TIP4P/2005, and that the magnitude of the tetrahedral entropy for the low density, low temperature isochores is comparable with that of the pair correlation entropy S_2. In this structurally anomalous regime, the excess entropy S_{ex} and S_2 are therefore strongly correlated with tetrahedral order. Kumar, Buldyrev, and Stanley [64] showed that for TIP5P water the tetrahedral entropy depends linearly on S_2 for lower temperatures, with an increasing slope for higher temperatures.

Our results (cf. fig. 21) for the relation between tetrahedral entropy and correlation time at the pore center are consistent with the cited bulk results, showing a strong correlation between the two quantities at higher temperatures and a somewhat weaker correlation at lower temperatures. Only the smooth ice-like pore behaves differently. This cannot be due solely to the different density value at the pore center, since these values also differ between the other pore systems, although not to the same extent. We suggest that the different behavior of the water in the smooth ice-like pore is the consequence of the pronounced formation of density layers, which extend to the pore center and which are accompanied by a large deviation of the water orientation from the bulk behavior. This different ordering of the

water molecules is not well captured by the tetrahedral order parameter, therefore the tetrahedral order parameter is smaller than in the other pores for the same value of the correlation time.

Although the rough and smooth pores show a very different dynamic behavior when approaching the pore boundary, in both cases we have observed a changeover from a VFT-like temperature dependence to changes in temperature to a more Arrhenius-like behavior for lower temperatures (cf. fig. 22). For the rough pores, where the behavior at the pore walls is strongly influenced by the (unchanging) energy landscape this drastic change in fragility is to be expected [14]. For the smooth pores the walls do not impose a complex energy landscape, but apparently determine nevertheless the structure of the water close to it and thus the energy barriers that must be overcome. Mamontov et al. [191], who investigated the behavior of water dynamics on the (110) surface of rutil (TiO_2) nanopowder by experiment and molecular dynamics simulations, identified three different components (slow, fast, and very fast) that could be related with different dynamic behavior. The slow component showing non-Arrhenius behavior was causally linked to a highly localized layer, which does not appear in our systems. The Arrhenius-like behavior of the very fast components could be related to a relatively low number of hydrogen bonds [192], and the authors suggested that in order to have a dynamic crossover from the low-temperature Arrhenius to the high-temperature non-Arrhenius behavior, the hydration level of the surface should be sufficiently high for a large fraction of water molecules to experience a bulk-like environment with a saturated number of hydrogen bonds to the nearest neighbor water molecules. This suggestion was experimentally corroborated by Mamontov et al. [193].

Water dynamics near the pore boundary is much slower for the atomically rough pores than for the completely smooth pores. In the literature slower water dynamics were mostly observed at hydrophilic compared to hydrophobic walls [194, 38, 170, 195]. Moreover, hard sphere liquids were found to show slower dynamics near walls with a higher degree of roughness [196] and simple liquids were found to move slower at non-attractive rough walls than at non-attractive smooth walls [16]. We have seen the same thing w.r.t. the hydrophobic and hydrophilic walls in the last section.

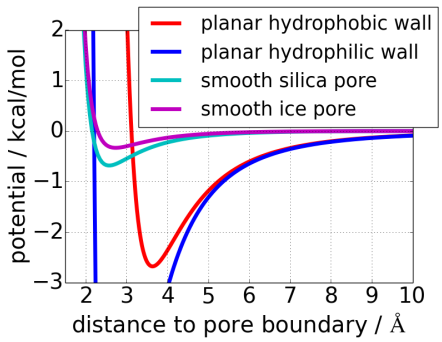

Figure 24: Potential acting on a single oxygen atom for planar and cylindrical smooth confinement.

In contrast to this Papavassiliou et al. [180] have used MD simulations to investigate slip vs. no-slip conditions and found slippage at hydrophilic interfaces as well, which has been experimentally underpinned by the work of Lee et al. [197]. To discriminate for atomistic walls between roughness and hydroaffinity effects, we varied the polarity of the pinned water molecules forming an amorphous ice pore, while leaving the surface topology unchanged. We observed that the slowdown of water vanishes when the polarity is reduced and, hence, it is not a geometrical effect, e.g., an excluded-volume effect. Rather, the slowdown results from the wall atoms imposing a static energy landscape. E.g., they provide fixed preferred sites for the formation of hydrogen bonds, to which the neighboring liquid needs to be adapted, blocking channels for cooperative structural rearrangements [198]. Papavassiliou et al. [180] have observed a similar effect, when reducing the electrostatic interaction between MgO and SPC/E water, resulting in slippage at the interface. They also report the formation of ”density bridges” in which the water molecules rearrange themselves as opposed to switching layers.

Water dynamics near smooth walls can even be faster than in the bulk liquid, consistent with results by Lee and Rossky [98] for water near hydrophobic walls. In the last section we predicted this to occur for sufficiently smooth interfaces, given a sufficiently weak interaction potential. In the smooth pores there

is no pendant to the electrostatic interaction between water and pore boundary. The resulting potentials are more hydrophobic than what we termed "hydrophobic walls" in the last section, as can be seen in fig. 24. A breakdown of the translational dynamics with concern to movement along the pore axis and perpendicular to it shows roughly the same picture as seen in fig. 19, with movement along the pore axis showing slightly less oscillation of the correlation times and in-plane movement showing slightly more, this simply being caused by the radial density peaks.
These faster dynamics at smooth surfaces permeate the entire pore. While both the rough silica pore and the amorphous ice pore approximately reach bulk values of the correlation time at the pore center, this is not the case for either of the smooth pores. Again, this effect is not due solely to the wall roughness, as can be inferred from our finding that a decrease of the dipole strength of the pinned water molecules leads to faster dynamics at the pore boundary, with the correlation time eventually falling below the bulk value.

A decrease of the dipole strength leads to weaker hydrogen bonds between the confined liquid and the confining matrix, implying an increase in hydrophobicity of the confinement. The resulting distortions of water structure are felt across the whole pore.

We tested whether faster-than-bulk dynamics in the pore center can be due to the changed density. For this purpose, we evaluated the change of correlation time in the bulk with density, finding a less than 30% reduction in the correlation time when density was increased by 10% at the relevant temperature and density values. In contrast, in the amorphous ice pore with charges reduced to $q = -0.3$ a density change of less than 5% in the pore center is accompanied by an almost 50% reduction in correlation time. This means that the change in tetrahedral entropy, which in turn is strongly correlated with correlation time, is only partly due to a change in density, and mainly due to the influence of the pore wall on the water structure in the pore. Indeed, the oscillations in density and molecular orientation shown in figs. 16 and 20 confirm that the pore boundary strongly disturbs the structure of the adjacent water layers, and that this disturbance permeates the entire volume of the studied pores, including the pore center.

5.2.4 Conclusion

We compared the structure and dynamics of SPC/E water in atomically rough and completely smooth pores. Moreover, we varied the hydroaffinity of a rough confinement by changing the dipole moments of the molecules forming the pore matrix, while keeping the wall topology unchanged.

We observed a difference in dynamics at the boundaries. Near rough walls comprised of charged atoms, there is a strong slowdown of water dynamics since structural relaxation is hindered by an atomically rough and essentially static energy landscape imposed by the largely fixed wall atoms. Accordingly, the slowdown vanishes when the dipole moments of the wall atoms are reduced and, hence, the fluctuations of the potential energy along the wall surface are diminished. Likewise, the speedup of water dynamics near smooth or uncharged walls can be explained by the absence of an inherent set of anchor-points for hydrogen bonds in the pore matrix. Furthermore, the absence of orientating contributions by the wall potential allows entropic orientational effects to dominate, eliciting structural oscillations. At the pore boundary this results in a disturbed hydrogen bond network of water, encouraging faster dynamics and Arrhenius-like behavior for higher temperatures. Farther in the pore these oscillations still distort the tetrahedral order, shifting both tetrahedral entropy and structural relaxation from the bulk behavior.

We could demonstrate that despite these differences in the dynamic behavior dynamics at the wall display increasingly Arrhenius-like behavior for both rough and smooth pore types.

We showed that, in the case of weak structural changes, the tetrahedral entropy, which is easily accessible in confined geometries, is a good indicator for the change in dynamics and, depending on the

temperature range, weakly to strongly correlates with the correlation time of the incoherent intermediate scattering function. It is interesting to note that the cylindrical geometry of the confinement is essential for observing effects of the wall on water structure and dynamics even at a distance of 25 Å. For flat geometries, e.g., slit pores, the influence of the wall ranges only up to a distance of 15 Å, as shown by simulations with different water models and wall types [170, 171, 38, 172, 173, 12] as well as experiments [174].

The finding that the hydroaffinity and structure of the wall have a strong effect on the structure and dynamics of water is very relevant for water in biological cells, which is always close to surfaces of different hydroaffinity, for instance to proteins with patchy hydrophobic surfaces.

5.3 Isobutyric acid and water mixture

This part of the thesis is devoted to the investigation of a mixture of water and isobutyric acid (iBA), confined in a cylindrical nanopore. Both an atomistic (silica) pore of roughly 4.2 nm diameter, as well as a smooth pore based on the average potential of the former are used. Pure confined iBA and water are simulated as well, but the focus lies on the mixtures. Weight percentages of 0, 40, 50, 60, 70 and 100 are simulated, where specification of the mixture ratio always reflects the iBA content, i.e. a 40wt% mixture will consist of 40% iBA and 60% water w.r.t. to weight. Bulk simulations were done as well, however, they were mostly used to bracket the temperature of demixing. Temperature values between 300 K and 400 K are used for the simulations.

The general behavior is only weakly dependent on the mixture ratio and contrary to expectations we find that in the atomistic pore our model results in wetting of the iBA, with a small amount of water at the pore wall, and a broad distribution of dynamic correlation times. Interestingly the distribution of correlation times of the iBA is not completely monotonic w.r.t. translational motion, but rather shows a slight speed up of dynamics directly at the pore boundary, a facet of behavior not seen for pure confined iBA. When observing the susceptibility w.r.t. translational and orientational movement we find different dynamic regimes for both dynamics. The mixture in the smooth pore also prefers iBA at the pore boundary, molecular orientation and dynamics are very different, however.

Our investigation of the mixture was inspired by Professor Buntkowsky from the TU Darmstadt, who had done corresponding experimental investigations before [199]. Vyalikh et al. [199] used ^{1}H NMR relaxometry and ^{1}H-pulsed field gradient diffusion measurements to investigate a 54wt% iBA and D_2O mixture confined in a controlled pore glass of roughly 10.3 nm diameter. They found two main dynamic processes w.r.t. to both translational and rotational motion and developed a qualitative model of the phase separation process in the pores, which assumes a temperature-dependent domain-like structure of the liquid below the phase transition temperature and a breakdown of these domains upon reaching the transition temperature, with the pore boundary wetted by water.

In this section results pertaining to a directional evaluation of the incoherent intermediate scattering function (3.4) are shown. Deviations from the targeted absolute value of the scattering vector $q = 2.27\,\text{Å}^-1$ are generally less than 1.07%, for water, for iBA, the deviation is generally less than 2.56%.

5.3.1 Simulation methods

The MD simulations were carried out using the NAMD [65] simulation package. Water is represented by the TIP3P water model, which is part of the CHARMM [200] package, while the iBA was built using the VMD [201] PSF Generation Plugin using ideal coordinates for the iBA taken from HIC-UP [202, 203, 204] and parameters taken from the CHARMM22 [205] force field. A basic blueprint of the molecule was compiled by combining elements of residues LEU and GLUP. In order to ensure charge neutrality the partial charge on the connecting atom was slightly increased, cf. table 6 for a visual representation and partial charges.

The silica nanopore has a diameter of roughly 4.2 nm and a density of roughly 7 silanol groups per nm^2. The manufacturing process of the pore was conducted analogously to the procedure described by Rovere et al. [206]. A more detailed explanation concerning this particular pore can be found in the master thesis by Alexander Janz [207], in section ”Die Implementierung der Pore mit einer Silanoldichte von ca. 7 OH-Bindungen/nm^2”, from page 26 onward. For the Lennard Jones (LJ) interaction parameters and partial charges for the silica pore we used the values as given by Bródka and Zerda [181]. All pore atoms except for the hydrogens were kept at fixed positions, all hydrogen bonds were kept at constant length, and in the pore hydrogen positions were further restricted by the harmonic part of the angle

potentials as given by Hill and Sauer [208]. Interactions between the various species were governed by the Lorentz-Berthelot mixing rules.

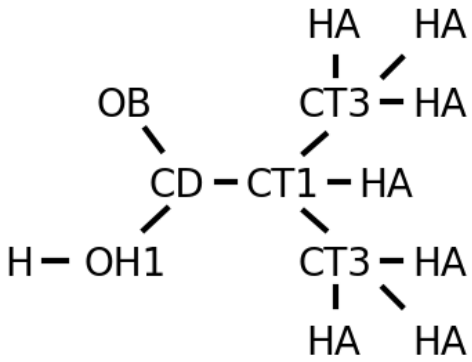

Figure 25: Visual representation of the potential interaction points of the iBA molecule as represented in NAMD. Parameters are given in table 6.

atom type	CT1	CT3	CD	OB
charge q	-0.12	-0.27	0.75	-0.55
ϵ (LJ)	0.02	0.08	0.07	0.12
r_{min} (LJ)	4.55	4.12	4.0	3.4
atom type	OH1	HA	H	
charge q	-0.61	0.09	0.44	
ϵ (LJ)	0.1521	0.022	0.046	
r_{min} (LJ)	3.54	2.64	0.449	

Table 6: Simulation parameters of the iBA. Charges are given in units of the elementary charge. LJ parameters according to NAMD conventions.

Since constant pressure simulations cannot be done using the pore we first determined an averaged potential for all atom types of the mixture. NAMD enables the implementation of external potentials and NPT simulations with constant cross sections of the unit cell. These features were used to identify the density at the pore center corresponding to temperature at a pressure of 1 bar. We then did a number of simulations at temperatures of 300 K, 350 K and 400 K to establish the ratio of molecules in the rough pore with the correct density at the pore center and the smooth pore within a comparable volume element. By linearly interpolating along these ratios, and filling the rough pores accordingly, we were able to avoid a constant increase of pressure with rising temperature. Comparisons to the behavior in the smooth pores also allow us to assess the influence of pore roughness and hydrogen bonding with the pore wall.

In the bulk we generally used a minimal equilibration time of 10 ns, starting from a configuration with separated components. For the smooth pores the bulk configuration was taken and the confining potential slowly established. After formation of the pore we equilibrated for a further simulation time of 15 ns. In the atomically rough pores the slowdown of dynamics at the pore boundary compelled us to further monitor the weight averaged radius of iBA and water as a measure of equilibration, leading to equilibration times between 7.5 ns and 17.5 ns depending on temperature and weight percentage of the mixture.

For simulations within the atomistic pore a time step of 1 fs was utilized, simulations in the bulk or smooth pore were carried out with a time step of 2 fs. The Coulomb interactions were calculated using the Particle-Mesh Ewald sum. Periodic boundary conditions were applied. We used a cutoff at 15 Å and a switching distance of 12 Å. In the NPT ensemble pressure was kept constant using the Langevin-Piston [68] method. NVT simulations were done using the Langevin thermostat, with a coupling coefficient of 1.0 ps^{-1} and with the hydrogen atoms included in the Langevin dynamics. Temperature values were spaced out in intervals of 10 K, with simulations generally in the 300 K to 400 K region.

5.3.2 Results and discussion

Demixing in the bulk

A first test of the validity of our force field was to look at whether demixing occurs in the bulk. Due to finite size effects the temperature of demixing cannot be pinned down exactly. We observe separate regions of iBA and water at 300 K, mixed systems at 400 K and increasing mixing of molecules in between, with the estimated transition temperature somewhere in the region of 350 K to 360 K.

This means that we observe a much higher temperature of demixing than is reported in the literature for the experimental system [209, 210, 211]. Such a shift of temperature, however, is not an uncommon occurrence in MD simulations.

Properties of the confined mixture

STRUCTURAL PROPERTIES

Radial density distribution

Fig. 26 shows the density profile of water and iBA as a function of the distance from the pore center in a 60wt% iBA water mixture. The qualitative features are the same for 40wt%, 50wt% and 70wt% mixtures. We can clearly observe the tendency of the iBA to form layers at the pore wall. With increasing temperature the density peaks become smaller. At the smooth wall the first density peak is higher than at the atomic wall, but the second peak is smaller.

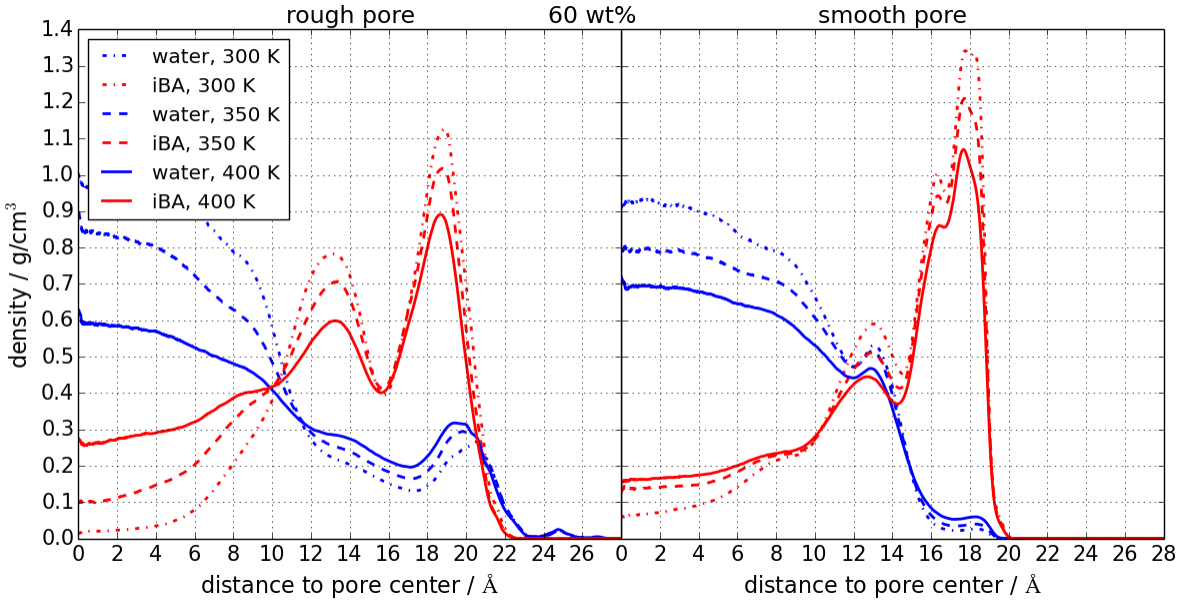

Figure 26: Density profiles for iBA and water. In contrast to the other figures in this section of the thesis, the pore boundary is on the right hand side.

Further we can observe that in the case of the rough pore there is a significant amount of water situated at the pore boundary.
Whereas in the smooth pore the density profile shows no angular dependence, close to the wall of the rough pore iBA and water form clusters more readily. Such strong differences between the influence of smooth and atomistic surfaces on molecular ordering were also seen in the case of pure confined water [166] as explained in the prior section. That the main part of the water is situated in the pore center,

rather than at the hydrophilic pore boundary is further discussed in paragraph "Accretion of iBA at the pore boundary".

Angular distribution

Fig. 27 shows the angular orientation of the iBA molecules in both pore systems for a 60wt% mixture, based on the vector between the CG and CB atoms. Vectors are considered parallel (↑↑) or antiparallel (↑↓) if they maximally deviate by 30° from ideal parallel or antiparallel orientation. ∥ indicates either of the two cases. The numbers give the ratio of the proportion of suitably orientated vectors to the proportion of the uniform distribution. For the smooth pore we defined the pore wall to be at 21.5 Å. For the rough pores, the distance to the pore is defined as the distance to the closest non-hydrogen wall atom.

In the smooth pore the atoms are ordered far more stringently than in the rough pore, at least at the pore boundary. Closest to the pore boundary the molecules show an increase in orientation parallel to the wall. The strong decline of radial orientation can be attributed to steric hindrance, the molecules cannot reach past the potential barrier to orient themselves in a radial direction. There is a slight increase in radial orientation with the carboxylic group pointing towards the pore center beforehand. This allows the water at the pore center to form a larger number of hydrogen bonds with the surrounding iBA molecules, which cannot form bonds with the smooth pore boundary.

In the case of the rough pore there is a minimal decline in molecules orientated in the $\vec{e}_z$- or $\vec{e}_\varphi$-direction. We observe a slight preference for the molecules to orient themselves radially with the carboxylic group pointing towards the pore wall. The methyl groups are preferentially not pointed towards the pore boundary when in close proximity to it. The radial orientations show a slight oscillation with a minimum of the $\vec{e}_r$ orientation and a maximum of the $\vec{e}_r$ orientation at a distance of roughly 9 Å distance from the pore wall. Increasing temperature softens the orientational preferences but does not completely eradicate them.
For both smooth and rough pores the qualitative features remain the same for all mixture ratios. When observing the structure of pure confined iBA (not shown), however, these features are generally exaggerated in comparison and oscillations of the orientation are more pronounced and reach further inside the pore. The orientation is roughly correlated with the density peaks, with the iBA molecules in the rough pore exhibiting a slight tendency to have the methyl groups pointing towards each other, or rather the carboxylic groups oriented towards pore boundary or water. This does not change for pure confined iBA, where we observe a decline of the ratio of dimers when confined in the rough pore (from 300 K to 380 K: roughly 23.4% to 22% of the molecules involved in dimers in the bulk, compared to 14.3% to 13.3% in the rough pore, where a dimer consists of two molecules where the OB and OH1 atoms (cf. table 6) of the two molecules each have a distance less or equal to 3.5 Å respectively).

DYNAMIC PROPERTIES

Incoherent intermediate scattering function

Fig. 28 shows the correlation times of the incoherent intermediate scattering function for a 70wt% mixture of iBA and water. Again the qualitative characteristics are the same for all investigated mixtures. The rough pore imposes a definite slowdown on translational motion, both for water and iBA. For the water this yields a monotonic increase with decreasing distance to the pore wall, while in the case of the iBA we can observe a slight speed-up. For pure iBA in the rough pore (cf. inlet in the uppermost left panel) the speed up is very minor compared to the mixture, and, from a distance of roughly 3.75 Å onward, seems to reach a plateau value instead. With increasing distance to the pore boundary the

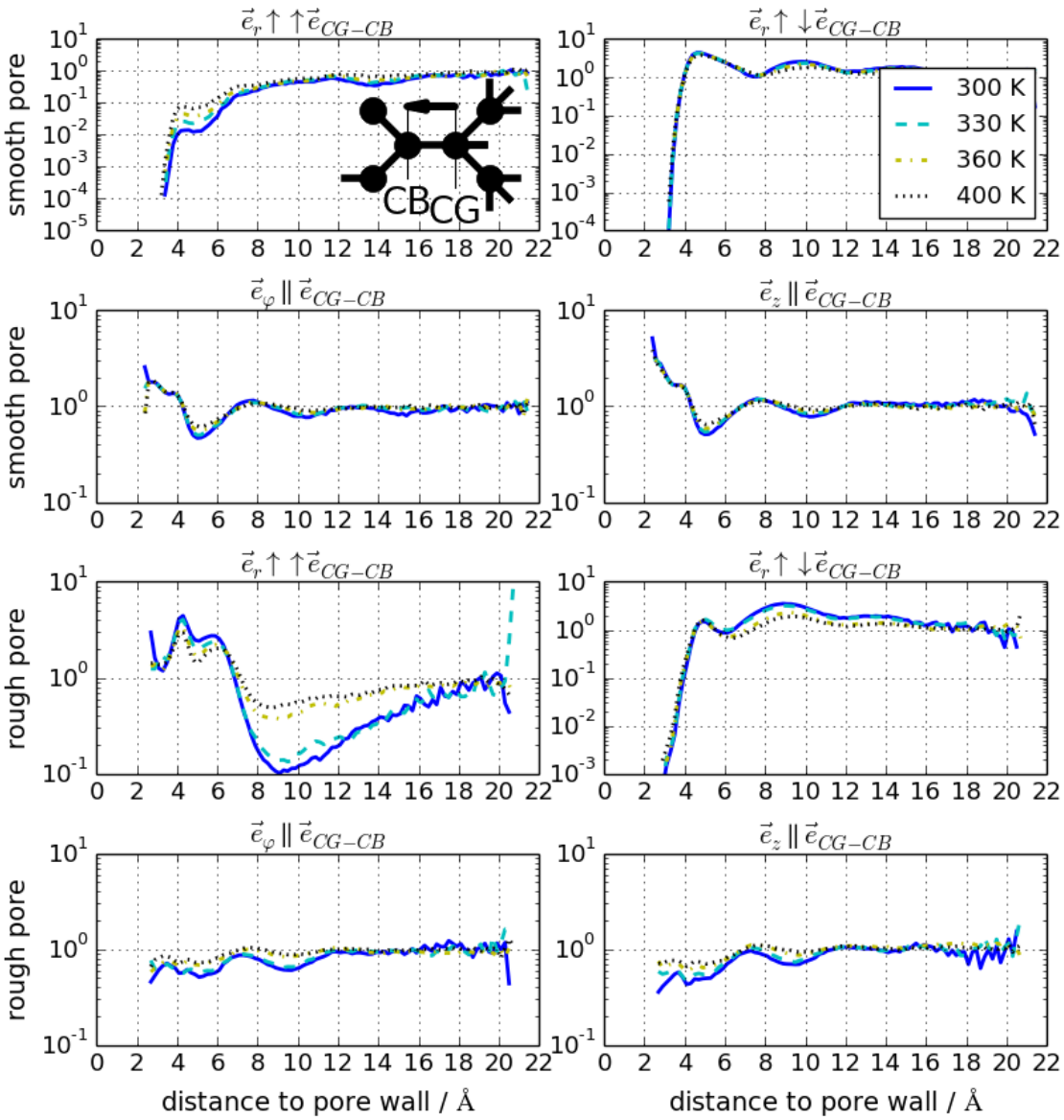

Figure 27: Angular orientation of the vector between CG and CB atoms in the iBA molecules in the rough and smooth pore. Vectors are considered parallel (↑↑) or antiparallel (↑↓) if they maximally deviate by 30° from ideal positions. || indicates that both cases are considered equally valid. The numbers give the ratio of the proportion of suitably orientated vectors to the proportion of the uniform distribution. The data shown is from a 60wt% mixture. The pore boundary is situated on the left hand side.

correlation times plateau. These values are very similar for all investigated weight percentages and only slightly lower than for the pure confined iBA (less than a ratio of 2 for all observed temperatures).

In the case of the smooth pore the pore boundary does not significantly hinder translational motion. The water molecules experience a definite speed up at the pore boundary for all temperatures, while the correlation times for the larger iBA molecules oscillate. The peaks in the correlation time correspond to the density peaks one can see in fig. 26.

We further investigated the direction dependent translational motion by evaluating the intermediate scattering function using wave vectors $\vec{q}$ in z-direction (parallel to pore axis) and the xy-plane (perpen-

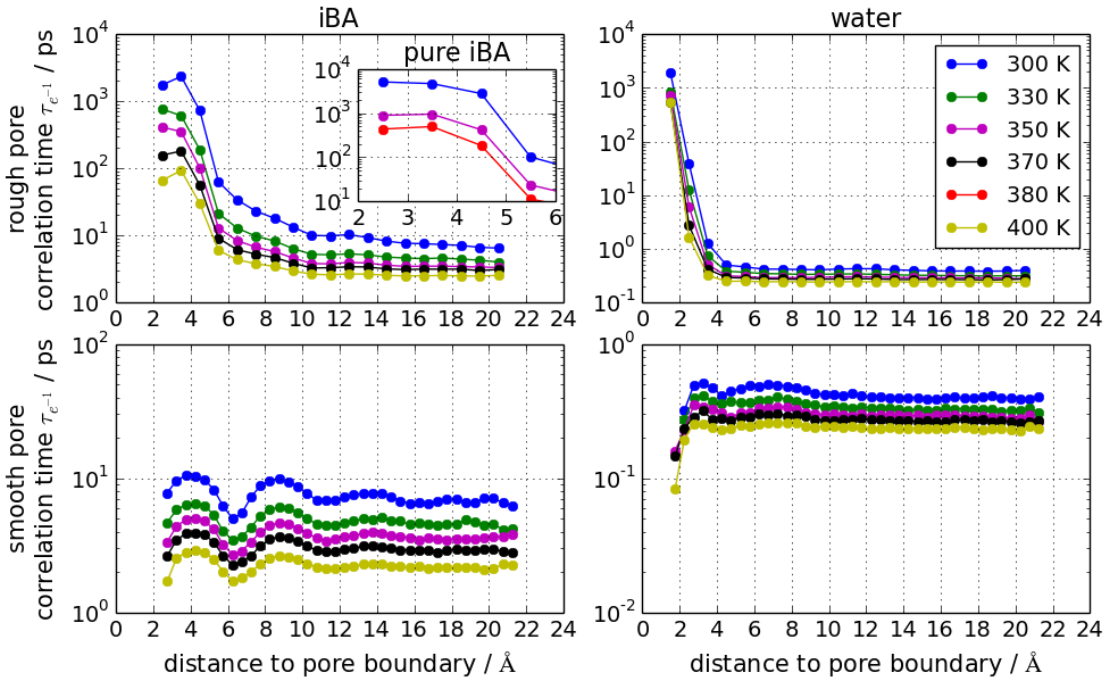

Figure 28: Correlation times of the incoherent intermediate scattering function, for iBA and water in smooth and rough pore for a 70wt% mixture of iBA and water. The uppermost left panel contains an inlet with correlation times of pure iBA confined in the rough pore. The x-axis indicates distance to the pore wall, such that the pore boundary is situated on the left hand side.

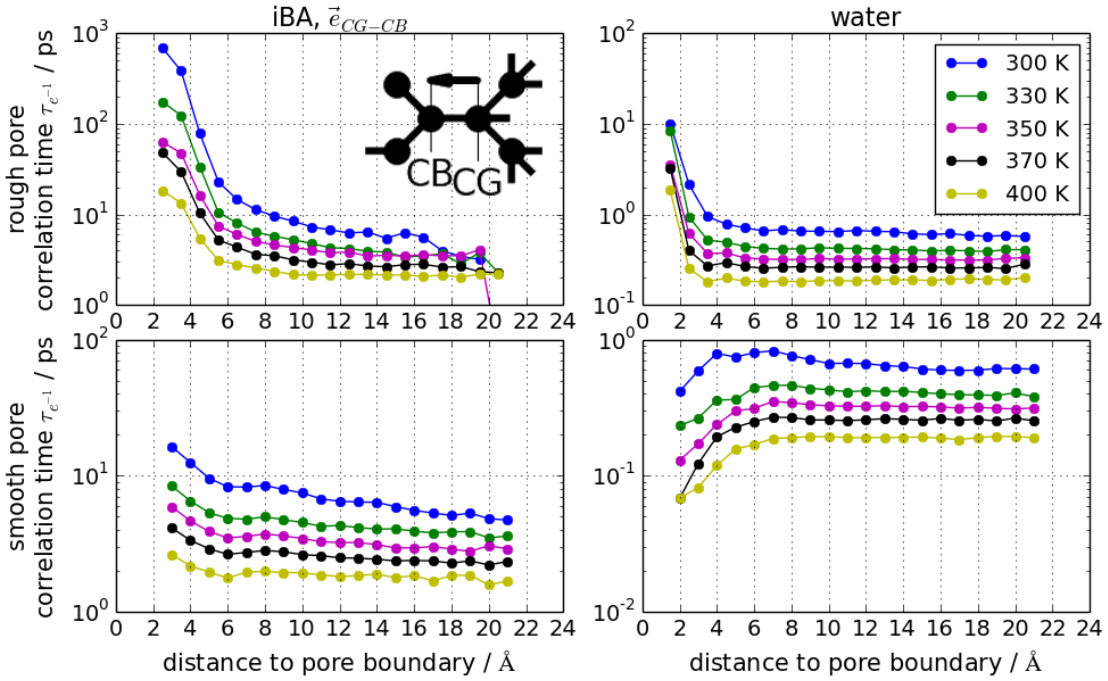

Figure 29: Correlation times of the orientational autocorrelation function, for iBA, and water in the smooth and rough pore for a 60wt% mixture. The x-axis indicates distance to the pore wall, such that the pore boundary is situated on the left hand side.

dicular to pore axis, in-plane movement). A further discrimination of the xy-plane in $\vec{e}_r$ and $\vec{e}_\varphi$ direction would have suffered from a numerical evaluation standpoint. With regard to planar walls it has been observed for water at both hydrophobic and hydrophilic walls [172, 195] as well as for hard spheres at a hard wall [179] that dynamics are faster parallel to a wall, than perpendicular.

Concerning the smooth pore, correlation times regarding movement in the z direction show little variation. In-plane movement shows slightly slower dynamics at the water/iBA interface and the speed up at the pore boundary.

The rough pore partially shows the same features. In the mixture there is a slight overtone of oscillations for in-plane movement, corresponding to the iBA density peaks. For the pure confined iBA this feature is again more pronounced and covers the whole pore. The slight speed up very close to the wall can be seen in both z-direction and the xy-plane, although again less so in the pure iBA. Generally dynamics in the z-direction in the rough pore are faster than in the xy-plane when molecules are close to the pore wall, with the factor ranging from roughly 9 for 300 K to 3 for 400 K. For water the ratio is often even higher. We attribute this difference in translational motion to the interaction the rough pore can undertake with the molecules, with the limited mobility of the hydrogen atoms of the silanol groups sufficient to disperse some of the energy of in-plane motion. In the case of the smooth pore the molecule simply overcomes a potential barrier and gains exactly the same energy when reflected back.

The slight speed up at the pore boundary is roughly correlated to the orientation of the molecule. We evaluated the intermediate scattering function binning the molecules with respect to the $\vec{e}_r$, $\vec{e}_z$ and $\vec{e}_\varphi$-orientation of the $\vec{e}_{\mathrm{CG-CB}}$ vector and in general those molecules oriented perpendicularly to the pore boundary will move slowest. Since we evaluate the intermediate scattering function with respect to the center of mass of a molecule it makes sense that closer to the pore boundary we would find a higher number of molecules oriented less perpendicularly. This explanation, however, covers both iBA molecules in a mixture and pure iBA. It is therefore insufficient to explain the slightly higher degree of the speed up seen for those iBA molecules in a mixture with water. It follows that the water molecules at the pore boundary impact positively on the translational motion of the iBA molecules. This makes sense to us, considering the volume ratio ensures that the water molecules are more mobile than the iBA.

Further, it should be noted that in the rough pore comparison of the coherent and incoherent intermediate scattering function (ISF) shows that the collective motion of iBA molecules plays an important role for lower temperatures. Correlation times of the coherent ISF are generally larger, with the ratio (correlation times of coherent ISF vs. correlation times of the incoherent ISF) decreasing with increasing temperature and initially dropping below 1.1 between 340 K and 370 K, depending on the weight percentage of the mixture.

Orientational autocorrelation function

Fig. 29 shows the correlation times of the orientational autocorrelation function for a 60wt% mixture of iBA and water. Again the qualitative characteristics are the same for all investigated mixtures. In the case of the rough pore both iBA and water continuously slow down when approaching the pore boundary. While only the rotational behavior of the $\vec{e}_{\mathrm{CG-CB}}$ vector is shown the correlation times of other reorientation vectors of the molecule show the same trend.

In the case of the smooth pore rotation speeds up slightly for the small water molecules but generally slows down for the larger and more unwieldy iBA molecules.

Similar to the case of translational motion the correlation times of the autocorrelation function traverse several orders of magnitude. In contrast, however, to translational motion there is no apparent speed up of reorientation at the pore boundary.

While the qualitative behavior (monotonic increase of correlation times), is the same for different rotational aspects of the molecule, rotational movement involving the methyl groups shows a smaller range of correlation times. This is not unexpected considering the methyl groups are only indirectly involved in the hydrogen bonding to the pore boundary. While the existence of interfacial hydrogen-bond interactions is not a prerequisite to a slowdown of the interfacial dynamics, it often amplifies this effect [212, 213, 214, 215].

Comparison to experimental findings

Vyalikh et al. [199] conducted NMR measurements on a iBA/D_2O system confined in controlled pore glass with a diameter of roughly 10.3 nm. W.r.t. self diffusion measurements they found clear deviation from isotropic single-phase diffusion, with two components visible in the data. Consequently they employed a two-phase diffusion model, which is in good agreement with the experimental data. They also investigated ^{1}H spin-lattice T_1 and ^{1}H spin-spin T_2 relaxation times as a function of temperature. The ^{1}H spin-spin relaxation T_2 shows strong deviations from mono-exponentiality at temperatures above 39°C, revealing the presence of two components with different spin-spin relaxation times. While the T_2 decay time of the slower component is temperature dependent, the fast component is nearly temperature independent with a value of ca. 1 ms.
While our MD simulations cannot perceive correlation times in that time regime we should see indications for two dynamic processes with regard to translational and rotational motion.

Fig. 30 shows translational and reorientational susceptibility in the whole pore, calculated from the incoherent intermediate scattering function and the orientational autocorrelation function. With respect to translational motion and iBA one can make out a temperature dependent main peak and a second peak or shoulder for small frequencies. For lower temperatures the simulation time is insufficient for a complete decline of the intermediate scattering function, resulting in oscillations in the Fourier transform for small frequencies. It is still evident, however, that the second peak or shoulder grows with decreasing temperature. In the case of the water we have only the one main peak, which shifts slightly with temperature.

With regards to the orientational autocorrelation function we show data concerning the $\vec{e}_{\mathrm{CG-CD}}$ and $\vec{e}_{\mathrm{CG-CB}}$ vectors (cf. inlet in the upper left panel). While the susceptibility w.r.t. $\vec{e}_{\mathrm{CG-CD}}$ shows only one, albeit drawn-out peak, we can clearly distinguish two processes for $\vec{e}_{\mathrm{CG-CB}}$, a major peak and a minor peak which devolves into a shoulder for higher temperatures. A similar division into two dynamic processes can be made for $\vec{e}_{\mathrm{OB-OH1}}$.

In both cases the distinction between the two dynamic processes can be seen on all temperature scales, albeit only weakly for higher temperatures, in contrast to the study of Vyalikh et al. [199], where the second fast rotational process only occurs from 39°C onward.

Accretion of iBA at the pore boundary

Vyalikh et al. [199] assumed in their study that the pore boundary was preferentially wetted by water. Frisken and Cannel [216] performed light scattering experiments on iBA and water in a 4 wt.% silica network with a crossover length of 300 Å. As the critical region was approached, they found that the scattered intensity initially decreased, indicating that the lower refractive index component, namely water, is preferentially adsorbed by silica.

In contrast in our simulations we see a clear accretion of iBA at the pore boundary, the density gradient of which softens with increasing temperature. To check whether this might be dependent on initial conditions we did simulations at 300 K, with the iBA completely in the pore center and completely

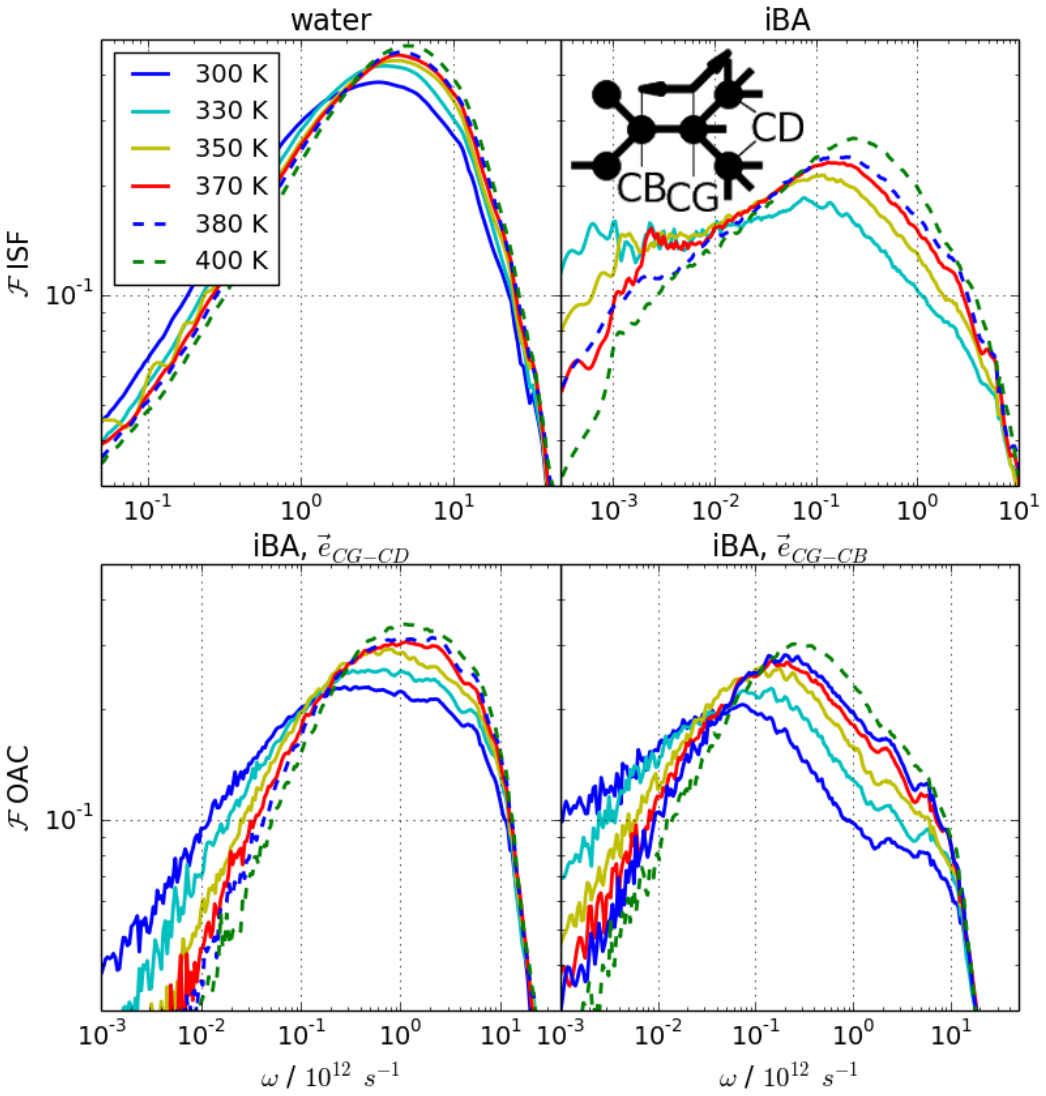

Figure 30: Susceptibility, calculated from the intermediate scattering function and orientational autocorrelation function of iBA and water in the rough pore. The orientational autocorrelation function is taken with respect to two different molecular vectors (cf. inlet in the upper left panel).

strung out along the pore boundary. Both cases devolved into the scenarios described in the paragraph "STRUCTURAL PROPERTIES", with the iBA mainly clustered along the pore boundary and some water at the pore wall. We have also done simulations of a single water molecule in a pore filled with iBA and a single iBA molecule in a pore filled with water. In both cases the foreign molecule was preferentially situated at the pore boundary.

Fig. 31 shows data concerning a simulation with a starting case of iBA being confined in the pore center. The upper panel shows the ratio of water of the radial density distribution beyond a given radius. The dashed lines represent the equilibrium values. As we can see after 7.5 ns the simulation has almost reached equilibrium values. The upper of the middel panels shows the development of hydrogen bonding with the pore via the average number of hydrogen bonds given for one pore silanol group. While the number of hydrogen bonds to iBA grows in time this is insufficient to counter the loss of hydrogen

bonded water molecules and the overall number decreases. We consider two water molecules to be hydrogen bonded when the angle between the intramolecular O–H vector and the intermolecular O…O vector is less than 30°, provided that the O…O separation is less than 3.35 Å [92]. The same criterion was used for water and iBA.

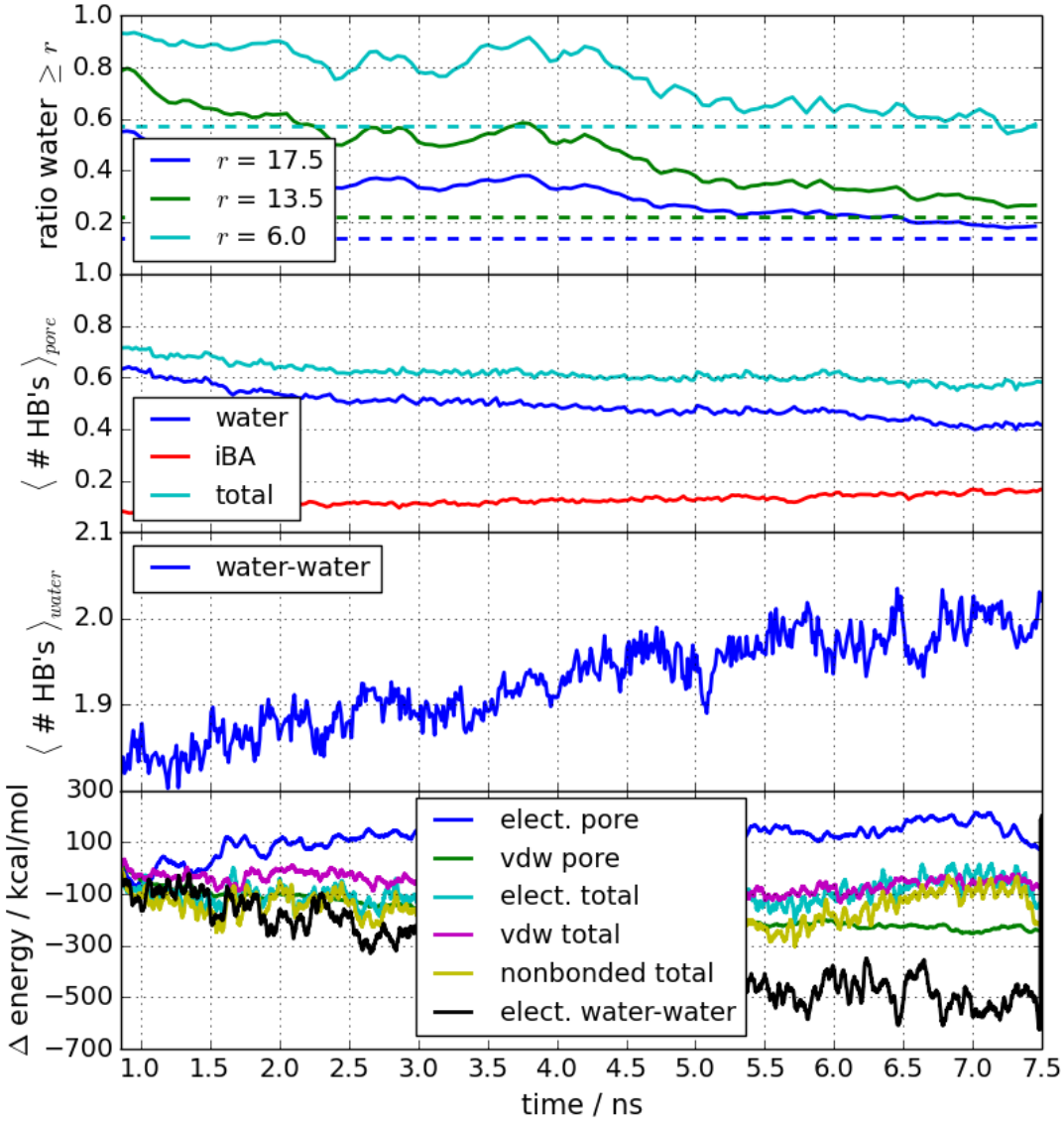

Figure 31: Simulation of a 70wt% mixture with iBA confined to the pore center as starting configuration. Upper panel: ratio of the radial distribution of water beyond a given radius (full lines) and equilibrium values (dashed lines). Upper middle panel: average number of hydrogen bonds between pore and iBA/water mixture per silanol group. Lower middle panel: average number of hydrogen bonds between water molecules per water molecule. Lower panel: change in potential energy of the total system, between pore and mixture and w.r.t. water-water interaction.

The lower of the middle panels shows the number of hydrogen bonds per water molecule which are formed with another water molecule. For all four weight percentages the overall number of hydrogen bonds per water molecule stays almost constant throughout the simulation (between 3.06 and 2.82 for weight percentages 40 through 70, where 3.23 is the bulk (water) value at 300 K). The lower panel

shows the energy differences. As one can see the vdw energy between pore and mixture decreases with more iBA accumulating at the pore boundary, while the electrostatic energy increases. At the same time the electrostatic energy of the water-water interaction decreases as simultaneously the number of water-water hydrogen bonds increases.

The data is shown from 0.85 ns onwards, since the artificial separation of iBA and water initially left a void between the fluid components. The relevant rearrangement of components is captured.

Since we have energy values for a number of different hydrogen bond situations we can evaluate the simulations w.r.t. the average loss of energy between one component of the fluid and pore associated with the loss of a hydrogen bond between pore and fluid. All four weight percentages show very similar values, the average of which are given in fig. 32.

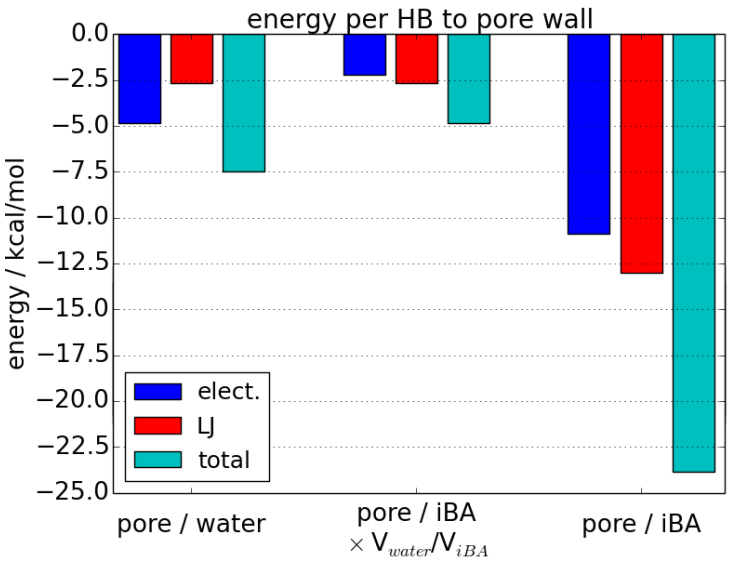

Figure 32: Average change in energy between fluid component and pore per hydrogen bond (with pore). Left hand side: hydrogen bonds between water and pore; right hand side: hydrogen bonds between iBA and pore; middle: hydrogen bonds between iBA and pore, normed by ratio of volume.

Fig. 32 shows the electrostatic, LJ and total nonbonded energy components of the hydrogen bonding, i.e. the change in energy experienced in the pore system with the loss of one hydrogen bond between pore and water or pore and iBA, respectively. On the left hand side is the change in energy for a water molecule, on the right hand side for an iBA molecule and in the middle is again the change in energy for an iBA molecule, normed by the ratio of a single water molecule in bulk water and a single iBA molecule in bulk water.
Clearly the water molecules show a larger electrostatic component, while for iBA molecules there is a larger LJ ratio. The total gain in energy is larger by almost half again as much for a hydrogen bonded water molecule when compared to an iBA molecule when normed by the relative volume. Thus it seems somewhat surprising that the pore boundary is favored by the iBA.

Basically there are two possibilities for the arrangement of molecules at the pore boundary. Either the water molecules adhere to the wall, thus creating two main interfaces to the water front and reducing the number of inter-water hydrogen bonds, or the iBA molecules adhere to the wall, creating two main interfaces to the iBA. Looking at how the energy of the system evolves, one can see that the advantageous electrostatic interaction of water and pore boundary is largely exchanged for a water rich block at the pore center and more water-water hydrogen bonds. This arrangement is supplemented by a smaller water deposit at the pore boundary, mainly due to the high electrostatic interaction between water and pore wall. The difference in vdw energy between fluid and pore wall is minimal when exchanging water and iBA.

The simulations where the water is initially completely in the pore center show the same basic progress, with an increase in the electrostatic water-water potential, and a decrease in the fluid-pore electrostatic interaction as water attaches itself to the pore boundary.

This overall composition is relatively robust against changes in the pore potential. Increasing the partial charges of the pore matrix by 15%, and thus further favoring electrostatic interaction with the pore boundary slightly increases the amount of water at the pore wall, but does not change the basic accumulation of water at the pore center.

5.3.3 Conclusion

We have established a model molecule for iBA based on the CHARMM22 [205] force field and simulated pure iBA and iBA/water mixtures in the bulk and in confinement. In the bulk mixture we observe phase separation occurring roughly in the vicinity of 350 K.
The confined mixture was simulated both in a realistic silica nanopore, denoted as rough pore, and an external potential based on averaging the interaction as given by the rough pore, denoted as smooth pore and devoid of anchoring sites for hydrogen bonding.
We have evaluated structural properties like the radial density distribution and orientation of molecules as well as translational and rotational dynamics. For both smooth and rough pore we have observed accretion of iBA at the pore boundary, though in the case of the rough pore there is a water density peak at the pore boundary, showing a certain amount of water in close contact with the pore.
Orientation of the iBA molecules is highly divergent in the smooth and rough pore, with the carboxylic group pointing towards pore boundary and potential bonding sites for the atomistic pore and towards the water rich phase or other iBA molecules, and therefore again potential hydrogen bonding sites, in the case of the smooth pore. While in the case of the smooth pore the density distribution imitates the strong rotational symmetry of the potential, in the case of the rough pore the iBA/water interface is less smooth for lower temperatures. Pure confined iBA generally exhibits stronger orientation than iBA in a mixture.

In the case of the rough pore the dynamics generally slow down when nearing the pore boundary, although translational motion of the iBA shows a slight speed up very close to the pore wall. This speed up, or plateau, is correlated with the orientation of the molecule and enhanced by the presence of water molecules at the pore boundary. Close to the pore boundary we observe faster translational dynamics in the z-direction than concerning in-plane movement. Orientational dynamics show no actual speed up, even though the gradient of the correlation times diminishes slightly. Reorientation connected to the carboxylic group of the molecule, i.e. the part capable of hydrogen bonding, shows a wider range of correlation times and, in contrast to reorientation of the methyl groups, dynamic processes clearly distinguishable in the Fourier transform of the orientational autocorrelation function.

Dynamics are very different in the smooth pore, where there is no strong slow down when approaching the pore boundary. While translational motion of the water molecules distinctly speeds up at the pore boundary, correlation times of the iBA are strongly correlated to the density profile. Reorientation speeds up for the small water molecules at the pore boundary as well, while the larger iBA molecules are more encumbered by their neighbors and correspondingly slow down.

Accordingly there is a very large difference both in terms of static and dynamic system properties between smooth and rough pore, further emphasizing the important role of hydrogen bonding sites.

Comparison of the correlation times of the coherent and incoherent scattering functions ($\tau_{\mathrm{inc}}/\tau_{\mathrm{coh}}$) show a ratio of up to 1.8 for 300 K. This difference lessens with increasing temperature, more quickly for the higher iBA weight percentages.

The translational and rotational susceptibility of the iBA in the rough pore reveal distinct dynamic processes. Vyalikh et al. [199] made a similar observation in their experimental study concerning a 54wt%

iBA/D_2O mixture in a controlled pore glass of roughly 10.3 nm diameter, although we see both processes in all observed temperatures, not only occurring after having traversed the consulate temperature.

We have performed a number of simulations with non-equilibrium starting conditions in the rough pore, allowing us to track the energy-composition and changes in the hydrogen bonding network. We find that with our parameters water is actually energetically favored as the wetting component w.r.t. fluid-pore interaction. However, the increase in water-water hydrogen bonding and corresponding decrease of electrostatic energy associated with the iBA not occupying the pore center is sufficient to counter this attraction, resulting in the main component at the wall being the iBA, with a small reservoir of water. Even an increase of the partial charges in the pore by 15% does not change the basic configuration, but only slightly increases the amount of water situated at the pore boundary.

The large surface to volume ratio we encounter in our pore system fundamentally alters the behavior we are familiar with from bulk systems. One should take note that we observe a density gradient of the components throughout the complete temperature range we simulated, i.e. from a completely unmixed to mixed state in the unconfined unit cells. In addition this density gradient seems to defy the preference of the confining pore, at least in the case of the atomistic pore representation. However, we can expect this effect to dissolve for larger pores, since the ratio of the existing interface diminishes with respect to pore volume and thus the energetic advantage of iBA being relegated to the pore boundary decreases.

6 Conclusion

In this thesis the question of how water and iBA/water mixtures react to confinement has been investigated, with a special regard given to the transition of rough to smooth confining boundaries. We have seen that different water models can show divergent qualitative behavior, thus defying easy categorization. The ingredients the structural and dynamical behavior is based upon, as given by the interaction strength of a given interface, its geometry, the details of the interaction and the properties of the water model, are subtle and the relative strength of their contributions hard to predict. Of course, this is also a feature which makes the involvement with molecular dynamics interesting and worthwhile. However, some overall concepts have been identified.

A more specific conclusion to each of the three main investigations can be found at the end of each subsection. Here a general overview over the key features of the behavior for pure water will be given.

- Concerning hydrophobic walls, the exact parameters of the interface are less important w.r.t. the response as given by the surrounding water. Abstraction of an atomistic wall via an external potential or change of lattice constant while keeping the same overall potential is less likely to result in different structural or dynamic behavior the weaker the interaction between interface and water and the less inherent order the water model possesses.
- Concerning hydrophilic walls, the structure of the interface has a strong influence on the behavior of the water. While perpendicular translational motion is less effected for small changes in the interfacial roughness, parallel mobility is strongly dependent on interfacial details.
- If the interface interacts sufficiently weakly or is sufficiently smooth, parallel mobility is only weakly curtailed, or even enhanced.
- Some facets of water behavior are strongly dependent on the water model. Therefore it is not automatically given that a reduction in the water/wall interaction will simultaneously lead to a reduction of interfacial water mobility.
- Rough amorphous walls, incorporating charged atoms/dipoles lead to a strong slowdown of water dynamics. This slowdown vanishes when the dipole moment is reduced, and therefore the fluctuations of the potential energy landscape along the interfacial boundary are diminished.
- The absence of orientating contributions by the wall potential allows entropic orientational effects to dominate, eliciting structural oscillations. This results in a disturbance of inherent water structure, encouraging faster dynamics and Arrhenius-like behavior for higher temperatures.
- Disturbance of the tetrahedral water structure reaches very far in cylindrical pores, shifting both tetrahedral entropy and structural relaxation from the bulk behavior.
- Arrhenius-like behavior occurs at the pore boundary to both rough and smooth cylindrical pores, despite the lack of specific anchoring points for the water molecules in the latter case.
- The easily accessible tetrahedral entropy is a good indicator for changes in dynamics and correlates, the degree of correlation depending on the temperature, with the correlation time of the incoherent intermediate scattering function.

These simulations and subsequent evaluation have given us qualitative insight into the behavior of water near interfaces, and on the effect we can expect the hydroaffinity of these interfaces to have. This is

especially relevant w.r.t. the topic of water in biological cells, since in these cases water is always close to surfaces of different hydroaffinity, take e.g. proteins with patchy hydrophobic surfaces.

Furthermore a confined binary mixture of water and isobutyric acid was investigated in this thesis.

By successfully explaining the accretion of iBA at the pore boundary despite the hydrophilic nature of the pore, we could showcase how confinement on the nanoscale effectively changes behavior patterns, since we cannot expect the same behavior to occur at arbitrary (lower) surface to volume ratios. This preference of the water to cluster together on the inside of the pore is likely to be valid for similar binary mixtures. In response to our results Wadim Winschel and Torsten Gutmann from the the work group of Professor Buntkowsky (TU Darmstadt) have undertaken a new set of measurements concerning the iBA/water system in a silica nanopore. Using heteronuclear correlation, a technique they had no access to at the time of the original series of experiments [99] and which offers information on the proximity of certain atoms, they were able to show a definite presence of iBA close to the pore boundary in the low temperature regime, thus validating this part of our results experimentally.

This is an excellent example for how MD simulations and experimental research can mesh together, furthering our understanding of fluid behavior on the microscopic scale.

List of figures

List of tables

List of references

[1] B. Schmandt, S. D. Jacobsen, T. W. Becker, Z. Liu, and K. G. Dueker, *Science* **344**, 1265 (2014).

[2] G. E. Brown Jr., *Science* **294**, 67 (2001).

[3] A. A. Darhuber, and S. M. Troian, *Annu. Rev. Fluid Mech.* **37**, 425 (2005).

[4] V. Srinivasan, V. K. Pamula, and R. B. Fair, *Lab Chip* **4**, 310 (2004).

[5] P. Ball, *Chem. Rev.* **108**, 74 (2008).

[6] K. L. Prime, and G. M. Whitesides, *Science* **252**, 1164 (1991).

[7] H. E. Stanley, S. V. Buldyrev, G. Franzese, P. Kumar, F. Mallamace, M. G. Mazza, K. Stokely, and L. Xu, *J. Phys.: Condens. Matter* **22**, 284101 (2010).

[8] L. Xu, and V. Molinero, *J. Phys. Chem. B* **115**, 14210 (2011).

[9] J.-M. Zanotti, M.-C. Bellissent-Funel, and S.-H. Chen, *Europhys. Lett.* **71**, 91 (2005).

[10] X. Y. Guo, T. Watermann, S. Keane, C. Allolio, and D. Sebastiani, *Z. Phys. Chem.* **226**, 1415 (2012).

[11] C. Bussai, S. Hannongbua, S. Fritzsche, and R. Haberlandt, *Chem. Phys. Lett.* **354**, 310 (2002).

[12] G. Cicero, J. C. Grossman, E. Schwegler, F. Gygi, and G. Galli, *J. Am. Chem. Soc.* **130**, 1871 (2008).

[13] I. Brovchenko, A. Geiger, and A. Oleinikova, *J. Chem. Phys.* **120**, 1958 (2004).

[14] F. Klameth, and M. Vogel, *J. Chem. Phys.* **138**, 134503 (2013).

[15] K. Watanabe, T. Kawasaki, and H. Tanaka, *Nature Materials* **10**, 512 (2011).

[16] P. Scheidler, W. Kob, and K. Binder, *Europhys. Lett.* **59**, 701 (2002).

[17] J. Wang, A. G. Kalinichev, and R. J. Kirkpatrick, *J. Phys. Chem. C* **113**, 11077 (2009).

[18] A. Ben-Naim, *J. Chem. Phys.* **128**, 024505 (2008).

[19] L. Heckmann, and B. Drossel, *J. Chem. Phys.* **137**, 064503 (2012).

[20] T. Truskett, and K. Dill, *J. Phys. Chem. B* **106**, 11829 (2002).

[21] T. Truskett, and K. Dill, *J. Chem. Phys.* **117**, 5101 (2002).

[22] T. Truskett, and K. Dill, *Biophys. Chem.* **105**, 449 (2003).

[23] G. Franzese, and H. Stanley, *J. Phys.: Condens. Matter* **14**, 2201 (2002).

[24] G. Franzese, and H. Stanley, *Physica A* **314**, 508 (2002).

[25] L. Heckmann, and B. Drossel, *J. Chem. Phys.* **138**, 234503 (2013).

[26] M. J. Stevens, and G. S. Grest, *Biointerphases* **3**, FC13 (2008).

[27] M.-C. Bellissent-Funel, R. Sridi-Dorbez, and L. Bosio, *J. Chem. Phys.* **104**, 10023 (1996).

[28] P. A. Bonnaud, B. Coasne, and R. J.-M. Pellenq, *J. Phys.: Condens. Matter* **22**, 284110 (2010).

[29] C. E. Bertrand, K.-H. Liu, E. Mamontov, and S.-H. Chen, *Phys. Rev. E* **87**, 042312 (2013).

[30] B. Guillot, *J. Mol. Liqu.* **101**, 219 (2002).

[31] D. J. Price, and C. L. Brooks III, *J. Chem. Phys.* **121**, 10096 (2004).

[32] H. W. Horn, W. C. Swope, J. W. Pitera, J. D. Madura, T. J. Dick, G. L. Hura, and T. Head-Gordon, *J. Chem. Phys.* **120**, 9665 (2004).

[33] S. W. Rick, *J. Chem. Phys.* **120**, 6085 (2004).

[34] H. J. C. Berendsen, J. R. Grigera, T. P. Straatsma, *J. Phys. Chem.* **91**, 6269 (1987).

[35] C. Vega, J. L. F. Abascal, M. M. Conde, and J. L. Aragones, *Faraday Discuss.* **141**, 251 (2008).

[36] J. Zielkiewicz, *J. Chem. Phys.* **123**, 104501 (2005).

[37] G. Baaken, N. Ankri, A. Schuler, J. Ruhe, and J. C. Behrends, *ACS Nano* **5**, 8080 (2011).

[38] M. Jensen, O. Mouritsen, and G. Peters, *J. Chem. Phys.* **120**, 9729 (2004).

[39] LI EnZe, DU ZhiPing, and YUAN ShiLing, *Science China Chemistry* **56**, 773 (2013).

[40] J. Li, T. Liu, X. Li, L. Ye, H. Chen, H. Fang, Z. Wu, and R. Zhou, *J. Phys. Chem. B* **109**, 13639 (2005).

[41] Tomohiro Hayashi, Alexander J. Pertsin, and Michael Grunze, *J. Chem. Phys.* **117**, 6271 (2005).

[42] P. Kumar, F. Starr, S. V. Buldyrev, and H. E. Stanley, *Phys. Rev. E* **75**, 011202 (2007).

[43] S. Clifford, K. Bolton, and D. Ramjugernath, J. Phys. Chem. B 110, 21938 (2006).

[44] M. Grayson, D. Eckroth, H. F. Mark, D. F. Othmer, C. G. Overberger, and G. T. Seaborg, *Encyclopedia of Chemical Technology, 3rd ed.*, John Wiley & Sons: New York, 1978, Vol. 4.

[45] P. Y. Bruice, *Organic Chemistry, 2nd ed.*, Prentice Hall: New Jersey, 1998

[46] W. Gerhartz, Y. S. Yamamoto, F. T. Campbell, R. Pfefferkorn, J. F. Rounsaville, *Ullmann's Encyclopedia of Industrial Chemistry, 5th ed.*, VCH: Weinheim, 1986, Vol A5.

[47] L. W. Codd, K. Dijkhoff, J. H. Fearon, C. J. van Oss, H. G. Roebersen, E. G. Stanford, *Materials and Technology*, Longman-J. H. de Bussy: Amsterdam, 1972, Vol. 4.

[48] S. Patai, *The Chemistry of Functional Groups Supplement B: The Chemistry of Acid Derivatives, Part 1*, John Wiley & Sons: Chichester, 1979.

[49] R. Sewnarain, J. D. Raal, and D. Ramjugernath, *J. Chem. Eng. Data* **47**, 603 (2002).

[50] M. Sliwinska-Bartkowiak, S. L. Sowers, and K. E. Gubbins, *Langmuir* **13**, 1182 (1997).

[51] M. Sliwinska-Bartkowiak, R. Sikorski, S. L. Sowers, L. D. Gelb, and K. E. Gubbins, *Fluid Phase Equilib.* **136**, 93 (1997).

[52] W. T. Gozdz, K. E. Gubbins, and A. Z. Panagiotopoulos, *Mol. Phys.* **84**, 825 (1995).

[53] L. D. Gelb, and K. E. Gubbins, *Physica A* **244**, 112 (1997).

[54] L. D. Landau, and E. M. Lifshitz, *Statistical Physics, vol. 1, 3rd ed.*, Pergamon Press, Oxford, 1980.

[55] V. P. Voronov, and V. M. Buleiko, *J. Exp. Theor. Phys.* **86**, 586 (1998).

[56] L. V. Entov, V. A. Levchenko, and V. P. Voronov, *Int. J. Thermophys.* **14**, 221 (1993).

[57] W. I. Goldburg, F. Aliev, and X.-I. Wu, *Physica A* **213**, 61 (1995).

[58] R. Valiullin, and I. Furó, *J. Chem. Phys.* **116**, 1072 (2002).

[59] M. C. Goh, W. I. Goldburg, and C. M. Knobler, *Phys. Rev. Lett.* **58**, 1008 (1987)

[60] Z. Zhuang, A. G. Casielles, and D. S. Cannell, *Phys. Rev. Lett.* **77**, 2969 (1996).

[61] E. Kierlik, Y. Fan, P. A. Monson, and M. L. Rosinberg, *J. Chem. Phys.* **102**, 3712 (1995).

[62] S. K. Kumar, H. Tang, and I. Szleifer, *Mol. Phys.* **81**, 867 (1994).

[63] L. D. Gelb, and K. E. Gubbins, *Phys. Rev. E* **55**, R1290 (1997).

[64] P. Kumar, S. V. Buldyrev, H. E. Stanley, *PNAS* **106**, 22130 (2009).

[65] J. C. Phillips, R. Braun, W. Wang, J. Gumbart, E. Tajkhorshid, E. Villa, C. Chipot, R. D. Skeel, L. Kale, and K. Schulten, *J. Comp. Chem.* **26**, 1781 (2005).

[66] E. Lindahl, B. Hess, D. van der Spoel, *J. Mol. Model.* **7**, 306 (2001).

[67] D. Frenkel, B. Smit, *Understanding Molecular Simulation from Algorithms to Applications*, Academic Press, San Diego, 2002.

[68] S. E. Feller, Y. Zhang, R. W. Pastor, B. R. Brooks, *J. Chem. Phys.* **103**, 4613 (1995).

[69] H. C. Andersen, *J. Chem. Phys.* **72**, 2384 (1980).

[70] W. F. van Gunsteren, D. Bakowies, R. Baron, I. Chandrasekhar, M. Christen, X. Dauea, P. Gee, D. P. Geerke, A. Glättli, P. H. Hünenberger, K. M. A., C. Oostenbrink, M. Schenk, D. Trzesniak, N. F. A. van der Vegt, and H. B. Yu, *Angew. Chemie* **118**, 4168 (2006).

[71] J. L. F. Abascal, and C. Vega, *J. Chem. Phys.* **123**, 234505 (2005).

[72] G. Lamoureux, E. Harder, I. V. Vorobyov, B. Roux, and A. D. MacKerell Jr., *Chem. Phys. Lett* **418**, 245 (2006).

[73] A. Laio, J. VandeVondele, and U. Rothlisberger, *J. Chem. Phys.* **116**, 6941 (2002).

[74] T. Werder, J. H. Walther, and P. Koumoutsakos, *J. Comp. Phys.* **205**, 373 (2005).

[75] K. M. Mohamed, and A. A. Mohamad, *Microfluid Nanofluid* **8**, 283 (2010).

[76] A. H. Narten, and H. A. Levy, *J. Chem. Phys.* **55**, 2263 (1971).

[77] G. Hura, J. M. Sorenson, R. M. Glaeser, and T. Head-Gordon, *J. Chem. Phys.* **113**, 9140 (2000).

[78] A. K. Soper, and M. G. Phillips, *Chem. Phys.* **107**, 47 (1986).

[79] A. K. Soper, *Chem. Phys.* **258**, 121 (2000).

[80] H. Palamarev, and G. Georgiev, *Vib. Spectrosc.* **7**, 255 (1994).

[81] H. R. Wyss, and M. Falk, *Can. J. Chem.* **48**, 607 (1970).

[82] W. A. Senior, and R. E. Verrall, *J. Phys. Chem.* **73**, 4242 (1969).

[83] J. B. Asbury, T. Steinel, C. Stromberg, S. A. Corcelli, C. P. Lawrence, J. L. Skinner, and M. D. Fayer, *J. Phys. Chem. A* **108**, 1107 (2004).

[84] J. D. Smith, C. D. Cappa, K. R. Wilson, R. C. Cohen, P. L. Geissler, and R. J. Saykally, *Proc. Natl. Acad. Sci. U.S.A.* **102**, 14171 (2005).

[85] R. Kumar, J. R. Schmidt, and J. L. Skinner, *J. Chem. Phys.* **126**, 204107 (2007).

[86] http://upload.wikimedia.org/wikipedia/commons/thumb/c/c6/3D_model_hydrogen_bonds_in_water.svg/1032px-3D_model_hydrogen_bonds_in_water.svg.png, (31.05.2015).

[87] J. D. Smith, C. D. Cappa, K. R. Wilson, R. C. Cohen, P. L. Geissler, and R. J. Saykally, *PNAS* **102**, 14171 (2005)

[88] W. L. Jorgensen, *Chem. Phys. Lett.* **70**, 326 (1980).

[89] W. L. Jorgensen, J. Chandrasekhar, J. D. Madura, R. W. Impey, and M. L. Klein, *J. Chem. Phys.* **79**, 926 (1983).

[90] A. Geiger, and H. E. Stanley, *Phys. Rev. Lett.* **49**, 1749 (1982).

[91] F. H. Stillinger, *Science* **209**, 451 (1980).

[92] C. Hartnig, W. Witschel, E. Spohr, P. Gallo, M. A. Ricci, M. Rovere, *J. Mol. Liq.* **85**, 127 (2000).

[93] J. R. Errington, and P. G. Debenedetti, *Nature* **409**, 318 (2001).

[94] P. L. Chau, and A. Hardwick, *Mol. Phys.* **93**, 511 (1998).

[95] J.-P. Hansen, and I. R. McDonald, *Theory of Simple Liquids, 3rd ed.*, Academic, London, 2006.

[96] G. Strobl, *The Physics of Polymers*, Springer, 1996.

[97] A. Bormuth, *Untersuchung der Polymerdynamik in Abhängigkeit von Kettenlänge, Temperatur und Druck mit Hilfe von Molekulardynamik Simulationen*, Dissertation, TU Darmstadt, 2012.

[98] S. H. Lee, Peter J. Rossky, *J. Chem. Phys.* **100**, 3334 (1994).

[99] A. Vyalikh, Th. Emmler, I. Shenderovich, Y. Zeng, G. H. Findenegg, and G. Buntkowsky, *Phys. Chem. Chem. Phys.* **9**, 2249 (2007).

[100] E. Gedat, A. Schreiber, J. Albrecht, I. Shenderovich, G. Findenegg, H.-H. Limbach, and G. Buntkowsky, *J. Phys. Chem. B* **106**, 1977 (2002).

[101] L. N. G. Filon, *Proc. Roy. Soc. Edinburgh: Sect. A* **49**, 38 (1929).

[102] T. Blochowicz, *Broadband Dielectric Spectroscopy in Neat and Binary Molecular Glass Formers*, Dissertation, Universität Bayreuth, 2003.

[103] R. Zwanzig, *Nonequilibrium Statistical Mechanics, 1st ed.*, Oxford University Press, 2001.

[104] C. Vega, E. Sanz, and J. L. F. Abascal, *J. Chem. Phys.* **122**, 114507 (2005).

[105] H. Vogel, *Z. Phys.* **22**, 645, (1921).

[106] G. S. Fulcher, *J. Am. Ceram. Soc.* **8**, 339 (1925).

[107] G. Tammann, and W. Hesse, *Z. anorg. allg. Chem.* **156**, 245 (1926).

[108] C. A. Angell, K. L. Ngai, G. B. McKenna, P. F. McMillan, and S. W. Martin, *J. Appl. Phys.* **88**, 3113 (2000).

[109] M. D. Ediger, C. A. Angell, and S. R. Nagel, *J. Phys. Chem.* **100**, 13200 (1996).

[110] A. Cavagna, *Phys. Rep.* **476**, 51 (2009).

[111] W. T. Laughlin, and D. R. Uhlmann, *J. Phys. Chem.* **76**, 2317 (1972).

[112] J. Jäckle, *Rep. Prog. Phys.* **49**, 171 (1986).

[113] G. Adam, and J. H. Gibbs, *J. Chem. Phys.* **43**, 139 (1965).

[114] M. Goldstein, *J. Chem. Phys.* **51**, 3728 (1969).

[115] F. H. Stillinger, *Science* **267**, 1935 (1995).

[116] P. G. Debenedetti, and F. H. Stillinger, *Nature* **410**, 259 (2001).

[117] R. Richert, *J. Phys. Cond. Mat.* **14**, R703 (2002).

[118] E. R. Weeks, J. C. Crocker, A. C. Levitt, A. Schofield, and D. A. Weitz, *Science* **287**, 627 (2000).

[119] W. Kob, C. Donati, S. J. Plimpton, P. H. Poole, and S. C. Glotzer, *Phys. Rev. Lett.* **79**, 2827 (1997).

[120] R. A. L. Jones, *Soft Condensed Matter*, Oxford University Press, New York, 2011.

[121] C. A. Angell, and W. Sichina, *Ann. N. Y. Acad. Sci.* **279**, 53 (1976).

[122] N. Giovambattista, S. V. Buldyrev, F. W. Starr, and H. E. Stanley, *Phys. Rev. Lett.* **90**, 085506-1 (2003).

[123] Y. Rosenfeld, *J. Phys. Cond. Mat.* **11**, 5415 (1999).

[124] M. Dzugutov, *Nature* **381**, 137 (1996).

[125] S. Chapman, and T. G. Cowling, *The Mathematical Theory of Non-Uniform Gases, 3rd edition*, Cambridge University Press, Cambridge, 1970.

[126] Y. Rosenfeld, *Phys. Rev. A* **15**, 2545 (1977).

[127] M. Dzugutov, *Phys. Rev. A* **46**, 2924 (1992).

[128] F. Stillinger, and R. A. La Violette, *J. Chem. Phys.* **83**, 6413 (1985).

[129] M. Dzugutov, M. Alvarez, and E. Lomba, *J. Phys. Cond. Mat.* **6**, 4419 (1994).

[130] M. Dzugutov, K.-E. Larsson, and I. Ebbsjö, *Phys. Rev. A* **38**, 3609 (1988).

[131] M. Dzugutov, *Europhys. Lett.* **26**, 533, (1994).

[132] M. Dzugutov, *Phys. Rev. Lett* **70**, 2924 (1993).

[133] M. Dzugutov, *Europhys. Lett.* **31**, 95, (1995).

[134] J. P. Boon, and S. Yip, *Molecular Hydrodynamics*, McGraw-Hill, New York, 1980.

[135] Y. Rosenfeld, *Phys. Rev. A* **28**, 3063 (1983).

[136] J. Mittal, J. R. Errington, and T. M. Truskett, *Phys. Rev. Lett.* **96**, 177804 (2006).

[137] J. Mittal, J. Errington, and T. Truskett, J. Phys. Chem. B 111, 10054 (2007).

[138] J. Mittal, J. R. Errington, T. M. Truskett, *J. Chem. Phys.* 125, 076102 (2006).

[139] A. B. de Oliveira, P. A. Netz, T. Colla, and M. C. Barbosa, *J. Chem. Phys.* **124**, 084505 (2006).

[140] S. Sastry, *Nature* **409**, 164 (2001).

[141] S. Sastry, *Phys. Rev. Lett.* **85**, 590 (2000).

[142] Y. D. Fomin, and V. N. Ryzhov, *arXiv:1004.1894*.

[143] Y. D. Fomin, N. V. Gribova, V. N. Ryzhov, S. M. Stishov, D. Frenkel, *J. Chem. Phys.* **129**, 064512 (2008).

[144] R. Sharma, S. N. Chakraborty, and C. Chakravarty, *J. Chem. Phys.* 125, 204501 (2006).

[145] W. P. Krekelberg, M. J. Pond, G. Goel, V. K. Shen, J. R. Errington, and T. M. Truskett, *Phys. Rev. E* **80**, 061205 (2009).

[146] R. Chopra, T. M. Truskett, and J. R. Errington, *J. Phys. Chem. B* **114**, 10558 (2010).

[147] M. Agarwal, M. Singh, R. Sharma, M. P. Alam, and C. Chakravarty, *J. Phys. Chem. B* **114**, 6995 (2010).

[148] M. Agarwal, M. P. Alam, and C. Chakravarty, *J. Phys. Chem. B* **115**, 6935 (2011).

[149] S. Prasad, and C. Chakravarty, *J. Chem. Phys.* **140**, 164501 (2014).

[150] J. Mittal, J. R. Errington, and T. M. Truskett, *J. Phys. Chem. B* **110**, 18147 (2006).

[151] F. Brochard, and P. G. De Gennes, *J. Physique Lett.* **44**, L785 (1983).

[152] P. G. De Gennes, *J. Phys. Chem* **88**, 6469 (1984).

[153] A. J. Liu, D. J. Durian, E. Herbolzheimer, and S. A. Safran, *Phys. Rev. Lett.* **65**, 1897 (1990).

[154] H. Nakanishi, and M. E. Fisher, *J. Chem. Phys* **78**, 3279 (1983).

[155] V. Privman, *Finite Size Scaling and Numerical Simulation of Statistical Systems*, World Scientific, Singapore, 1990.

[156] J. V. Maher, W. I. Goldburg, D. W. Pohl, and M. Lanz, *Phys. Rev. Lett.* **53**, 60 (1984).

[157] M. Y. Lin, S. K. Sinha, J. M. Drake, X.-I. Wu, P. Thiyagarajan, and H. B. Stanley, *Phys. Rev. Lett.* **72**, 2207 (1994).

[158] H. Tanaka, *Phys. Rev. Lett.* **70**, 2770 (1993).

[159] J. W. Cahn, *J. Chem. Phys.* **66**, 3667 (1977).

[160] J. Bodensohn, and W. I. Goldburg, *Phys. Rev. A* **46**, 5084 (1992).

[161] P. Guenoun, D. Beysens, and M. Robert, *Phys. Rev. Lett.* **65**, 2406 (1990).

[162] P. Wiltzius, and A. Cumming, *Phys. Rev. Lett.* **66**, 3000 (1991).

[163] F. Bruder, and R. Brenn, *Phys. Rev. Lett.* **69**, 624 (1992).

[164] P. Wiltzius, S. B. Dierker, and B. S. Dennis, *Phys. Rev. Lett.* **62**, 804 (1989).

[165] L. Monette, A. J. Liu, G. S. Grest, *Phys. Rev. A* **46**, 7664 (1992).

[166] M. F. Harrach, F. Klameth, B. Drossel, and M.Vogel, *J. Chem. Phys.* **142**, 034703 (2015).

[167] David J. Huggins, *J. Chem. Phys.* **136**, 064518 (2012).

[168] T. Werder, J. H. Walther, R. L. Jaffe, T. Halicioglu, and P. Koumoutsakos, *J. Phys. Chem. B* **107**, 1345 (2003).

[169] Ivan Brovchenko, and Alla Oleinikova, *J. Phys. Chem. B*, **114**, 16494 (2010).

[170] D. Argyris, N. R. Tummala, and A. Striolo, *J. Phys. Chem. C* **112**, 13587 (2008).

[171] C. Y. Lee, J. A. McCammon, and P. J. Rossky, *J. Chem. Phys.* **80**, 4448 (1984).

[172] J. R. Grigera, S. G. Kalko, and J. Fischbarg, *Langmuir* **12**, 154 (1996).

[173] A. Malani, K. G. Ayappa, and S. Murad, *J. Phys. Chem. B* **113**, 13825 (2009).

[174] T. R. Jensen, M. Ø. Jensen, N. Reitzel, K. Balashev, G. H. Peters, K. Kjaer, and T. Bjørnholm, *Phys. Rev. Lett.* **90**, 86101 (2003).

[175] M. C. Gordillo, G. Nagy, and J. Martí, *J. Chem. Phys.* **123**, 54707 (2005).

[176] A. J. Pertsin, T. Hayashi, and M. Grunze, *J. Phys. Chem. B* **106**, 12274 (2002).

[177] L. Cheng, P. Fenter, K. L. Nagy, M. L. Schlegel, and N. C. Sturchio, *Phys. Rev. Lett.* **87**, 156103 (2001).

[178] A. Pertsin, and M. Grunze, *J. Phys. Chem. B* **108**, 16533 (2004).

[179] J. R. Grigera, *J. Chem. Phys.* **72**, 3439 (1980).

[180] T. A. Ho, D. V. Papavassiliou, L. L. Lee, and A. Striolo, *PNAS* **108**, 16170 (2011).

[181] A. Bródka, T. W. Zerda, *J. Chem. Phys.* **104** 6319 (1996).

[182] S. Nosé, *Mol. Phys.* **52**, 255 (1984).

[183] W. G. Hoover, *Phys. Rev. A* **31**, 1695 (1985).

[184] C. Allolio, F. Klameth, M. Vogel, and D. Sebastiani, *ChemPhysChem* **18**, 3955 (2014).

[185] M. Parrinello, A. Rahman, *J. Appl. Phys.* **52**, 7182 (1981).

[186] F. Klameth, P. Henritzi, and M. Vogel, *J. Chem. Phys.* **140**, 144501 (2014).

[187] D. Argyris, D. R. Cole, and A. Striolo, *Langmuir* **25**, 8025 (2009).

[188] P. A. Bonnaud, B. Coasne, and R. J.-M. Pellenq, *J. Phys. Cond. Mat.* **22**, 284110 (2010).

[189] D. Nayar, M. Agarwal, and C. Chakravarty, *J. Chem. Theory. Comput.* **7**, 3354 (2011).

[190] A. Scala, F. W. Starr, E. La Nave, F. Sciortino, and H. E. Stanley, *Nature* **406**, 166 (2000).

[191] E. Mamontov, D. J. Wesolowski, L. Vlcek, P. T. Cummings, J. Rosenqvist, W. Wang, and D. R. Cole, *J. Phys. Chem. C* **112**, 12334 (2008).

[192] J. Teixeira, M.-C. Bellissent-Funel, S. H. Chen, and A. J. Dianoux, *Phys. Rev. A* **31**, 1913 (1985).

[193] E. Mamontov, L. Vlcek, D. J. Wesolowski, P. T. Cummings, J. Rosenqvist, W. Wang, D. R. Cole, L. M. Anovitz, and G. Gasparovic, *Phys. Rev. E* **79**, 051504 (2009).

[194] F. Sedlmeier, Y. von Hansen, L. Mengyu, D. Horinek, R. R. Netz, *J. Stat. Phys.* **145**, 240 (2011).

[195] M. F. Harrach, and B. Drossel, *J. Chem. Phys.* **140**, 174501 (2014).

[196] W. P. Krekelberg, V. K. Shen, J. R. Errington, *J. Chem. Phys.* **135**, 154502 (2011).

[197] K. P. Lee, H. Leese, D. Mattia, *Nanoscale* **4**, 2621 (2012).

[198] M. Rosenstihl, K. Kämpf, F. Klameth, M. Sattig, and M. Vogel, *J. Non-Cryst. Solids* **407**, 449 (2015).

[199] A. Vyalikh, Th. Emmler, E. Gedat, I. Shenderovich, G. H. Findenegg, H.-H. Limbach, and G. Buntkowsky, *Solid State Nuclear Magnetic Resonance* **28**, 117 (2005).

[200] B. R. Brooks, R. E. Bruccoleri, B. D. Olafson, D. J. States, S. Swaminathan, and M. Karplus, *J. Comp. Chem.* **4**, 187 (1983).

[201] W. Humphrey, A. Dalke, and K. Schulten, *J. Mol. Graphics* **14**, 33 (1996).

[202] G. J. Kleywegt, *Acta Cryst.* **D63**, 94 (2007).

[203] G. J. Kleywegt, K. Henrick, E. J. Dodson, and D. M. F. van Aalten, *Structure*, **11**, 1051 (2003).

[204] G. J. Kleywegt, and T. A. Jones, *Acta Cryst.* **D54**, 1119 (1998).

[205] A. D. MacKerell, Jr., D. Bashford, M. Bellott, R. L. Dunbrack, Jr., J. D. Evanseck, M. J. Field, S. Fischer, J. Gao, H. Guo, S. Ha, D. Joseph-McCarthy, L. Kuchnir, K. Kuczera, F. T. K. Lau, C. Mattos, S. Michnick, T. Ngo, D. T. Nguyen, B. Prodhom, W. E. Reiher, III, B. Roux, M. Schlenkrich, J. C. Smith, R. Stote, J. Straub, M. Watanabe, J. Wiórkiewicz-Kuczera, D. Yin, and M. Karplus, *J. Phys. Chem. B* **102**, 3586 (1998).

[206] M. Rovere, M. A. Ricci, D. Vellati, and F. Bruni, *J. Chem. Phys.* **108**, 9859 (1998).

[207] A. Janz, *Molekulardynamik-Simulationen an Wasser-Peptid-Systemen des Peptids VPGVG zur Untersuchung der Struktur-Dynamik-Beziehung*, Master-Thesis, TU Darmstadt, 2012.

[208] J.-R. Hill, and J. Sauer, *J. Phys. Chem.* **98** 1238 (1994).

[209] B. Chu, F. Schoenes, and W. I. Kao, *J. Am. Chem. Soc.* **90**, 3042 (1968).

[210] B. Chu, and F. J. Schoenes, *Phys. Rev.* **185**, 219 (1969).

[211] Y. C. Chou, and W. I. Goldburg, *Phys. Rev. A* **20**, 2105 (1979).

[212] P. Scheidler, W. Kob, and K.Binder, *J. Phys. Chem. B* **108**, 6673 (2004).

[213] M. Alcoutlabi, and G. B. McKenna, *J. Phys. Cond. Mat.* **17**, R461 (2005).

[214] C. Alba-Simionesco, B. Coasne, G. Dosseh, G. Dudziak, K. E. Gubbins, R. Radhakrishnan, and M. Sliwinska-Bartkowiak, *J. Phys. Cond. Mat.* **18**, R15 (2006).

[215] M. Arndt, R. Stannarius, W. Gorbatschow, and F. Kremer, *Phys. Rev. E* **54**, 5377 (1996).

[216] B. J. Frisken, and D. S. Cannell, *Phys. Rev. Lett.* **69**, 632 (1992).

List of publications

- M. F. Harrach, M. Heckmann, and B. Drossel, *J. Chem. Phys.* **137**, 044908 (2012), Strong stretching theory for diblock copolymers in thin films under application of electric fields.
- M. F. Harrach, and B. Drossel, *J. Chem. Phys.* **140**, 174501 (2014), Structure and dynamics of TIP3P, TIP4P, and TIP5P water near smooth and atomistic walls of different hydroaffinity.
- M. F. Harrach, F. Klameth, B. Drossel, and M. Vogel, *J. Chem. Phys.* **142**, 034703 (2015), Effect of the hydroaffinity and topology of pore walls on the structure and dynamics of confined water.

university	
09/2011 - 07/2015	Ph.D. student and research associate at the TU Darmstadt
10/2005 - 08/2011	student of physics and mathematics at the TU Darmstadt
08.08.2011	M.Sc. Physics at the TU Darmstadt
09.10.2009	B.Sc. Physics at the TU Darmstadt
09/2007 - 04/2008	study abroad at the University of Saskatchewan, Canada
16.08.2007	Vordiplom Mathematik at the TU Darmstadt
school	
09/2001 - 06/2004	Friedrich-Dessauer-Gymnasium, Frankfurt am Main (Höchst)
birth	
11.10.1984	Frankfurt am Main

Acknowledgment

I would like to thank all those people who have helped and supported me during my time at the TU Darmstadt.

Special thanks go to my professor and immediate supervisor Barbara Drossel, without whom this work would never have been written. Her door is always open and everybody in the work group knows that we can ask her for help anytime. I would also like to thank professor Michael Vogel for advice and discussion, as well as for venturing a second opinion on this thesis.

Thanks also go to Felix Klameth, who was already an experienced MD simulant when I started to get familiar with the topic, and with whom I collaborated with respect to the topic of SPC/E water in smooth and atomistically rough pores, where the simulations and evaluation of the latter were carried out by him.

I would also like to thank my colleagues in the work group, especially those who were stationed in the same office and thus had to suffer my company, notably Lotta Heckmann, with whom I shared many of our supervisory duties as teaching assistance, Christopher ”Mifo” Priester, who suddenly found himself in an office full of MD people and Julian Geske, who was kind enough to proofread excerpts of this work.

Of course thanks also go the DFG for grant FOR 1583, and the admins, Markus Rosenstihl, Daniel Löb, Marco Möller, Christian Kolb, Christoph Schmitt and Philipp Gramlich, all of whom do - or did - a great job caring for our computer systems and allowing us to actually do any research.

Last but not least I would like to acknowledge my parents and family who have always been willing to support me and my decisions.